Fakultät für
Mathematik, Informatik
und Naturwissenschaften

RWTH AACHEN
UNIVERSITY

Structure and Magnetic Properties of Magnetocaloric $Mn_3Fe_2Si_3$

Von der Fakultät für Mathematik, Informatik und Naturwissenschaften der RWTH Aachen
University zur Erlangung des akademischen Grades eines
Doktors der Naturwissenschaften genehmigte Dissertation

Vorgelegt von

Mohammed Ait haddouch, M.Sc.

aus

Casablanca, Marokko,

Berichter: Professor Dr. Thomas Brückel

Professor Dr. Georg Roth

Tag der mündlichen Prüfung: 29.11.2021

Abstract

The magnetocaloric effect (MCE) is thermodynamically described by the temperature change of a magnetic material upon adiabatic change of magnetic field. This effect affords a sustainable technique for refrigeration, if cheap and environment-friendly materials are used. Therefore, it attracts the attention of many scientific studies. In this thesis we are interested in the compound $Mn_3Fe_2Si_3$, which belongs to the $Mn_{5-x}Fe_xSi_3$ ($0 \leqslant x \leqslant 5$). These compounds fit to the new paradigm that the existence of different magnetic sites in a compound is beneficial for a large MCE.

First part of this thesis is devoted to macroscopic investigation on the single crystalline specimen of the $Mn_3Fe_2Si_3$. The magnetic field vs temperature of $Mn_3Fe_2Si_3$ is similar yet not identical to the parent compound Mn_5Si_3. The $Mn_3Fe_2Si_3$ compound exhibits two antiferromagnetic phase transitions AF1 and AF2. The magnetic response is anisotropic, e.g. the transition AF2 to PM is visible only, if the field is applied perpendicular [001]. Compared to Mn_5Si_3, which features a field driven transition from AF1 to AF2, no remarkable increase is observed in the magnetization of $Mn_3Fe_2Si_3$ and accordingly only a small isothermal entropy change is derived.

The second and third part of this thesis is about Crystal and magnetic structure investigation by means of synchrotron radiation and neutron diffraction. The results show that $Mn_3Fe_2Si_3$ crystallizes in hexagonal space group $P6_3/mcm$. No clear sign of a structural phase transition down to lowest temperature, nor any indication of a clear response of the lattice parameter to the magnetic transitions. $Mn_3Fe_2Si_3$ has a collinear magnetic structure in the AF2 phase and a non-collinear magnetic structure in AF1 phase. The both phases have ordered moments already on the M1 site and 2/3 of the M2 sites. By comparing the magnetic structure of $Mn_3Fe_2Si_3$ and the parent compound Mn_5Si_3, we find strong similarities in the magnetic structure with the distinct difference of the ordering on the M1 site. We associate these differences with the strength of the magneto-caloric properties.

Zusammenfassung

Der magnetokalorische Effekt (MCE) wird thermodynamisch durch die Temperaturänderung eines magnetischen Materials bei einer adiabatischen Änderung des Magnetfelds beschrieben. Dieser Effekt ermöglicht eine nachhaltige Kältetechnik, wenn günstige und umweltfreundliche Materialien verwendet werden. Daher zieht es die Aufmerksamkeit vieler wissenschaftlicher Studien auf sich. In dieser Arbeit interessieren wir uns für die Verbindung $Mn_3Fe_2Si_3$, die zu $Mn_{5-x}Fe_xSi_3$ ($0\leqslant$ x$\leqslant 5$) gehört. Diese Verbindungen passen zu dem neuen Paradigma, dass die Existenz verschiedener magnetischer Zentren in einer Verbindung für ein großes MCE von Vorteil ist.

Der erste Teil dieser Dissertation widmet sich der makroskopischen Untersuchung an der einkristallinen Probe des $Mn_3Fe_2Si_3$. Das Magnetfeld gegenüber der Temperatur von $Mn_3Fe_2Si_3$ ist ähnlich, aber nicht identisch mit der Mutterverbindung Mn_5Si_3 . Die Verbindung $Mn_3Fe_2Si_3$ weist zwei antiferromagnetische Phasenübergänge AF1 und AF2 auf. Die magnetische Reaktion ist anisotrop, z.B. der Übergang AF2 zu PM ist nur sichtbar, wenn das Feld senkrecht angelegt wird [001]. Im Vergleich zu Mn_5Si_3, das einen feldgesteuerten Übergang von AF1 zu AF2 aufweist, wird keine bemerkenswerte Zunahme der Magnetisierung von $Mn_3Fe_2Si_3$ beobachtet und dementsprechend wird nur eine kleine isotherme Entropieänderung abgeleitet.

Der zweite und dritte Teil dieser Arbeit beschäftigt sich mit Kristall- und Magnetstrukturuntersuchungen mittels Synchrotronstrahlung und Neutronenbeugung. Die Ergebnisse zeigen, dass $Mn_3Fe_2Si_3$ in der hexagonalen Raumgruppe $P6_3/mcm$ kristallisiert. Kein klares Anzeichen für einen strukturellen Phasenübergang bis zur niedrigsten Temperatur, noch irgendein Hinweis auf eine klare Reaktion des Gitterparameters auf die magnetischen Übergänge. $Mn_3Fe_2Si_3$ hat eine kollineare magnetische Struktur in der AF2-Phase und eine nicht-kollineare magnetische Struktur in der AF1-Phase. Die beiden Phasen haben bereits bestellte Momente auf der M1-Site und 2/3 der M2-Sites. Durch Vergleich der magnetischen Struktur von $Mn_3Fe_2Si_3$ und der Stammverbindung Mn_5Si_3 finden wir starke Ähnlichkeiten in der magnetischen Struktur mit dem deutlichen Unterschied der Ordnung auf der M1-Stelle. Wir verbinden diese Unterschiede mit der Stärke der magnetokalorischen Eigenschaften.

Acknowledgements

There are many who helped me along the way on this thesis, and I would like to thank them all for helping me in diverse ways.

Prof. Dr.Thomas Brückel, for giving me the opportunity to work in JCNS-2, one of the best institutes in neutron scattering field, I am grateful for his guidance and discussions during my work here and of course for reviewing my thesis.

Prof. Dr. Georg Roth for accepting to be the second review of my thesis.

apl. Prof. Dr. Karen Friese, for her support and guidance. I am grateful for her advice, constructive criticism, and patience with me throughout this thesis. I thank her for her efforts in teaching me and helping me to have a deeper understanding of crystallography.

Dr. Jörg Voigt, for helping me evolve in data analysis and keeping pace with my progress step by step. I am grateful for the time and effort he put into making this project a success. I learned a lot from his discussions with me and of course I still have a lot to learn.

Dr. Cheng Li, for performing neutron powder diffraction on $Mn_3Fe_2Si_3$ using POWGEN at the Spallation Neutron Source (SNS), Oak Ridge National Laboratory.

Andreas Eich, for measuring $Mn_3Fe_2Si_3$ single crystal using neutron diffraction E-4 diffractometer at BER II research reactor.

Andrzej Grzechnik and **Andreas Eich**, for their help and support during my synchrotron beam time using 4-circle Huber single crystal diffractometer (P24-Beamline, DESY).

Devashibhai Adroja, **Nicolo Violini** and **Dr. Jörg Voigt** for their help and support during the MERLIN time of flight beamtime, installed at target station 1 of the ISIS Pulsed Neutron and Muon Source (STFC Rutherford Appleton Laboratory, U.K.).

DP. Joerg Persson for preparing the sample and supporting me during the sample preparation.

Berthold Schmitz for his technical support during the measurements at PPMS.

Dr. Markus Herrmann, **Dr. Igor Radelytskyi** and **Dr. Nikolaos Biniskos** for scientific discussion during beamtimes.

Frau Barbara Daegener for her help in many forms.

Dr. Emmanuel Kentzinger, Dr. Qdemat Asmaa, Dr. Tanvi Bhatnagar-Schöffmann, Dr. Patrick Schöffmann, Dr. Annika Stellhorn, Venus Rai, Nileena Nandakumaran and all other members of JCNS-2, thank you for all the good times we spent together, for the positive vibes and the sense of humor.

my **mother** and **father**, for their sacrifices and their patience with me, and their continuous and unconditional encouragement to me and their good faith in me.

Contents

1. Introduction

Over the past decade, the attraction for the magnetocaloric effect (MCE), has been increasing because of their considerable potential for magnetic refrigeration applications, promising higher energy efficiency than existing technologies. The magnetic refrigeration based on the MCE in magnetic materials has been promoted as a green alternative to conventional vapor-compression based refrigeration technologies, as the cooling efficiency around room temperature working with Gd as MCE material reaches 60%, whereas the best conventional gas compressor cycle refrigerators reach only 40% [1]. Therefore, the application of solid magnetic refrigerants reduces indirectly CO_2 emissions through efficiency benefits. Magnetic refrigeration systems can be built more compactly than compressor-based refrigeration systems and the noise of the refrigerators can be lowered. These advantages make the technology particularly interesting for air-conditioning and domestic refrigeration applications.

Among these materials, the compound series $Mn_{5-x}Fe_xSi_3$ has been studied intensely not only for the characteristics of the observed MCE's [5, 4, 2, 3], but also for elucidating the fundamental mechanisms [6, 7, 8].

The focus of the thesis is an experimental investigation of structural and physical properties of magnetocaloric $Mn_3Fe_2Si_3$ (x=2).

The thesis is structured in 9 chapters. The aim of chapter "Magnetocaloric effect and magnetic cooling" is to put the work in context. The MCE is first introduced with an illustrative description of its application (magnetic refrigeration cycle). As this thesis is focused on a better understanding of MCE materials, a general overview of magnetocaloric materials and their classes is presented. Next, information and physical properties of other members of the Mn_{5-x} Fe_x Si_3 series are introduced as a reference, before focusing on the material system investigated in this work ($Mn_3Fe_2Si_3$).

Chapter "Theoretical Background" provides the theoretical foundation for the data analysis. In the beginning a general information on antiferromagnetism is presented, followed by basic physics and thermodynamics of the Magnetocaloric effect. Also the basics of x-ray and neutron diffraction are introduced. At the end of this chapter, the concepts of magnetic space groups is introduced. Chapters "Experimental methods and instruments" and "Experimental process" describe the different experimental methods used in the synthesis and characterization of $Mn_3Fe_2Si_3$ material. Chapter "Macroscopic properties of the magnetocaloric compound $Mn_3Fe_2Si_3$" presents the results of the macroscopic property measurements of the compound $Mn_3Fe_2Si_3$. In chapter "Crystal structure of $Mn_3Fe_2Si_3$" I discuss structural parameters of $Mn_3Fe_2Si_3$, derived from synchrotron radiation single crystal diffraction at different temperatures.

The magnetic structure of $Mn_3Fe_2Si_3$ at different temperatures is explored in chapter "Magnetic structures of $Mn_3Fe_2Si_3$" using neutron powder diffraction.

A wrap up of the results from the different techniques and a conclusion about the relation between structure and magnetism in $Mn_3Fe_2Si_3$ are given in "Summary". The **Appendix** presents the procedures used for the data analysis, and supplementary information.

2. Magnetocaloric effect and magnetic cooling

2.1. Magnetocaloric effect

The MCE is thermodynamically described by the temperature change of a magnetic material upon adiabatic change of magnetic field. Its discovery is often attributed to Emil Warburg during his work on the magnetization of pure iron in 1881 [9]. However, according to Smith *et al* [10], MCE was in fact discovered experimentally in 1917 by Weiss and Piccard by observing a sizable and reversible temperature change in nickel near its Curie temperature [11]. Later, Giauque and MacDougall [12] independently proposed that by making use of the MCE one can attain very low temperature by adiabatically demagnetizing paramagnetic (PM) salts. In 1976, Brown constructed the first magnetic refrigeration system [13] using gadolinium as magnetic refrigerant, and demonstrated refrigeration by adiabatic demagnetization in the room-temperature range. In 1997, Pecharsky and Gschneidner [14] discovered a giant MCE in $Gd_5Si_{4-x}Ge_x$ alloys at 280 K associated with first-order magneto-structural transition. It was demonstrated that the temperature at which a large MCE exists could be tuned to between 280 K and 20 K by substituting Ge for Si. The simultaneous changes in in the crystal structure and magnetization at the transition temperature were expected to strongly influence both the lattice and the magnetic entropy. The reported MCE of $Gd_5Si_2Ge_2$ [14] was about 50 % larger than the up to then benchmark second order material, Gd metal.

2.2. Magnetic refrigeration

In practice, the core of magnetic refrigeration based on MCE is the temperature change of any suitable material in response to a changing magnetic field. The principle of a magnetic refrigeration cycle is based on the four following steps illustrated in Figure 2.1:

1) Adiabatic magnetisation: the temperature of the refrigerant increases due to the application of an external magnetic field.
2) Iso-field cooling: Heat is transferred to the thermal bath.
3) Adiabatic demagnetisation: the temperature of the refrigerant decreases due to the removal of magnetic field.
4) Iso-field heating: heat is loaded from the inside of the fridge. Once the refrigerant

and the heat load reach a thermal equilibrium state, the cycle finishes, and a new one begins.

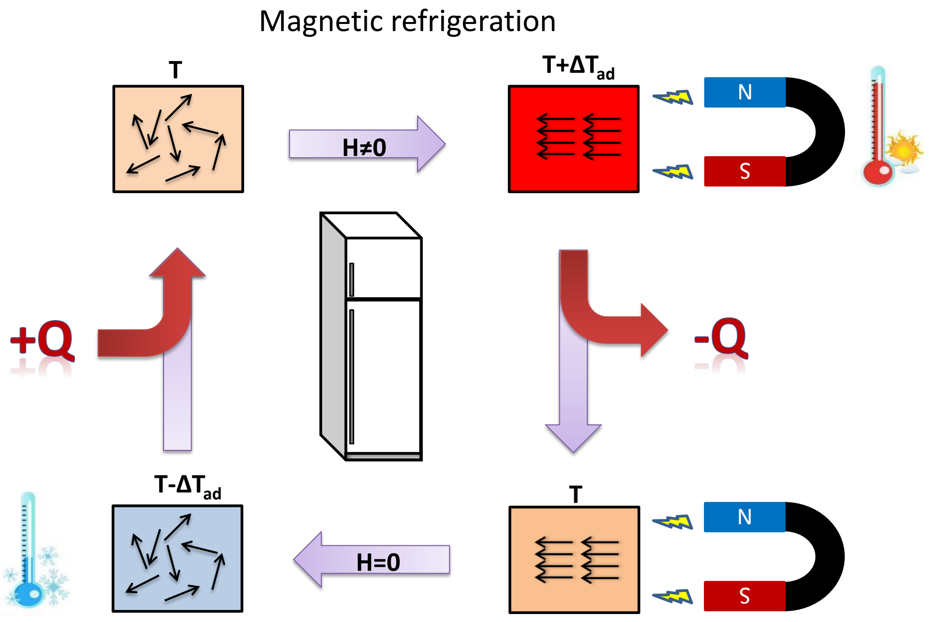

Figure 2.1.: Schematic representation of a magnetic refrigeration cycle. The figure is adapted from [15].

2.3. Magnetocaloric (MC) materials

2.3.1. Classification of MC compounds

MCE is considered as the keystone physical property behind an alternative technology for refrigeration both at room and at cryogenic temperatures. As the MCE is highest around magnetic phase transitions, the behavior of materials around these transitions is crucial for the performance of the refrigerant. MC compounds can be classified according to the order of their magnetic phase transition and can be divided into first order magnetic transition materials (FOMT) and second order magnetic transition materials (SOMT).

The FOMT often involve magnetostructural changes and show a discontinuity in the first derivative of the free energy. The discontinuity in the entropy is related to the enthalpy of transformation, called the latent heat. This reduces the efficiency of MCE. FOMTs reach the highest measured values of MCE. However, large magnetic fields are needed to trigger the magnetostructural transitions. This generally gives a high MCE in a narrow temperature range limiting the refrigeration capacity. Furthermore, most of the known FOMT material systems either contain very expensive elements (e.g. Gd), toxic elements (e.g. As) or have very complicated and expensive synthesis routes. On the other hand, for SOPTs, the first derivative of the free energy is continuous while the second derivative is discontinuous. SOMT materials in general have broader transitions with lower values of the MCE. Since in technological applications several other material properties are important, the choice between FOMT and SOMT materials is not as simple as it seems.

Figure 2.2 shows a comparison of some of the most investigated magnetocaloric materials in a plot of isothermal change of magnetic entropy for a magnetic field change between 0 and 5 T, $\Delta S_M(T)_{\Delta H=5T}$ versus transition temperature. Several materials such as $La(Fe_xSi_{1-x})_{13}$ [16], $La(Fe,Si)_{13}H$ [17], MnAs-based [5], and Fe_2P-based alloys [18] have shown interesting magnetocaloric performances. Also, the reference material Gd and compounds $Gd_5Si_2Ge_2$ [14] are among the best candidate materials for ambient temperature magnetocaloric devices. The magnitude of the MCE in the $MnFeP_{1-x}As_x$ [5] compounds is higher than Gd metal and comparable to compounds such as $Gd_5Si_2Ge_2$ [14] which undergo FOMT.

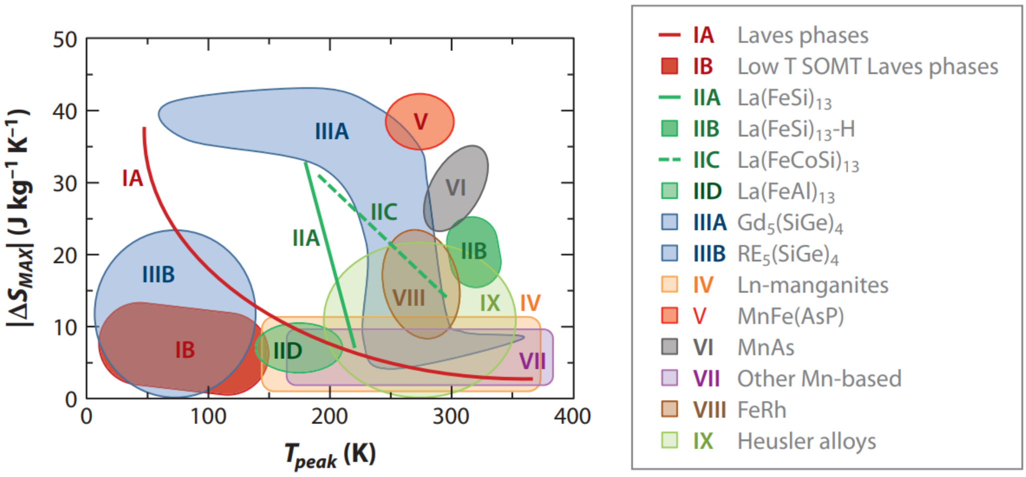

Figure 2.2.: Absolute value of maximum isothermal entropy change for field change from 0 to 5 T versus magnetic transition temperature for different families of MC materials, taken from [1]

The Giant MCE in the $MnFeP_{1-x}As_x$ compounds originates from a field-induced metamagnetic FOMT. Unlike to what happens in the $Gd_5Si_{4-x}Ge_x$ compounds, the symmetry of the hexagonal Fe_2P-type [18] structure does not change below and above the transition, but a sharp decrease of the a-axis lattice parameter and a sharp increase of the c-axis lattice parameter accompanies the transition from FM to PM phase.

The MCE is induced via the coupling of the magnetic sublattice with the applied magnetic field. For large MCE at room temperature, a flexible structure which accommodate substitutions by various ions is required, since this could cause structural changes, a variety of magnetic phase transitions and enhance the MCE properties.

Apart from the large magnetic entropy change and large adiabatic temperature change, there is a number of other criteria that must be taken into account for selecting materials for a commercial magnetic refrigeration design. These include: raw material cost, production cost, toxicity, recycling capability, low thermal and magnetic hysteresis for high operation frequency, and environmental impacts.

2.3.2. The $Mn_{5-x}Fe_xSi_3$ series ($0 \leqslant x \leqslant 5$)

The $Mn_{5-x}Fe_xSi_3$ ($0 \leqslant x \leqslant 5$) compounds are known for their magnetocaloric properties and they consist of abundant, non-toxic and cheap elements. The largest MCE reported for this system was observed in $Mn_{5-x}Fe_xSi_3$ ($x = 4$), e.g. for a field variation from 0 to 2 T, the MCE of this compound is $\Delta S_M(T)^{x=4} \approx 2\,\mathrm{J/kg\,K}$ [4, 3]. This is a modest MCE compared to MC compounds mentioned in the previous section such as $MnFeP_{1-x}As_x$ ($x = 0.45$) with $\Delta S_M(T)^{x=0.45} \approx 20\,\mathrm{J/kg\,K}$ for 0 to 2 T field change [5]. Despite this fact, the $Mn_{5-x}Fe_xSi_3$ compounds are considered as interesting model systems to develop a better understanding of the underlying mechanism of the MCE in multiple site driven magnetocaloric materials.

The reason for our interest on this family of compounds are:

First, they undergo a variety of magnetic phase transitions at different temperatures depending on their iron content, i.e. the predominant interactions change from antiferromagnetic (AF) to ferromagnetic (FM) when moving from the Mn end member to the Fe end member (see Figure 2.3 (left)). Second, the corresponding magnetic entropy changes show different shapes and magnitudes ranging from a negative MCE (x=0) to the modestly high positive magnetocaloric effect (MCE) of ~ 2J/kg K at a magnetic field change from 0 T to 2 T for $MnFe_4Si_3$ (x=4) (see Figure 2.3 (Right)). Third, it is possible to synthesize these materials as large single crystals, which is not achievable for most other magnetocaloric materials that are generally obtainable in polycrystalline form. This is an essential advantage for examining the underlying mechanism of the MCE, as a set of experimental techniques are only applicable if large single crystals are available.

2.3.2.1. Mn_5Si_3 (x=0)

The crystal structure of the parent compound Mn_5Si_3 belongs to the hexagonal space group $P6_3/mcm$ at room temperature with two distinct crystallographic positions for the Mn atoms, M1 (Wyckoff position (WP): 4d; 1/3,2/3,0) and M2 (Wyckoff position: 6g; x,0,1/4; $x \approx 0.2364$) [20]. The Si atom also resides on a 6g position with (x,0,1/4; $x \approx 0.5957$) [20]. Upon the substitution of Mn for Fe in $Mn_{5-x}Fe_xSi_3$ series, Fe occupies preferentially the M1(WP:4d) position [20], however, without reaching complete site order.

The M1 (WP:4d) atom is surrounded by 6 Si atoms at distances of approximately 2.4 Å in the form of a distorted octahedron [$M1Si_6$] (see Figure 2.4). These octahedra share triangular faces with their analogs forming infinite chains of composition $_\infty[M1Si_3]$ along the c axis [20, 3, 2]. The M2 atoms are interconnected to form distorted empty octahedra [$\square$ $(M2)_6$]. They also share common triangular faces and

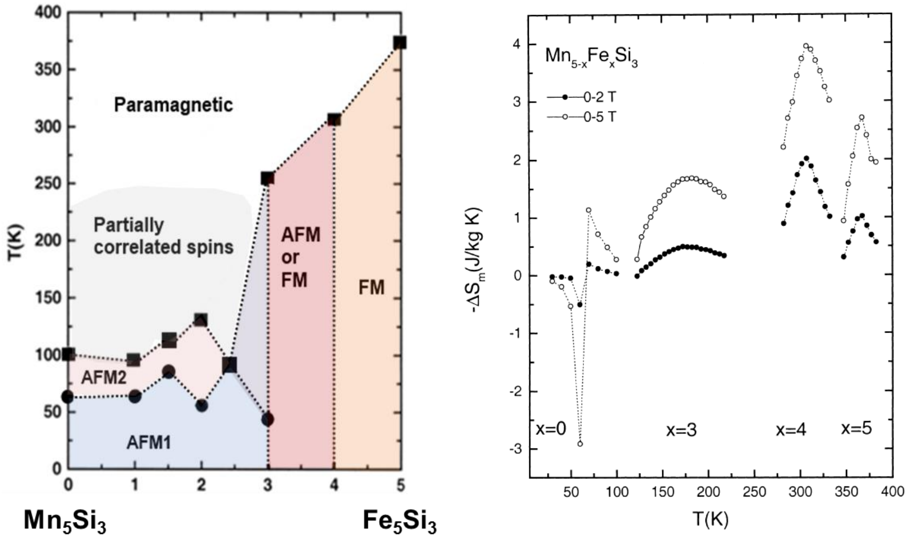

Figure 2.3.: (Left) Magnetic phase diagram adapted from [4], additional data points (x=1.5 and x=2.5) are taken from [19]. (Right) magnetic entropy changes for two different magnetic field variations for the Mn_{5-x} Fe_x Si_3 system (taken from [4]).

form infinite chains of composition $_\infty[\,\square(\mathrm{M2})_3]$ along the *c*-direction. Neighbouring $_\infty[\mathrm{M1Si_3}]$ chains share common edges with each other, forming channels occupied by the chains of empty octahedra $[\square\ (\mathrm{M2})_6]$ [20, 3, 2].

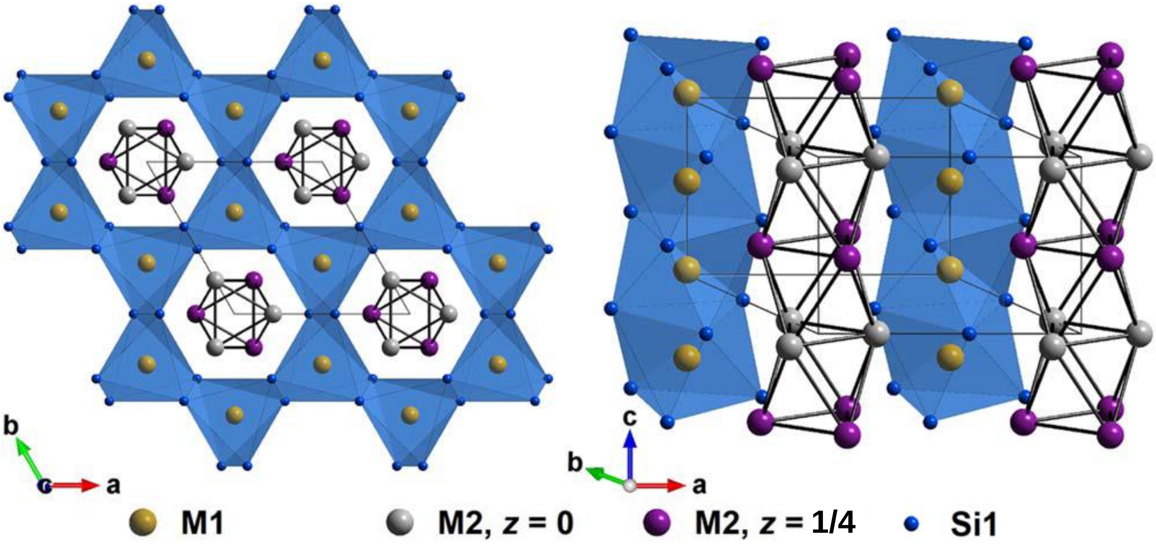

Figure 2.4.: Crystal structure of Mn_{5-x} Fe_x Si_3 (taken from [21]).

In the Fe-rich compounds of the Mn_{5-x} Fe_x Si_3 system, no temperature-induced structural phase transitions are observed [20]. However, the parent compound Mn_5Si_3

has a structural phase transition at 99 K where the space group symmetry changes from hexagonal $P6_3/mcm$ to orthorhombic $Ccmm$ with lattice parameter $a_{ortho} \approx a_{hex}$, $b_{ortho} \approx a_{hex} + 2b_{hex}$, $c_{ortho} \approx c_{hex}$ (see Appendix A.10). This structural phase transition coincides with the magnetic transition from a paramagnetic (PM) to an antiferromagnetic state (AF2) [2, 22]. In $Ccmm$ space group the M2 positions (WP6g) split into two sets of inequivalent positions, so that in the AF2 phase three symmetrically independent sites are available for Mn, designated M1 (WP:8e; 0,y,0), M21 (WP:4c; x,0,1/4), and M22 (WP:8g; x,y,1/4) in the following. Additional magnetic reflections, which appear in the AF2 phase, can be indexed with a propagation vector of (010) referring to the orthorhombic setting. They appear at reflection positions violating the extinction rules for C-centering ($hkl : h + k = 2n + 1$). At 90 K this phase comprises an antiferromagnetic collinear arrangement of Mn magnetic moments on the M22 position which have their magnetic moments of magnitude 1.48(1) μ_B, pointing along the b-direction, while M1 and M21 sites carry no static magnetic moments (see Figure 2.5) [2, 22]. A small temperature dependent deviation from collinearity was observed, 3° of tilt at 80 K and 8° of tilt at 70 K (Figure 2.5), with respect to the b crystallographic direction. Nevertheless AF2 was referred to as collinear phase in the literature [22, 2].

At 60 K the magnetic ordering is changed due to a phase transition taking place at ~62(1)K [2]. The magnetic structure of the low temperature AF1 phase is characterized by a monoclinic spin arrangement although the atomic positions can still be described with the non-centrosymmetric orthorhombic symmetry $Cc2m$. In this phase, three sublattices have to be be considered. They are formed by the magnetic moments on M22 and M23 with moments pointing into different directions forming a complex non-collinear antiferromagnetic structure [23, 2], and the M1 sites which carry a smaller magnetic moment.

At the transition temperature from the AF2 to AF1 phase a discontinuous expansion in the c-lattice parameter is observed. According to the literature, this expansion leads to a larger Mn1-Mn1 distance ($= 0.5\ c$) in the AF1 phase, this way enabling the ordering of the moments on the Mn1 site, which is suppressed by the smaller Mn1-Mn1 distance in the AF2 phase [22](see Figure 2.5).

Discrepancies exist in literature concerning the presence of magnetic moments on Mn21 and Mn22 sites: while according to [23] no ordered magnetic moment was observed, a very small magnetic moment was observed on these sites in [2]. Based on neutron powder diffraction data, Gottschlich et al [2] identify an additional low-temperature high-field phase, designated AF1′, in which the ordered moment on the Mn1 site presumably disappears again. The end member Mn_5Si_3 (x=0) exhibits an inverse MCE [5, 4], with an isothermal entropy change of 3 J/kg K for a field change of 5 T at the magnetic phase transitions near 62 K between the non-collinear AF1 phase and the collinear AF2 phase. The entropy change becomes negative slightly above the transition temperature from AF1-AF2 and decreases with increasing temperature till the paramagnetic state is reached [5].

Recently, it has been demonstrated that the inverse MCE can be attributed to changes in the magnetic excitation spectrum across the phase transition. In the $AF1$

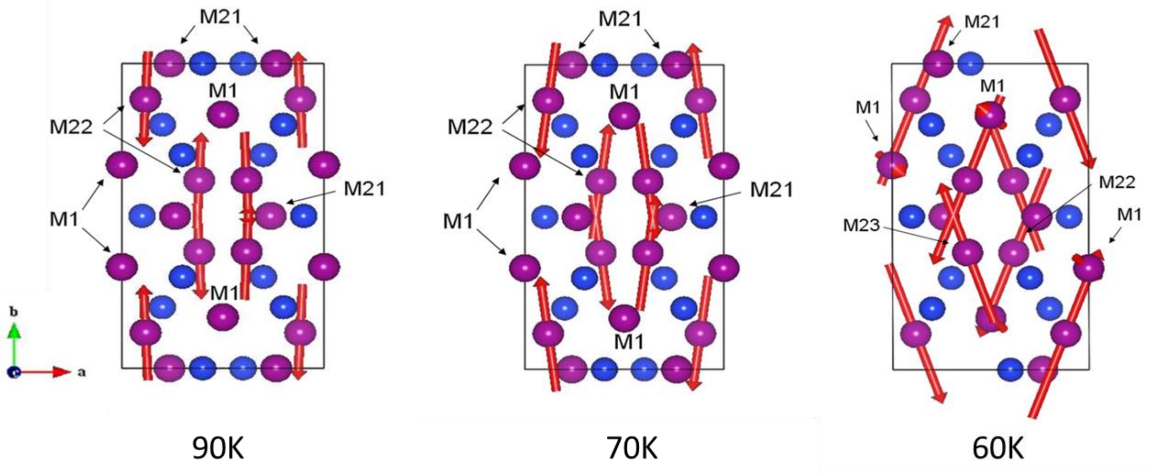

Figure 2.5.: Projection in the (a,b) plane of the orthorhombic unit cell of Mn_5Si_3 at 60, 70, 90 K (taken from [2]). For the AF1 phase (60 K) the Mn23 and Mn24 sites correspond to the Mn22 sites of the AF2 phase (70 K and 90 K) [23, 2].

phase the spectrum is dominated by spin waves, while in the $AF2$ phase low energy spin fluctuations become strong and increase the magnetic entropy significantly [6]. The macroscopic response of Mn_5Si_3 has been recently revisited by means of Hall effect measurements by Sürgers *et al.* [24] and magnetization measurements up to 14 T by Das *et al.* [25]. Das *et al.* observed a small change in the M(H) isotherms slope below of 66 K, when moving from the $AF1$ to the $AF1'$ phase. In addition to that, a sharp change in M values of the M(H) isotherms was observed which is associated to the $AF1'$ to $AF2$ transition. Both the transition fields are found to be shifted toward the lower value with increasing temperature [25].

2.3.2.2. $MnFe_4Si_3$ (x=4)

On the basis of neutron and X-ray single crystal diffraction study on the ferromagnetic compound $MnFe_4Si_3$ at 380 K [3], it was shown that, in contrast to the parent structure, a partial ordering of Mn and Fe takes place on the M2 sites, leading to a lowering of the symmetry to $P\overline{6}$ space group with six symmetrically independent sites ($M1_a/M1_b$; $M2_a/M2_b$; $Si1_a/Si1_b$). The M1a/M1b sites are nearly exclusively occupied by Fe, while the M2a/M2b sites have a mixed occupancy of Mn and Fe. Below 300 K, the sites with mixed occupancy of Mn/Fe carry an ordered magnetic moment of approximately $1.5(2)\mu_B$ pointing perpendicular to the c-direction, whereas, for the position which is occupied by Fe, the refined magnetic moment is smaller than the error (see Figure 2.6). [3].

The magnetization of $MnFe_4Si_3$ rapidly reaches about 1.7(1) μ_B per metal atom at a field of 0.5 T at a temperature of 50 K [3], while, the average magnetic moment per iron atom of the ferromagnetic Fe_5Si_3 is about 1.32 μ_B in a field of 5 T[4]. The

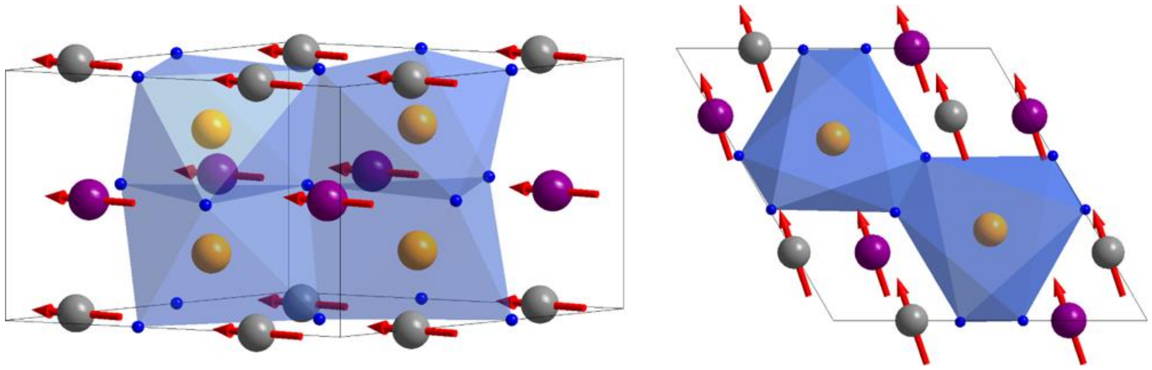

Figure 2.6.: Schematic diagram illustrating the ferromagnetic structure of $MnFe_4Si_3$ at 200 K in magnetic space group Pm'. Left, slightly tilted projection approximately along [110]-direction; right, projection along [001]-direction (taken from [3]).

fact that the total magnetic moment in $MnFe_4Si_3$ is higher than the total magnetic moment in Fe_5Si_3 can be attributed to the relatively large value of the Mn moment when forced into a ferromagnetic moment arrangement.

The large magnetic moment of the Mn atoms coupled parallel to the Fe moments can also explain the modestly large direct MCE of $MnFe_4Si_3$ (x=4) with an isothermal entropy change of $-\Delta_{iso}$= 4 J/kg K for a field change of 5 T [3], which is higher than the isothermal entropy change of Fe_5Si_3, $-\Delta_{iso}$= 2.7 J/kg K for the same field change [4] (see Figure 2.3).

2.3.2.3. $Mn_3Fe_2Si_3$ (x=2)

This thesis is focused on the compound $Mn_3Fe_2Si_3$ (x=2; space group $P6_3/mcm$ at RT) which show some similarities to the Mn_5Si_3 compound. Neutron studies on this compound shows a high degree of structural order of the paramagnetic ions with Fe being preferentially incorporated into the M1 (4d) site which is coordinated octahedrally by Si, while Mn preferentially occupies the remaining M2 (orthorhombic: M21/M22) positions [20]. According to earlier magnetization measurements on polycrystalline material, the compound has a transition from the paramagnetic to the $AF2$ phase at approximately 125 K and a second transition from $AF2$ to $AF1$ at approximately 70 K [4]. The magnetization has been measured in pulsed fields up to 38 T, without a hint for an additional transition [4]. As a consequence of the incorporation of Fe into the structure, one expects significant changes in the magnetic and structural properties. We therefore studied structural and magnetic properties of single crystals and powder of $Mn_3Fe_2Si_3$ to elucidate this effect further. This way, we hope to contribute to a better understanding of the MCE in the whole series of compounds.

3. Theoretical Background

3.1. Magnetic Order: Antiferromagnetism

The Heisenberg model describes the exchange interaction between localized spins in a crystal, its Hamiltonian reads:

$$H = -\sum_{i,j} J_{ij} \vec{S}_i \cdot \vec{S}_j \tag{3.1}$$

The sum runs over all sites in the crystal and J_{ij} is the exchange integral between atoms i, j. A positive $J_{i,j}$ refers to a ferromagnetic exchange, i. e. it favors a parallel alignment of spins on site i and j, while $J_{i,j} < 0$ tends to align the spins on sites i, j in an antiparallel manner.

Antiferromagnetic materials exhibit a small but positive susceptibility $\chi > 0$, at all temperatures (T)[26, 27]. In zero applied field the spins of an antiferromagnet are ordered in an anti-parallel arrangement with zero net magnetic moment at temperatures below the ordering temperature, which is called the Néel temperature T_N. Above T_N, where the substance is paramagnetic, the moments are oriented randomly resulting in a zero net magnetization (M) in the absence of a magnetic field.

To model magnetic interactions, Weiss Mean Field Theory of Ferromagnetism assumed that S_j in eq. 3.1 can be replaced by its average value $< S_j >$ which is proportional to the magnetization M. The interaction then acts as an internal field H_{int} [28]. If there is an external field H, then the total field acting on the i^{th} spin is :

$$H_{tot} = H + H_{int} = H - |\lambda| M, \tag{3.2}$$

where λ is the molecular field coefficient. This quantity is proportional describes the interaction of a magnetic ion with the others [29].

The case of an antiferromagnet is the model of a crystal with two sublattices, A and B with equal sublattice magnetization and anti-parallel spin alignment. Since for an AF the exchange integrals are negative, then λ is also negative. In general, the interaction between the nearest neighbor (between two sublattices A and B) can be significantly different from the interaction between the next-nearest neighbor (witin the same sublattice). The mean exchange fields acting on each sublattice of an antiferromagnet may be written as [30]:

$$H_{intA} = -\Gamma M_A - |\lambda| M_B \ ; \quad H_{intB} = -\Gamma M_B - |\lambda| M_A \tag{3.3}$$

Γ is a constant which expresses the contribution to the molecular field from the same sublattice. Applying the mean-field treatment one obtains the Curie-Weiss temperature $\theta = -C(|\lambda| + \Gamma)$ and the AF ordering sets in the Neel temperature $T_N = C(|\lambda| - \Gamma)$. Then, we obtain the ratio relating the strength of inter- and intra-sublattice interactions [30].

$$\frac{T_N}{\theta} = -\frac{|\lambda| - \Gamma}{|\lambda| + \Gamma} \tag{3.4}$$

For the susceptibility one can derive the expression:

$$\chi = \lim_{H \to 0} \frac{M}{H} = \frac{C}{T - C(|\lambda| + \Gamma)} = \frac{C}{T + \theta}, \tag{3.5}$$

By fitting the linear part of the plot of $\frac{1}{\chi}$ as function of temperature where the Curie-Weiss law is obeyed (Paramagnetic regime), we can extract the characteristic temperature θ from the intercept with the abszissa and Curie constant from the slope of the linear fit. As result, we can calculate the effective paramagnetic moment by the following relation expressed in SI units [31]:

$$\mu_{eff} = \sqrt{\frac{3k_B C}{N \mu_0 \mu_B^2}}, \tag{3.6}$$

where k_B is the Boltzmann's constant, N is the number of magnetic atoms per unit volume, μ_B is the Bohr magneton and μ_0 is permeability of free space, the μ_{eff} is measured in Bohr magnetons per formula unit. According to the mean-field approximation, μ_{eff} can be also given by $\mu_{\text{eff}}^2 = xg^2 S(S+1)\mu_B^2$, where x is the fraction of magnetic ions per formula unit, g is their gyromagnetic factor, and S their spin quantum number [32]. The effective paramagnetic moment μ_{eff} for a system containing more than one type of magnetic ion can be treated as separate magnetic systems with the same ordering temperature. e.g. μ_{eff} for system with two magnetic ions can be expressed as [32]:

$$\mu_{\text{eff}} = \sqrt{\mu_{\text{eff}(1)}^2 + \mu_{\text{eff}(2)}^2}, \tag{3.7}$$

Below T_N, the susceptibility of antiferromagnets depends on the direction of the applied field relative to the spin axis. For a simple antiferromagnet, applying a small magnetic field perpendicular to the axis of the spins invokes a slight tilt of the spins against the molecular field so that a component of magnetization is produced along the applied magnetic field. The susceptibility $\chi_\perp \neq 0$ does not depend on temperature below T_N.

In the case of the parallel orientation of the magnetic field to the axis of the spins, the parallel susceptibility $\chi_\parallel$ goes to zero as $T \to 0$ and increases smoothly with increasing temperature up to T_N [33].

3.2. Basic physics and thermodynamics of Magnetocaloric effect

The magnetocaloric effect is an effect characterized by the adiabatic temperature change ($\Delta \mathrm{T}_{ad}$) or the isothermal entropy change (ΔS_{iso}) due to the application of the magnetic field H. The total entropy ΔS_{iso} and adiabatic temperature change ΔT_{ad} are shown in a temperature-entropy (TS) diagram between two magnetic isofield curves without magnetic field (H=0) and a non-zero magnetic field (H≠0) (see Figure 3.1) for a material featuring a direct MCE. In the isothermal process A-B, the increase of the applied magnetic field orders magnetic moments in the material, which results in a lowering of the magnetic entropy ΔS_M and consequently in a lowering of the total entropy ΔS_{iso}. In the process A-C, the magnetic field is applied adiabatically (the total entropy remains constant).

The total entropy of a magnetic substance at constant pressure and volume depends on both magnetic field H and temperature, T. It consist of lattice (S_l) and electronic contributions (S_e) besides the magnetic contributions from the atomic magnetic moments (S_m) (see Eq.3.8). In order to conserve the total entropy under adiabatic conditions, the system is forced to increase its temperature. In the adiabatic conditions, the reduction of the magnetic entropy is compensated by an increase in the lattice and/or electronic entropy.

$$\Delta S_l(T,H) + \Delta S_e(T,H) + \Delta S_m(T,H) = 0 \tag{3.8}$$

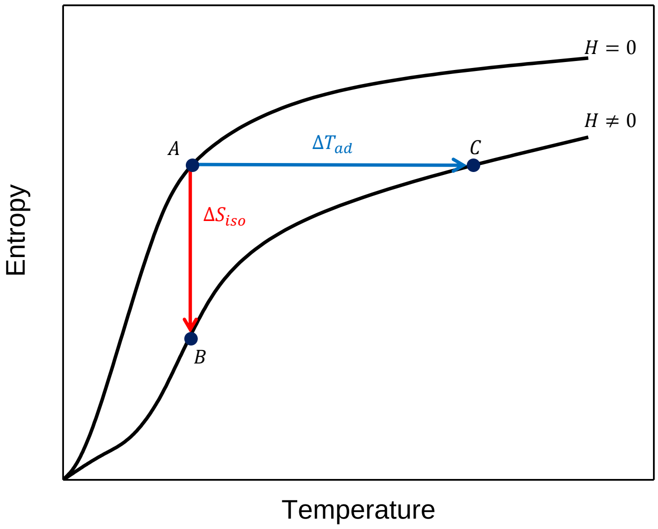

Figure 3.1.: Schematic Entropy-Temperature diagram for constant pressure and two different magnetic fields

In order to explain the origin of the magnetocaloric effect, we describe the thermodynamics of a magnetic material under a magnetic field using the description of the Gibbs free energy, G.

$$G = U - TS + PV - M\mu_0 H \tag{3.9}$$

Where U, S, V, M and μ_0 are the internal energy, total entropy, volume, magnetization of the system and permeability of free space, respectively. By using the first law of thermodynamics: $dU(T,P,H) = TdS + \mu_0 HdM - PdV$, we can write the variation of the Gibbs free energy as:

$$dG(T,P,H) = -SdT + VdP - M\mu_0 dH \tag{3.10}$$

Therefore, we can determine the expression for S, V and $\mu_0 M$ from the first derivative of G, as follows:

$$S(T,P,H) = -\left(\frac{\partial G}{\partial T}\right)_{H,P} \tag{3.11}$$

$$V(T,P,H) = -\left(\frac{\partial G}{\partial P}\right)_{T,H} \tag{3.12}$$

$$\mu_0 M(T,P,H) = -\left(\frac{\partial G}{\partial H}\right)_{T,P} \tag{3.13}$$

The Maxwell relation relating the entropy with the the magnetization, can be obtained by making the derivative for equations 3.11 and 3.13:

$$\left(\frac{\partial S}{\partial H}\right)_{T,P} = \mu_0 \left(\frac{\partial M}{\partial T}\right)_{H,P} \tag{3.14}$$

Considering the total entropy of the system, $S(T,P,H)$, the total differential of the total entropy can be written as:

$$dS(T,P,H) = \left(\frac{\partial S}{\partial P}\right)_{T,H} dP + \left(\frac{\partial S}{\partial T}\right)_{P,H} dT + \mu_0 \left(\frac{\partial S}{\partial H}\right)_{P,T} dH \tag{3.15}$$

By using the Maxwell relation 3.14 for an isothermal and isobaric process, we can derive the change in entropy as function of the magnetization M :

$$dS = \mu_0 \left(\frac{\partial M}{\partial T}\right)_{H,P} dH \tag{3.16}$$

i. e. the entropy changes strongly, when the magnetization changes strongly with temperature.

The isothermal entropy change can then be calculated by integrating the Eq.3.16 between two magnetic fields H_i and H_f.

$$\Delta S_M(T,P,\Delta H) = \mu_0 \int_{H_i}^{H_f} \left(\frac{\partial M}{\partial T}\right)_{H,P} dH \tag{3.17}$$

The entropy change can be also expressed in terms of heat capacity $C_{H,P}$ under constant pressure and magnetic field:

$$C_{H,P}(T) = T\left(\frac{\partial S}{\partial T}\right)_{H} \tag{3.18}$$

This permits us to calculate the isothermal entropy change from the evolution of the heat capacity as a function of temperature:

$$\Delta S_M(T,\Delta H) = \int_0^{T_f} \frac{C_{H_f,P}(T) - C_{H_i,P}(T)}{T} dT \tag{3.19}$$

Under adiabatic $dS = 0$ and isobaric $dP = 0$ conditions, Eq.3.15 can now be presented as:

$$dT = -\mu_0 \left(\frac{\partial S}{\partial H}\right)_T \left(\frac{\partial T}{\partial S}\right)_H dH \tag{3.20}$$

By using the Maxwell relation and the definition of the specific heat under constant field (Eq.3.18), we can integrate from H_i to H_f to get of the adiabatic temperature change ΔT_{ad}:

$$\Delta T_{ad}(T,\Delta H) = -\mu_0 \int_{H_i}^{H_f} \left(\frac{T}{C_{H,P}(T)}\right)_H \left(\frac{\partial M(T,H)}{\partial T}\right)_H dH \tag{3.21}$$

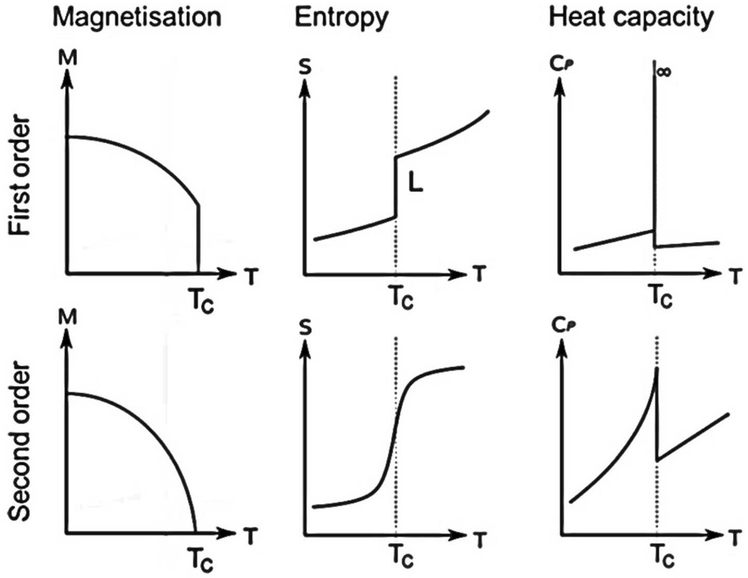

Figure 3.2.: The behavior of the magnetization, free energy, entropy, and heat capacity according to the first-order and second-order phase transitions. Adapted from [34].

As already mentioned in first chapter, the MCE is expected to be large around a phase transition when the temperature derivative of the magnetization $\left(\frac{\partial M}{\partial T}\right)_H$ is large. In the first-order phase transitions, the change of entropy of a system is discontinuous. This is a result of the latent heat associated with the transition. The heat capacity therefore goes to infinity when the transition point is approached from either side (see Figure3.2). In the case of second-order transitions, there is no latent heat and therefore the change of entropy of a system is continuous. The specific heat is expected to be a discontinuous parameter as it is proportional to the first derivative of entropy with temperature (see Figure3.2).

The magnetocaloric effect is categorized in the following way: *a*) Direct MCE, where $\left(\frac{\partial M}{\partial T}\right)_H < 0$ resulting in $\Delta S_{iso} < 0$ and $\Delta T_{ad} > 0$ and *b*) and indirect MCE, where $\left(\frac{\partial M}{\partial T}\right)_H > 0$ resulting in $\Delta S_{iso} < 0$ and $\Delta T_{ad} < 0$. A direct MCE is typically been observed in the vicinity of a ferromagnetic-paramagnetic phase transition as the magnetic entropy is reduced by suppressing the spin fluctuations. The indirect MCE, namely an increase of the magnetic entropy, means, that spin fluctuations are induced by application of a field.

3.3. Diffraction

3.3.1. X-ray diffraction

An ideal crystal consists of a periodic arrangement of atoms. Within the crystal parallel lattice planes decorated with atoms are identified by Miller Indices (hkl) which are defined on the basis of the reciprocals of the intercepts of the plane with the crystallographic axes. The distance between parallel rows of lattice planes hkl of atoms is commonly denoted as d-spacing (d_{hkl}).

An incoming x-ray beam with a wavelength comparable to the spacings of the atoms in the crystal interacts with the electron clouds of the atoms. At certain angles θ, when the Bragg condition is fulfilled [35], constructive interference between the diffracted waves occurs and diffracted intensity from the particular lattice plans can be observed with a detector.

The electron density distribution as a function of position xyz within the unit cell is described as :

$$\rho_{xyz} = \frac{1}{V}\sum\nolimits_{hkl} F_{hkl} \cdot exp(i \cdot (h \cdot x + k \cdot y + l \cdot z)). \tag{3.22}$$

Eq. 3.22 represents the Fourier transform between the real space (where the atoms are represented by ρ_{xyz}) and the reciprocal space (diffraction pattern) represented by the structure factors F_{hkl} (Note: in crystallography it is common to include 2π in the argument of the functions). V and xyz represents the volume of the unit cell and the position of the atoms in the unit cell, respectively. F_{hkl} describes both the amplitude and the phase of the diffracted waves from scattering planes hkl and it is given by:

$$F_{hkl} = \sum\nolimits_{N}^{n=0} f_n \cdot exp(i \cdot (h \cdot x_n + k \cdot y_n + l \cdot z_n)). \tag{3.23}$$

where the sum is over all the atoms n in the unit cell, f_n is the scattering factor of atom n, and x_n, y_n and z_n describe the position of the n-th atom the unit cell.The coordinates x_n, y_n and z_n refer to the coordinate system defined by the lattice parameter a, b, c.

The atomic scattering factor is a measure for the scattering power of an individual atom and derived by considering the interference of all the waves scattered by the electrons in this atom.

When the electron density distribution has spherical symmetry, the atomic scattering factor can be presented and plotted as a function of the magnitude of the scattering vector (see Figure 3.3):

$$|\vec{Q}| = 4\pi sin\frac{\theta}{\lambda}, \tag{3.24}$$

where θ is the angle between the incident X-ray beam and the diffracting lattice plane, and λ is the wavelength of the X-rays. The atomic scattering factor depends on the type of atom and the direction of scattering, so that it reaches a maximum in the same direction of the incident X-rays $Q = 0$ where f_n is equal to the atomic number Z, and decreases as a function of the angle of incidence[36] due to the destructive interference effects between the Z electrons scattered waves.

of waves scattered from electrons of an atom.

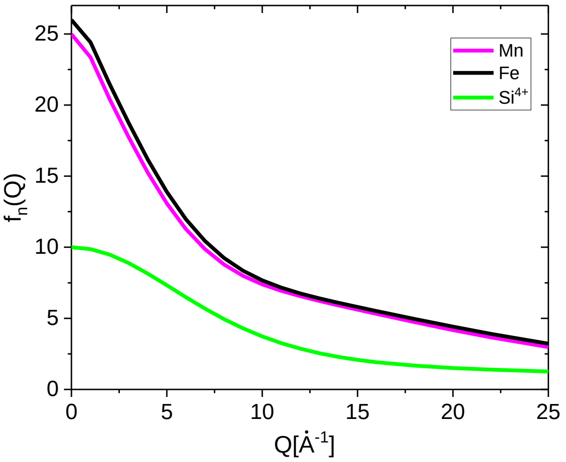

Figure 3.3.: The variation in the atomic scattering factor for Mn, Fe and Si elements as function of Q

The diffraction pattern can be calculated by a Fourier transform of the electron density if there is prior knowledge of the electron density. To obtain the electron density from the diffraction pattern one has to apply an inverse Fourier transform. For this, the amplitude and the phase of the structure factor are needed. However, in the diffraction experiment one only gets the modulus of the structure factor $|F_{hkl}|$ proportional to the square root of the intensity measured on the detector, while the value of the phase $(i \cdot (h \cdot x_n + k \cdot y_n + l \cdot z_n))$, which is an essential piece of information, is lost. This is known as the phase problem of crystallography.

Different methods were developed to reconstruct the missing phase information [37] which will not be described in detail here, as, in our case, we used a structural model from the literature as a starting model, and calculated initial phases based on it.

So far, all the above equations are written by considering rigid atoms in unit cell at the absolute temperature of 0 K. For temperatures T > 0 K, the atoms are vibrating about their equilibrium position. These vibrations cause a drop-off in the intensity of the Bragg peaks with increasing θ angle, giving rise instead to diffuse intensity distributed in the reciprocal space. These diffuse intensities give information about the dynamics of the atoms constituting the crystal, and they are called thermal diffuse scattering or inelastic phonon scattering.

So, in X-ray diffraction, the intensity drop-off as a function of θ arises from the drop in the atomic scattering factor and from atomic vibrations that can be represented by the exponential function called the Debye-Waller factor W [37]:

$$W = exp\left(-B\left(\frac{sin(\theta)}{\lambda}\right)^2\right) \tag{3.25}$$

where $B = 8\pi^2 U$ and where $U =< u^2 >$ is the mean quadratic atomic displacement. As a result the expression for $|F_{hkl}|$ becomes:

$$F_{hkl} = \sum_N^{n=0} f_n \cdot exp(2 \cdot \pi \cdot i \cdot (h \cdot x_n + k \cdot y_n + l \cdot z_n)) \cdot W_n \tag{3.26}$$

In crystal structures, each atom vibrates in general anisotropically, and the electron density for an atom has the form of a triaxial ellipsoid. These ellipsoids must be constrained in accordance with the site symmetry, and their shape and orientation can be determined by six atomic anisotropic displacement parameters (ADPs). They are the diagonal and off diagonal terms of a three-by-three matrix:

$$U = \begin{pmatrix} U_{11} & U_{12} & U_{13} \\ U_{21} & U_{22} & U_{23} \\ U_{31} & U_{32} & U_{33} \end{pmatrix}. \tag{3.27}$$

The diagonal terms U_{11}, U_{22} and U_{33} are related to the lengths of the principal axes of the vibration ellipsoid, and the "off diagonal" terms U_{13},U_{23},U_{12} refer to the orientation of the ellipsoid with respect to the reciprocal axes. For isotropic vibrations, the ellipsoids would have all off-diagonal terms equal to zero, and all diagonal terms are identical i.e. the thermal ellipsoids are spherical.

If we assume that the diffraction vector is referred to the basis of the reciprocal lattice $H = ha_1^* + ka_2^* + la_3^*$ and the atomic displacement vector to the basis of the direct lattice $U = \Delta x a_1 + \Delta y a_2 + \Delta z a_3$ (with $a_1 = a$, $a_2 = b$, $a_3 = c$), then we can replace the six-parameter description of the anisotropic displacement parameter by a single quantity using a new relation [38, 39]:

$$U_{eq} = \frac{1}{3} \sum_{i=1}^{3} \sum_{j=1}^{3} U_{ij} a_i^* a_j^* a_i a_j, \tag{3.28}$$

.

3.3.1.1. Absorption correction

As X-ray beam of intensity I_0 travels a distance L through a homogeneous isotropic material, a percentage of the X-rays will be absorbed by the sample according to the following equation [41, 40]:

$$T = \frac{I}{I_0} = e^{-\mu \cdot L}, \tag{3.29}$$

I is the diffracted beam intensity which is attenuated relative to the incident beam intensity I_0, T is the transmission factor that can adopt values between 0 and 1. L is the total length equal to the sum of the path lengths traversed by the incident beam ($L1$) and diffracted beam ($L2$). The absorption correction is then given by [41]:

$$A = \frac{1}{T} \tag{3.30}$$

Despite the simplicity of the exponential expression, the degree of absorption is generally complex to calculate since the different volume (V) elements within the sample are not constrained to have the same values of L. The absorption from the entire sample is thus represented by the volume integral. Therefore the transmission coefficient can be represented as[41, 40]:

$$T = \frac{1}{V} \int e^{-\mu \cdot L} dV, \tag{3.31}$$

3.3.2. Neutron diffraction

3.3.2.1. Nuclear scattering

Neutrons interact with the nucleus via the strong-force interaction, in contrast to x-rays or electrons which interact with the electron cloud. The interaction between an incident neutron at position r and the n-th atomic nucleus positioned at R_n can be approximated by a delta function [42]:

$$V_{nuc}(\vec{r}) = \frac{2\pi\hbar^2}{m} \sum_n b\delta(\vec{r} - \vec{R}_n) \tag{3.32}$$

The proportionality factor b is called neutron scattering length, it can vary greatly between elements of similar atomic number, and even between isotopes of the same element. As an example, there is a very high contrast between Mn (b=-3.73 fm) and Fe (b=9.45 fm), for which x-rays are insensitive since these two elements have nearly the same number of electrons. Neutron diffraction is also sensitive to the hydrogen atom even in the presence of such heavy elements as uranium, which is difficult to detect by x-rays since hydrogen in bonds has often less than one surrounding electron [43].

The strength of the scattering length b depends on the intra-nuclear structure and is therefore different for different isotopes. This fact gives rise to coherent scattering and incoherent scattering. The coherent part shows interference effects between scattered neutron waves from different atoms, and provides information about the nuclear structure. In the incoherent scattering part, there is no interference between waves scattered by different nuclei. Actually, it corresponds to the scattering from single atoms, which subsequently superimpose in an incoherent manner (The intensities scattered from each nucleus just add up independently), and causes an isotropic background in neutron experiments.

In the following, we will focus only on coherent scattering, where, the partial differential cross-section for elastic coherent nuclear scattering is derived as:

$$\left(\frac{d\sigma}{d\Omega}\right)_{nuc,coh} = \frac{8\pi^3}{v_0}\sum_{\vec{\tau}}|F_{Nuc}(\vec{Q})|^2\cdot\delta(\vec{Q}-\vec{\tau}), \tag{3.33}$$

where v_0 is the unit cell volume, $\vec{\tau}$ is a reciprocal lattice vector, $\vec{Q} = \vec{k_f} - \vec{k_i}$ is the scattering vector, $\vec{k_i}$ and $\vec{k_f}$ describe the direction of the incident and diffracted neutron beam with respect to the crystal, respectively. The nuclear structure factor is given by [44]:

$$F_{Nuc}(Q) = \sum_{N}^{n=0} b_n\cdot exp(i\cdot\vec{Q}\cdot r_n)\cdot W_n \tag{3.34}$$

3.3.2.2. Magnetic scattering

The dipolar interaction between the neutron magnetic moment and the magnetic moment of atoms with unpaired electrons leads to a magnetic neutron scattering contribution. The interaction potential of a neutron in spin state σ_N and a propagating electron with momentum $\vec{p}$ and spin $\vec{s}$ can be written as follows [42]

$$V_{mag}(\vec{r}) = -\gamma\mu_N 2\mu_B\vec{\sigma_N}\left[\nabla\times\left(\frac{\vec{s}\times\vec{R}}{R^3}\right)+\frac{\vec{p}\times\vec{R}}{\hbar R^3}\right], \tag{3.35}$$

where γ=1.913 is the gyromagnetic factor of the neutron, μ_N is the nuclear magneton and μ_B is the Bohr magneton. $\nabla\times\left(\frac{\vec{s}\times\vec{R}}{R^3}\right)$ and $\frac{\vec{p}\times\vec{R}}{\hbar R^3}$ are due to the intrinsic electron spin and the orbital motion of the electron, respectively. In the case of magnetic coherent Bragg scattering, the partial differential cross-section is:

$$\left(\frac{d\sigma}{d\Omega}\right)_{mag,coh} = \frac{1}{N_m}\frac{8\pi^3}{v_0}\sum_{\vec{\tau_M}}|F_{M\perp}(\vec{\tau_M})|^2\cdot\delta(\vec{Q}-\vec{\tau_M}), \tag{3.36}$$

N_m is the number of magnetic ions $\vec{\tau_M} = \vec{\tau}\pm\vec{k}$ is the reciprocal vector of the magnetic structure. $\vec{k}$ is called the propagation vector that describes the relation between moment orientations of equivalent magnetic atoms in different nuclear unit cells. $\vec{F_{M\perp}}$ denotes the component of the Fourier transform of the samples magnetization, which is perpendicular to the scattering vector $\vec{Q}$: $\vec{F_{M\perp}} = \vec{Q}\times\vec{F_M}\times\vec{Q}$, i.e the magnetic Bragg peaks can be detected if the neutron wave vector transfer $\vec{Q}$ has a component perpendicular to the direction of the ordered spins and equals a magnetic reciprocal lattice vector $\vec{\tau_M}$. The magnetic structure factor is given by: by[45, 46]:

$$\vec{F_M}(\vec{Q}) = \sum_{N}^{n=0} f_n^M(\vec{Q})\vec{m}_n exp(i\cdot\vec{Q}\cdot r_n)\cdot W_n \tag{3.37}$$

$f_n^M(Q)$ is the magnetic form factor which describes the density of magnetic moments in an atom. Similarly to the X-ray form factor, the magnetic form factor decreases of at larger Q, while the nuclear scattering length is independent of Q.

3.4. Magnetic structure

3.4.1. Polar and Axial Vectors

Due to their spin, unpaired electrons have a magnetic dipole moment represented as an axial vector perpendicular to a current loop and its direction is given by the right hand thumb rule of electromagnetism. An axial vector is most often presented as the cross product of two polar vectors. The axial vector transform like polar vector under proper rotations, but change sign under improper symmetry operation such as inversion, mirrors and roto-inversions.

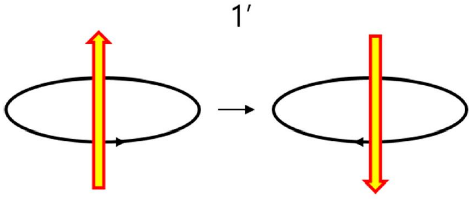

Figure 3.4.: Action of time reversal on a current loop: the axial vector (magnetic dipole) is inverted. Taken from [47]

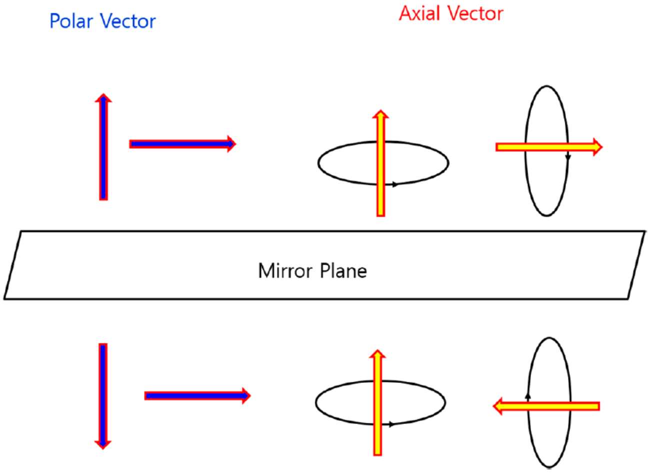

Figure 3.5.: Action of a mirror plane on a polar vector and on an axial vector. Taken from [47]

To describe the direction of the axial vector, a new symmetry operator can be introduced, designated as $1'$. This new operator is called spin reversal operator or time reversal operator. Under this operator, the current loop must change its sign and as a result, it flips the direction of the magnetic moment $1'\vec{m} = -\vec{m}$ (see Figure 3.4).

Unlike the axial vector it is not necessary to consider a loop for a polar vector, therefore, the operation of symmetry on a polar vector is easily understood. The differences between the two vectors under a mirror symmetry operation are indicated in Figure 3.5.

If we combine a symmetry operator g with $1'$, we simply write g'(a primed element). Then, a general operator g acts on the magnetic moment $\vec{m}$ as: $gm = \delta\, det(g) gm$, where δ is the signature of the operator, that is, δ=1 if the operator is unprimed and δ=-1 if the operator is primed.

3.4.1.1. Magnetic space groups: Shubnikov groups

If a magnetic group is denoted as $\mathbf{M}$ and a conventional crystallographic group as $\mathbf{G}$, then $\mathbf{M}$ can be obtained as a subgroup of the outer direct product of $\mathbf{R}$ with the crystallographic group $\mathbf{G}$ ($\mathbf{M} \subset \mathbf{G} \otimes \mathbf{R}$, where $\mathbf{R}$ is defined as the time reversal group that is formed by only two elements $\{1, 1'\}$. The group $\mathbf{G}$ is known as colorless group. The paramagnetic group $\mathbf{P}$ is known as a gray group. It is a simple summation of a crystallographic group and a time reversal operation ($\mathbf{P}= \mathbf{G} + \mathbf{G}1'$). The notation of the resulting group is exactly the conventional Hermann–Mauguin (HM) symbol followed by the symbol $1'$. The colorless groups $\mathbf{G}$ and the gray groups $\mathbf{P}$ are trivial and they both comprise 230 groups [48].

For the magnetic space groups $\mathbf{M}$, the non-trivial black-white groups are important. The $\mathbf{M}$ group can be derived from the crystallographic group $\mathbf{G}$. This relation is expressed as $\mathbf{M} = \mathbf{H} + (\mathbf{G} - \mathbf{H})1'$, where $\mathbf{H}$ is subgroup of index 2 of the parent group $\mathbf{G}$ constituting the unprimed elements, and $\mathbf{G} - \mathbf{H}$ are the elements that are multiplied by the time reversal operator. This is valid for all kind of groups: point groups, translation groups and space groups [48].

The total number of magnetic space groups classified by Shubnikov is 1651 [49]. Among these 1651 magnetic space groups, there are 230 colorless groups $\mathbf{G}$ and 230 gray groups $\mathbf{P}$. In addition, using the relation ($\mathbf{M} = \mathbf{H} + (\mathbf{G} - \mathbf{H})1'$), one obtains 1191 Black–White groups. The Black-White (BW) group can be divided into two types based on whether the translational symmetry changes with respect to the space group $\mathbf{G}$ or not [48]. In the Shubnikov groups of the first kind of Black–White groups (BW1) the subgroup of translations is the same as that of the space group from which they derive ($\mathbf{H} \subset \mathbf{G}$). These groups are *translationengleich* or *t*-subgroups of $\mathbf{G}$. This means that the spin reversal operator is not associated with translations and the magnetic unit cell is the same as the crystallographic cell. The notation of these groups is the same as the Hermann–Mauguin symbol of $\mathbf{G}$, except for the fact that the appropriate generators are primed. There are 674 subgroups that fulfill this equi-translation condition.

In the remaining 517 of the black-white groups, there is a change in the translational symmetry but the crystal class is kept. This corresponds to *klassengleiche* or *k*-subgroups of **G**. In this case, the translation subgroup contains translation that are combined with the time inversion. These groups are called equi-class groups or second Black–White groups (BW2) [48].

To denote a magnetic space group, two notations are used: Opechowski–Guccione (OG) based on the parent crystallographic group **G** and Belov–Neronova–Smirnova (BNS) based on the subgroup **H**. The difference between both notations is in the description of the magnetic lattices of the BW2 groups. In the BNS notation none of the generators constituting the symbol of the group are primed, instead the primed element can be obtained from the magnetic lattice type that is explicitly specified. On the contrary, the OG notation conserves the original HM symbol and uses the primed generators. Note that for BW1 groups, the BNS and OG notations coincide [48, 50].

For BW2 groups in the BNS setting, the magnetic space-group symbol is the crystallographic space-group symbol for **H** with a subscript added to the first letter, denoting the type of colored lattice. As an example, if one considers a primitive Bravais lattice with black lattice points at T_P and one adds a white lattice point to the centre of each unit cell, i.e. T_I=T_P+t_C (where t_C is a vector corresponding to half the body diagonal, one obtains a black and white Bravais lattice P_I [50]. P_I thus denotes that an original body centred lattice becomes primitive, as the centring translations are combined with time inversion and become *anti*-translations. The general expression of the magnetic lattice containing translations and anti-translations is given by [48]:

$$\mathbf{M}_L = \mathbf{H}_L + (\mathbf{T} - \mathbf{H}_L)1', \tag{3.38}$$

where $\mathbf{H}_L$ is a subgroup of index 2 containing pure lattice translations and $(\mathbf{T}-\mathbf{H}_L)1' = \mathbf{H}'_L$ are the remaining operators containing the anti-translation.

3.4.1.2. Formalism of a propagation vector $\vec{k}$

Magnetic structures can be described by the periodic repetition of a magnetic unit cell in the three directions of space, just as nuclear crystal structures are described by lattice translation of a unit cell. In order to describe a magnetic structure one uses a description based on the nuclear unit cell and a 'propagation vector', $\vec{k}$, that describes the relation between moment orientations of equivalent magnetic atoms in different nuclear unit cells. $\vec{k}$ can be determined from the position of the magnetic Bragg reflections seen in neutron diffraction patterns recorded at magnetically ordered phase of a material. In general a magnetic structure is given by its Fourier-components in the form:

$$m_{l,j} = -\sum_{q} m_{k,j} \cdot exp(i \cdot k \cdot R_l), \tag{3.39}$$

where $m_{l,j}$ denotes the moments of atom j in cell in the unit cell having as origin the lattice vector R_l.

3.4.1.3. Example: possible magnetic space groups for $Mn_3Fe_2Si_3$

The space group describing the symmetry of $Mn_3Fe_2Si_3$ is $P6_3mcm$. No structural phase transition was observed in $Mn_3Fe_2Si_3$ at low temperatures, yet in the following it will be described in the orthohexagonal setting corresponding to the $Ccmm$ cell (subgroup of $P6_3mcm$) which was chosen in the literature for the description of the parent compound Mn_5Si_3 [2, 22, 23]. (see Appendix A.1 for further details).

Starting from the space group $Ccmm$ (group **G**) the magnetic space groups can be constructed using the International tables for Crystallography, Volume A (ITA) [51]. For this, one first has to derive all space groups that are subgroups (**H**) of index 2 of **G**. There are three different kinds of maximal non-isomorphic subgroup for $Ccmm$, namely, I, IIa and IIb (empty) [51]. The subgroups in group I correspond to t-subgroups and the ones in group II are k-subgroups. Based on the magnetic space group approach described above, the division I and II correspond to the BW1 and BW2-type, respectively. In the following only the BW2-type groups are derived. In the ITA, IIa composed of eight subgroups **H** of index $k = 2$ are given [51].

H Index 2	Notations of **M** Based on Eq.3.38	BNS[1]	BNS[2]	OG
$Pmma$	$\{1,2_{1x},2_y,2_z,-1,m_x,m_y,a_z\}\mathbf{H}_L + \{1,2_{1x},2_{1y},2_{1z},-1,n_x,c_y,n_z\}\mathbf{H}'_L$	P_Amma	P_Ccmm	C_Pmcm
$Pnna$	$\{1,2_x,2_{1y},2_z,-1,n_x,n_y,a_z\}\mathbf{H}_L + \{1,2_{1x},2_{1y},2_{1z},-1,b_x,m_y,m_z\}\mathbf{H}'_L$	P_Bnna	P_Cnan	$C_Pm'c'm'$
$Pbcm$	$\{1,2_x,2_{1y},2_{1z},-1,b_x,c_y,m_z\}\mathbf{H}_L + \{1,2_{1x},2_y,2_{1z},-1,m_x,n_y,n_z\}\mathbf{H}'_L$	P_Cbcm	P_Ccam	$C_Pm'cm$
$Pnnm$	$\{1,2_{1x},2_{1y},2_z,-1,n_x,n_y,m_z\}\mathbf{H}_L + \{1,2_x,2_{1y},2_{1z},-1,b_x,m_y,a_z\}\mathbf{H}'_L$	P_Bnnm	P_Cnmn	$C_Pmc'm'$
$Pmmn$	$\{1,2_{1x},2_{1y},2_z,-1,m_x,m_y,n_z\}\mathbf{H}_L + \{1,2_x,2_{1y},2_{1z},-1,c_x,n_y,b_z\}\mathbf{H}'_L$	P_Bmmn	P_Cnmm	$C_Pmc'm$
$Pbcn$	$\{1,2_{1x},2_y,2_{1z},-1,b_x,c_y,n_z\}\mathbf{H}_L + \{1,2_x,2_{1y},2_{1z},-1,m_x,n_y,m_z\}\mathbf{H}'_L$	P_Cbcn	P_Ccan	$C_Pm'cm'$
$Pnma$	$\{1,2_{1x},2_{1y},2_{1z},-1,n_x,m_y,a_z\}\mathbf{H}_L + \{1,2_{1x},2_y,2_z,-1,m_x,c_y,n_z\}\mathbf{H}'_L$	P_Anma	P_Ccmn	C_Pmcm'
$Pnma$	$\{1,2_{1x},2_{1y},2_{1z},-1,n_x,m_y,a_z\}\mathbf{H}_L + \{1,2_x,2_{1y},2_z,-1,b_x,n_y,m_z\}\mathbf{H}'_L$	P_Bnma	P_Cnam	$C_Pm'c'm'$

Table 3.1.: Magnetic space groups **M** in the standard setting with respect to BNS and OG notations derived from $Ccmm$ space group of the parent structure using Eq. 3.38. [1] Standard setting, [2] Non-Standard setting.

Table 3.1 shows these eight magnetic space groups **M** in BNS and OG notations derived from the $Ccmm$ space group of the parent structure using Eq. 3.38. For the BNS standard setting, three types of Black-and-white lattice generators (Operations corresponding to a translation) were used to construct the magnetic space groups: $(0,\frac{1}{2},\frac{1}{2})$ for P_A, $(\frac{1}{2},0,\frac{1}{2})$ for P_B and $(\frac{1}{2},\frac{1}{2},0)$ for P_C.

It should be pointed out here that for the refinement the non-standard settings of the magnetic space groups were used in order to keep the origin and unit-cell orientation of the nuclear structure comparable in all models.

4. Experimental methods and instruments

4.1. Synthesis and crystal growth

4.1.1. Cold crucible induction melting

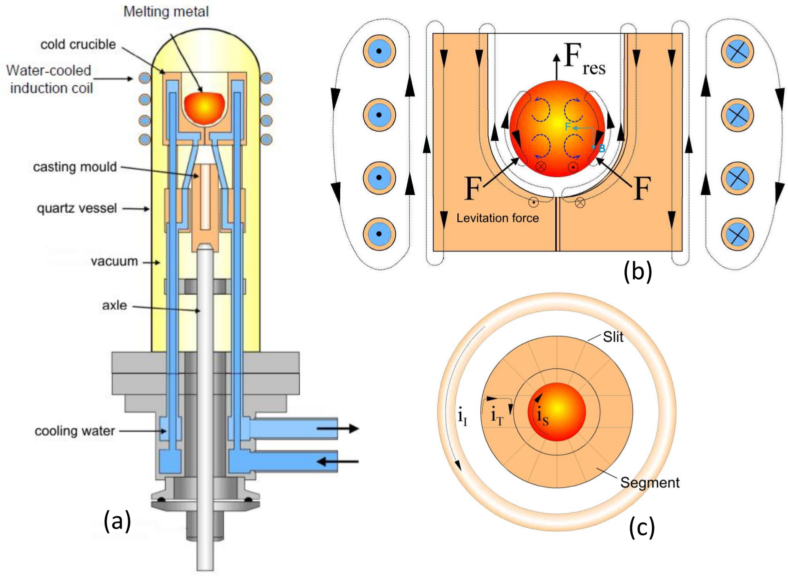

Figure 4.1.: Schematic drawing of an apparatus for cold crucible induction melting taken from [52].

The cold crucible induction melting (CCIM) (see Figure 4.1-a) is a process to melt high temperature reactive materials [53]. The CCIM combines metal melting and levitation, and avoids contact between the molten material and the crucible. The sample is placed in a copper crucible which is divided in several segments. Each segment is insulated from the neighboring segments, and cooled with water. An electric field is generated from high frequency alternating current (AC) which passes through multi-turn induction coils that surround the glass tube covering the crucible. The induced current I_T looped around each segment generates an induced current I_S in the sample, resulting in the required magnetic field in the metallic sample (see Figure 4.1-c). An increase in power causes eddy currents that produce joule heating which melts the sample in a sphere-like shape. The molten metal is levitated by Lorentz forces, which minimize the thermal losses and accelerate the process of heating (see Figure 4.1-b). Additional forces F are generated from the interaction between the induced currents and the magnetic field and result in further movements of the melt. Hence, through the constant and well controlled stirring, a melt of high homogeneity and purity grades can be produced.

4.1.2. Single crystal growth (Czochralski method)

The single crystals investigated in the course of this thesis were grown by the Czochralski method [54], a technique widely used for growing large-size single crystals. Figure 4.2 presents the basic setup of the Czochralski process. A crucible of suitable size is put on a holder surrounded by Copper coils. A generator supplies a large alternating current which passes through the coils to heat the starting material which is placed in the crucible. The solid is inductively heated due to its electrical conductivity. A suitable seed crystal is then mounted on a rod and dipped into the surface of the melt. When crystal growth begins, the rod with the seed crystal is rotated and slowly drawn from the melt. The diameter of the pulled crystal is controlled by manipulating the temperature of the melt and the pulling rate.

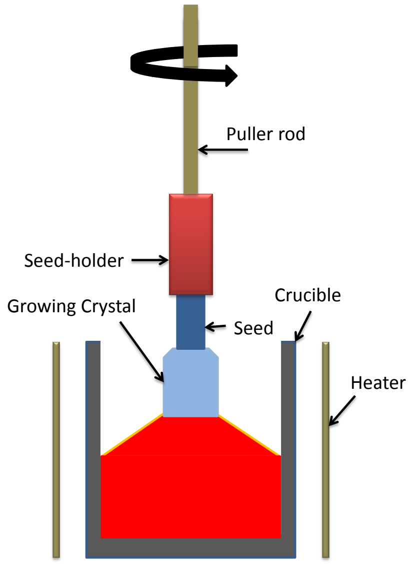

Figure 4.2.: Illustration of the setup used for the growth of single crystals with the Czochralski method

4.2. Measurement of physical properties

The magnetic and thermal property measurements described in this thesis were performed using the commercial Physical Property Measurement System (PPMS) from Quantum Design. The system provides magnetic field up to ± 9 Tesla and temperatures in the range of 1.9 - 400 K, which can be extended depending on the used measurement option from 0.05 K to 1000K.

4.2.1. Vibrating sample magnetometer (VSM)

A Vibrating Sample Magnetometer (VSM) is one of the measurement options of the PPMS to determine the magnetic moment of a sample, magnetization, isothermal remanent magnetization as well as demagnetization curves. The sample is placed between sensing coils and is mechanically vibrated (sinusoidal motion) by the VSM linear motor transport (head). The sample must be precisely positioned in the center of the gradiometer pickup coil. The precise position and amplitude of oscillation are controlled by the VSM motor module.

According to Faraday's Law of electromagnetic induction, the resulting magnetic flux changes induce a voltage in the sensing coils that is proportional to the magnetic moment of the sample. The induced voltage is amplified and detected in the VSM detection module. The VSM detection module uses the position encoder signal as a reference for synchronous detection. In order to reach a sensitivity to magnetization changes less than 10^{-6} emu at a data rate of 1 Hz, an oscillation amplitude with a peak of 1-3 mm, and a frequency of 40 Hz is usually applied.

4.2.2. Heat Capacity

The Physical Property Measurement System (PPMS) employs the relaxation calorimetry method for the specific heat measurements by controlling the heat added to and removed from a sample while monitoring the resulting change in temperature. In the calorimeter, a heater and a thermometer are attached to the bottom side of the platform suspended by eight wires in the center of the puck (See Figure 4.3). The wires provide a thermal connection to the platform and an electrical connection to the thermometer and the heater. The sample is attached and thermally coupled to the platform by using a thin layer of grease [55].

During the measurement, a known amount of heat is applied for a fixed time and then followed by a cooling period of the same duration. The relaxation process is recorded and the value of the specific heat of the sample can then be obtained from the fit of the data. Because both the platform and the grease will contribute to this relaxation time, it is crucial to take an addenda measurement at the beginning, where the heat capacity of the puck with grease is measured separately. Afterwards, the heat capacity of the sample is calculated by subtracting the calculated addenda contribution from the total heat capacity measurements at each temperature [55].

To fit the temperature response curve, the software uses two thermal models, the 'simple' model and the two tau model, depending on the thermal link between the sample and the platform.

The simple model assumes that the sample and platform have a good thermal coupling between each other and are at the same temperature during the measurement; generally this model is used to measure the addenda. However, when the thermal coupling between the sample and platform is poor (grease between sample and platform), the software uses the two-tau model to measure the heat capacity. The following equations express the two-tau model:

$$C_p \frac{dT_p}{dt} = P(t) - K_1(T_p(t) - T_b) + K_2(T_s(t) - T_p(t)) \tag{4.1}$$

$$C_s \frac{dT_s}{dt} = -K_2(T_s(t) - T_p(t)) \tag{4.2}$$

where a C_p, C_s are the heat capacity of the platform and sample, receptively; K_1 is the thermal conductance of the supporting wires; K_2 is the thermal conductance between the sample and platform due to the grease; T_p and T_s are the respective temperatures of the platform and sample; and $P(t)$ is the power applied by the heater. In the two-tau model, the first time-constant (tau 1) represents the relaxation time between the sample platform and the puck, and the second time constant (tau 2) represents the relaxation time between the sample platform and the sample itself. A detailed description of this model can be found in [56].

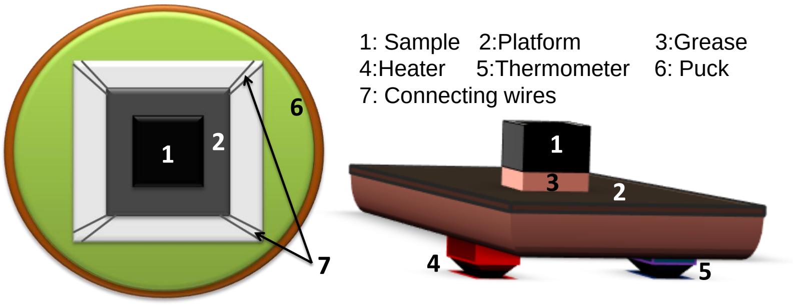

Figure 4.3.: Scheme of a PPMS puck for heat capacity measurements.

4.3. Scattering techniques: instrumentation

4.3.1. X-ray Diffraction: Laue camera

The back-reflection Laue method [57] was used to determine the orientation of large single crystals in the course of this thesis. An incident white X-radiation beam strikes the crystal and is then diffracted by the crystal planes into a spot pattern according to Bragg's law. The Laue apparatus used here to orient the crystals is the MWL120 real-time back-reflection Laue camera system, equipped with a multiwire detector and a tungsten X-ray tube. In the MWL120 system, the crystal is mounted on a holder fixed on a three-axis motorized rotation goniometer With the help of the camera, the orientation process can be observed in real time [58].

4.3.2. X-ray diffraction: 4-circle Huber single crystal diffractometer (P24-Beamline, DESY)

The 4-circle Huber single crystal diffractometer with Eulerian cradle is installed in the second experimental hutch (EH2) of the P24 beamline. And it is equipped with marCCD165 detector at the high brilliance PETRA III storage ring at DESY (Hamburg, Germany) [59]. The experimental hutch is located at 84 m from the undulator. The energy of the beam can be tuned within a range between 2.4 keV and 44 keV with the help of two crystal pairs, Si(111) and Si(311) which form the double crystal monochromators [59]. The scheme of the 4-circle diffractometer with Eulerian geometry is shown in Figure 4.4. The crystal can be rotated around three axis (ω, ϕ, χ) and the detector is moved around a fourth axis (2θ).

The goniometer is mounted on an ω-circle, lying in the horizontal plane, and so having a vertical rotation axis. Perpendicular to ω-circle is the vertical χ-circle, having a horizontal axis, whatever the value of ω. The goniometer head on which the crystal is attached, is mounted on the ϕ-circle, located on the inside of χ [37].

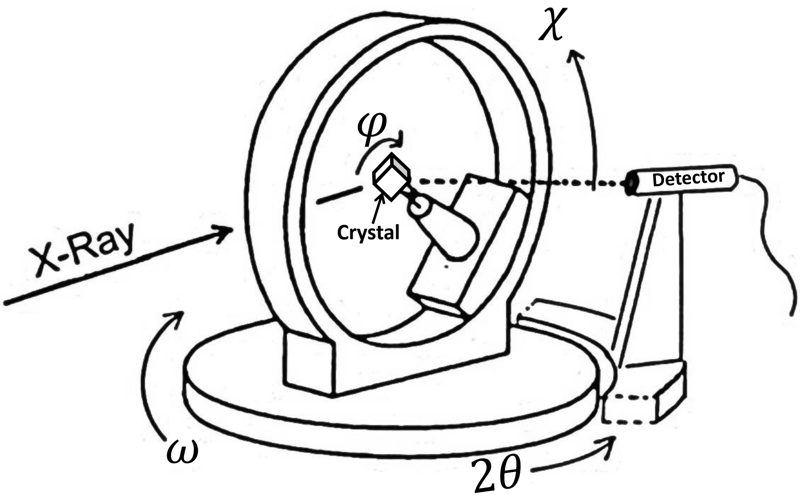

Figure 4.4.: Scheme of the 4-circle Eulerian geometry taken from [37]

4.3.3. Neutron Diffraction: Double-axis diffractometer (E4-Beamline, Berlin)

The double-axis E-4 diffractometer is operated by the Helmholtz-Zentrum Berlin at BER II research reactor [60]. It provides sample environments covering magnetic fields up to 17 T and temperatures down to 30 mK. The monochromator shielding contains one beam channel at a take-off angle $2\theta_M = 42.5°$. This position corresponds to the incident wavelength of 0.24 nm for the vertical focusing PG(002) monochromator. A radial collimator is oscillated several degrees about the sample position,so that any shadowing of the detectors is uniformly distributed. This collimator is placed between the monochromator and the primary shutter. The instrument is equipped with a position sensitive 200x200 mm^2 detector (PSD) (see Figure 4.5) [60].

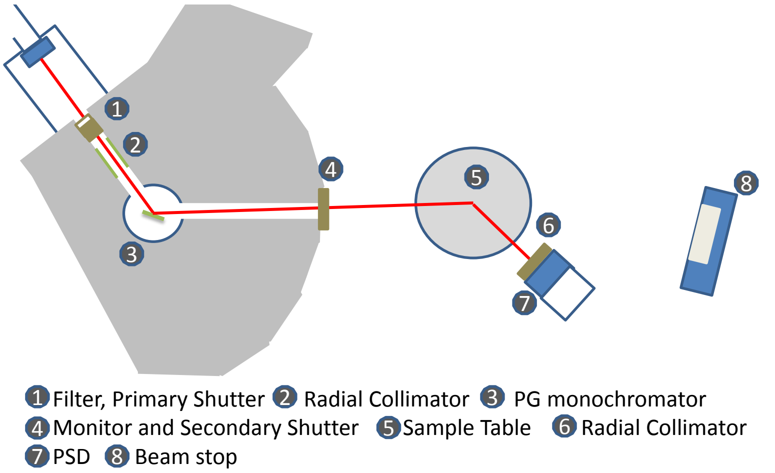

Figure 4.5.: Schematic view of the 2-axis E4 diffractometer taken from [60].

4.3.4. Neutron scattering: Time-of-flight spectroscopy (Merlin)

The MERLIN time of flight (TOF) spectrometer (Figure 4.6) is installed at target station 1 of the ISIS Pulsed Neutron and Muon Source (STFC Rutherford Appleton Laboratory, U.K.). This instrument is a direct geometry spectrometer, i.e. the energy of the incoming neutrons is fixed, and the energy of the scattered neutrons is measured by time-of-flight analysis. Thanks to the large area position sensitive detector MERLIN resolves the momentum and the energy transfer with good resolution MERLIN provides a large incident flux compared to other INS spectrometers thanks to the supermirror guide. [61]. The energy of the incident neutrons can be chosen in a wide range, from 10 to 1000 meV, with an energy resolution of the order of $3-5\%$ [61].

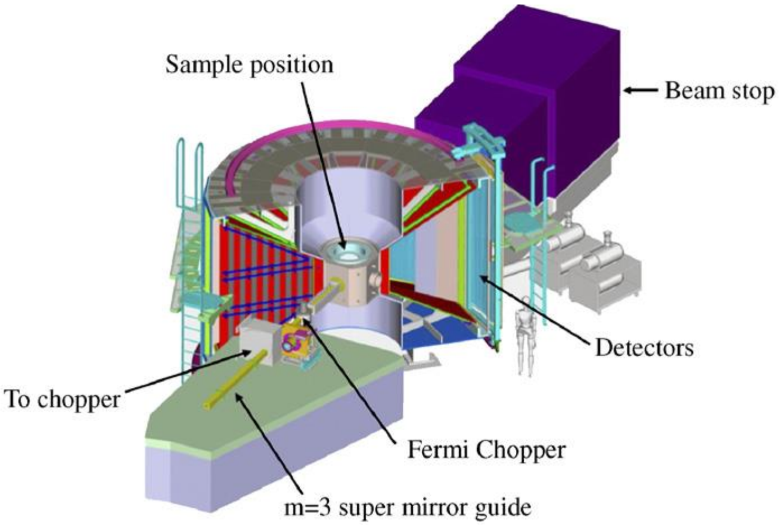

Figure 4.6.: Schematic view of the MERLIN spectrometer at ISIS taken from [61].

4.3.5. Neutron diffraction: Time-of-flight diffraction (POWGEN)

POWGEN is a third-generation time of flight powder diffractometer (see Figure 4.7) constructed at the Spallation Neutron Source (SNS), Oak Ridge National Laboratory. The source to sample distance of 60 m and the source frequency of 60 Hz provide a bandwidth $\Delta\lambda$=1 Å, that can be centered around $\lambda_0 = 0.8, 1.5, 2.67, 4.8$ Å to cover a lattice d-spacing range 0.1 Å< d < 38 Å. The detector covers an angular range $10° < 2\theta < 170°$. It covers d-spacings from ~ 0.1 Å, or less, to 8 Å in a single measurement. The particular geometric design of POWGEN and the flight path from moderator and sample yields a high count rate while preserving a high resolution of Δd/d = 0.0015 at a d = 1 Å[62].

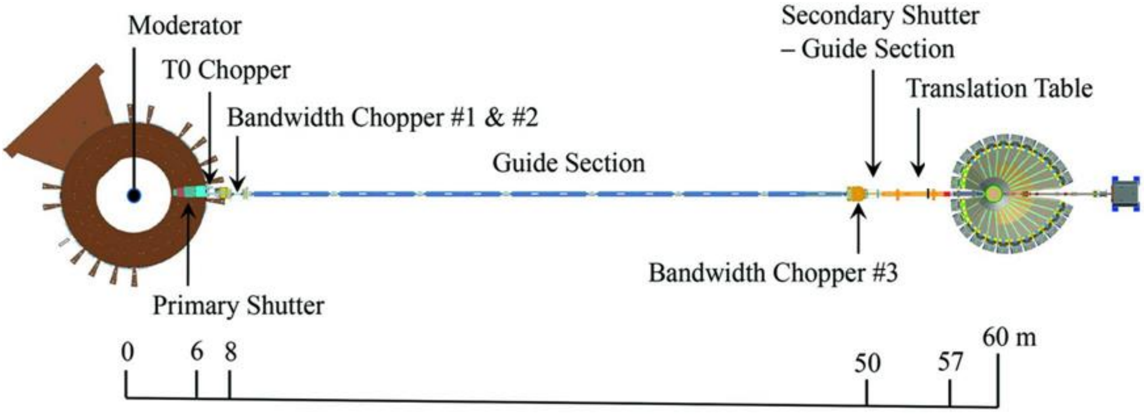

Figure 4.7.: Schematic top view of POWGEN taken from [63]

5. Experimental process

5.1. Synthesis of $Mn_3Fe_2Si_3$ single crystal

Polycrystalline samples of $Mn_3Fe_2Si_3$ were prepared by the cold crucible induction melting process under argon atmosphere. First, the pure constituent elements, manganese Sigma Aldrich, 99,9%, iron Sigma Aldrich, 99,9% and silicon Chempur, 99,9% were weighed according to the respective stoichiometric ratio in the compound (see table 5.1). The sample was placed in a copper crucible using cleaned tweezers in order to prevent any possible contamination.

The big pieces of the raw materials were placed at the bottom of the crucible to avoid the fall out of the smaller pieces from the slits of the crucible. All raw materials were heated under vacuum (10^{-6} mbar) to prevent oxidation of the ingots. Afterwards, the sample chamber was filled with 800 mbar of argon. And finally, the raw materials were melted with high frequency alternating magnetic fields and quenched to room temperature. Once the molten sample has cooled we turned it around and melted it again for two times in order to improve its homogeneity. This synthesis has been performed two times and two pellets of the polycrystalline materials were obtained and weighed approximately 50 g each. They were brushed and cleaned with ethanol and set to an ultrasonic bath to remove impurities. The obtained polycrystalline materials were then used as starting materials for the growth of a large single crystal of $Mn_3Fe_2Si_3$ by the Czochralski method (see section 4.1.2). The pellets were filled into an aluminum oxide crucible, which was also cleaned with ethanol. The aluminum oxide crucible was put into a larger ceramic crucible and then put at the center of the furnace to ensure that the heat was evenly distributed. After melting the material in argon atmosphere, the single crystal growth was started using a seed crystal of tungsten with rotation speed of 20 rev/min mounted on a rod which moved with a pulling rate of 10 mm/h. The obtained crystal of $Mn_3Fe_2Si_3$ is shown in figure 5.1. The phase purity of the grown single crystal was checked by laboratory X-ray powder diffraction on a ground piece of the single crystal. The chemical composition of the prepared samples was confirmed with Inductively Coupled Plasma with Optical Emission Spectroscopy (ICP-OES) (see table 5.1)

Substance	Real Mass (g)	Mass ratio (%)	ICP OES results	Producer
Mn	22.847	45.69	45.6±0.3	Aldrich
Fe	15.48	30.96	29.3±0.2	Aldrich
Si	11.68	23.36	23.41±0.14	Chempur

Table 5.1.: Stoichiometric ratio and Mass of $Mn_3Fe_2Si_3$ substances and their mean concentration with standard deviation obtained by (ICP-OES) Spectroscopy

Figure 5.1.: Photo of the final crystal. The long axis correspond to a crystallographic c-axis.

5.2. Macroscopic measurements

5.2.1. Magnetization measurements

Measurements of the temperature and magnetic field dependent magnetization parallel and perpendicular to the hexagonal [001]-direction, were carried out in the temperature region between 5 K and 380 K and magnetic fields in the range -9 T $\leq \mu_0 H \leq$ 9 T using the vibrating sample magnetometer (VSM) option in a PPMS from Quantum Design. The crystallographic orientation of the two fragments of the single crystals specimen were first determined using x-ray Laue diffraction and then the fragments were cut using spark erosion. The weights of these two single crystals were 11.2 mg and 17 mg for measurements with field perpendicular to [001] and parallel to [001], respectively.

The datasets for all isofield magnetization experiments for both directions were measured upon cooling in sweep mode at a temperature change rate of 2 K/min yielding approximate temperature steps of 0.35 K, i.e. the temperature is varied continuously while recording the magnetization with an integration time of 1s.

Isothermal magnetization measurements were performed by applying the sweep mode for the field variation. For strong fields ($|\mu_0 H| > 0.1$ T), a change rate of 19.8 mT/s was used. However, because sweep mode does not attempt to stabilize the field at the intermediate set points, it may not produce highly accurate data. So, to measure the steeper changes of the magnetization, the field change rate was reduced to 5 mT/s ($|\mu_0 H| < 0.1$ T).

Table 5.2 summarizes the isothermal magnetization measurements protocol. Furthermore, isothermal magnetization loops were also recorded in the field scan range $\mu_0 H$ = ±8.5T at 10 K, 50 K, 100 K, 150 K and 300 K.

Temperature region (K)	ΔT (K)
5-45	5
45-75	2
75-105	5
105-130	2
130-351	10

Table 5.2.: Temperature protocol of isothermal magnetization measurements

5.2.2. Heat capacity measurements

Heat capacity HC measurements on a $Mn_3Fe_2Si_3$ single crystal were carried out at different magnetic fields up to $\mu_0 H$=6 T parallel and perpendicular to [001], between 10-150 K using a PPMS DynaCool from Quantum Design. For the addenda measurement, a tiny amount of Apiezon-N-grease was added on the sample platform of the puck and measurements were performed at zero magnetic field between 1- 150 K with 35 points. All HC measurements were perfomed on the fragment with mass 11.2 mg used in the magnetization measurements. The sample was placed in the center of the puck and carefully fixed in the grease. The table 5.3 summarizes the number of points measured at all temperature ranges. Both, the addenda and sample measurements, were performed with a linear temperature increase and a heating rate of 2%. A polynomial interpolation between two neighboring data points was applied using the automatic procedure implemented in the PPMS software, in order to subtract the addenda heat capacity from the sample heat capacity at each temperature.

Temperature region (K)	Number of points
10-40	15
40-75	70
75-116	20
116-126	20
126-151	12

Table 5.3.: Number of points in the heat capacity measurements at all temperature ranges

5.3. Neutron powder diffraction

Temperature-dependent neutron powder diffraction data of $Mn_3Fe_2Si_3$ were recorded using time-of-flight (TOF) neutron diffraction at the POWGEN diffractometer at 20, 50, 90, 105, 150, 200 and 300 K. About 5 g of well ground $Mn_3Fe_2Si_3$ powder sample was loaded into a vanadium can with 8 mm diameter under He atmosphere to ensure proper thermalisation of the powder. The container was sealed and then placed in the carousal inside the sample changer. The data was recorded using two different bands, one with central wavelength CWL= 0.8 Å and the other with CWL = 2.665 Å. The two CWL lead to two d-spacing coverage 0.1340-8.200 Å and 1.0701-22.9342 Å, which is required to measure both small d-spacing reflections, providing information about the nuclear structure, and large d-spacing reflections originating from the AF magnetic structure.

5.4. X-ray single crystal diffraction

For all measurements at the P24 beamline the wavelength of synchrotron radiation was tuned to $\lambda = 0.44279$ Å. In the beginning, a standard corundum crystal with well known lattice parameter was measured. From these data the geometrical center of the detector (x_0, y_0) and its distance (d) from the sample were deduced.

Crystals of $Mn_3Fe_2Si_3$ up to 100 μm in length were attached using a small amount of two-component glue to the top of glass fibers and mounted on the goniometer. The quality of the crystals was checked prior to the synchrotron measurements on a laboratory diffractometer. The measurements were carried out by ϕ scans and ω scans at different values of χ with the marCCD165 detector positioned at two different 2θ angles. The temperature-dependent measurements were performed using an open flow Helium cryostat.

Run	2θ	χ	ω	$\phi_i \rightarrow \phi_f, \Delta\phi$	ϕ	$\omega_i \rightarrow \omega_f, \Delta\omega$	t (s)	T
1	30	-70	0	0→180,1			1	(A)
2	0	-70	0	0→180,1			2	(A)
3	0	-40	0	20→200,1			2	(A & B)
4	0	-40			0	-20→30,1	2	(A & B)
5	0	-40			120	-20→30,1	2	(A & B)
6	0	-40			240	-20→30,1	2	(A & B)

Table 5.4.: Run lists of all measured data sets at temperatures A: Upon cooling (300, 250, 200, 150, 125, 100, 80, 60) K ; Upon heating (55, 90) K and B: Upon cooling (40, 20) K; Upon heating (30, 50, 110, 125) K.

Table 5.4 summarizes the run lists of all measured data sets at temperatures A: Upon cooling (300, 250, 200, 150, 125, 100, 80, 60) K ; Upon heating (55, 90) K and B: Upon cooling (40, 20) K; Upon heating (30, 50, 110, 125) K. During cooling at temperatures below 50 K, diffraction from ice was observed in the first and second run. Therefore, these two runs were excluded for the corresponding measurements (designated B in Table 5.4). Figure 5.2 shows a representative diffraction image of the first run at 300 K and 40 K where the ice start to form.

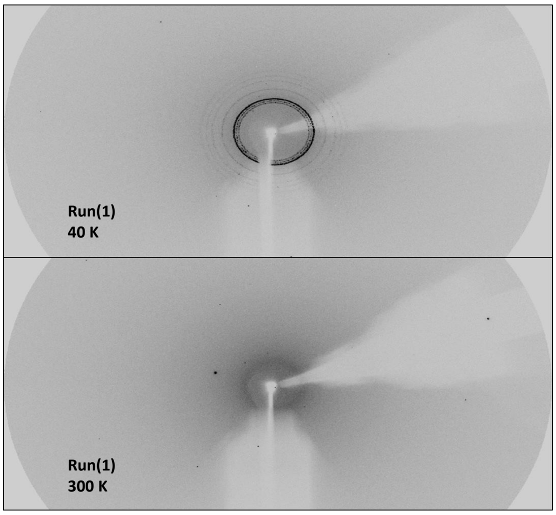

Figure 5.2.: Representative diffraction image of the first run at 300 K and 40 K where the ice start to form.

5.5. Neutron single crystal scattering

5.5.1. MERLIN-Beamline

The neutron scattering of $Mn_3Fe_2Si_3$ single-crystal of mass m = 790 mg was measured on the MERLIN TOF spectrometer, at temperatures T= 5 K and 125 K using incident energies of 9 meV, 13 meV, 21 meV, 40 meV and 108 meV. The single crystal was prealigned by x-ray Laue diffraction.

For the Merlin experiment the crystal was mounted with (0kl) reflections in the horizontal scattering plane and cooled in a closed cycle cryostat to a base temperature of 5 K. The crystal was rotated around the vertical axis in discrete steps of $\Delta\phi = 2°$ covering an angular range of 90°, covering a large volume in reciprocal space. The Fermi chopper was spun at a frequency of 350 Hz. The intensity normalization and the detector calibration were performed by measuring the scattering from a standard vanadium sample with the incident beam. The four-dimensional $S(\vec{Q},\omega)$ was combined and analyzed using the software package Horace [64].

5.5.2. E4-Beamline

The temperature-dependent evolution of the intensities of two magnetic reflections (1 0.5 1) and (1.5 1 0) indices refer to the hexagonal cell ($a \approx 6.85$ Å and $c \approx 4.75$ Å) were measured on the double-axis diffractometer E4 at a neutron wavelength of λ= 2.451 Å with a vertically focusing pyrolytic graphite (PG) monochromator. The corresponding single crystal had a mass of m=150 mg. The single crystal was oriented at room temperature having (0kl) reflections in the horizontal scattering plane. The orientation matrix was determined with five nuclear Bragg reflections found after large-range scans at room temperature and checked again when the crystal was cooled down to 150 K. The sample was cooled to 90 K and then to 20 K, to identify the magnetic Bragg reflections, and finally heated to measure the temperature dependence of reflections at different temperatures. An existing calibration file was used to account for the detector sensitivity.

6. Macroscopic properties of the magnetocaloric compound $Mn_3Fe_2Si_3$

6.1. Heat Capacity (HC)

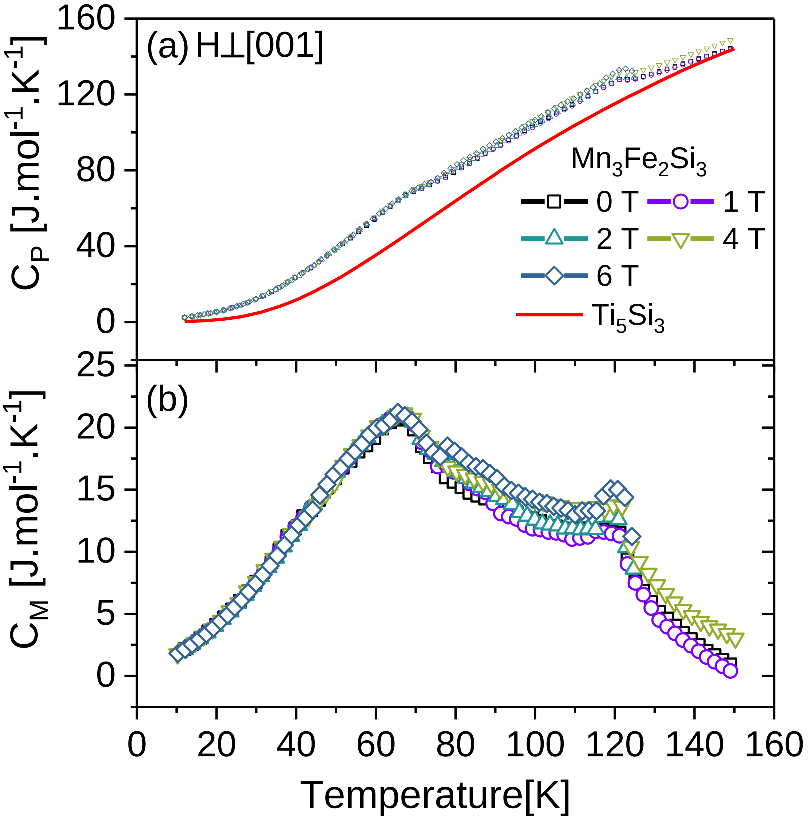

Figure 6.1.: Temperature dependence of (a) total and (b) magnetic heat capacity of $Mn_3Fe_2Si_3$ at different fields with $\vec{H} \perp [001]$ up to 150 K (HC at 6 T was measured only in the temperature range centred around the first anomaly). The red curve in (a) is the total heat capacity of the nonmagnetic compound Ti_5Si_3.

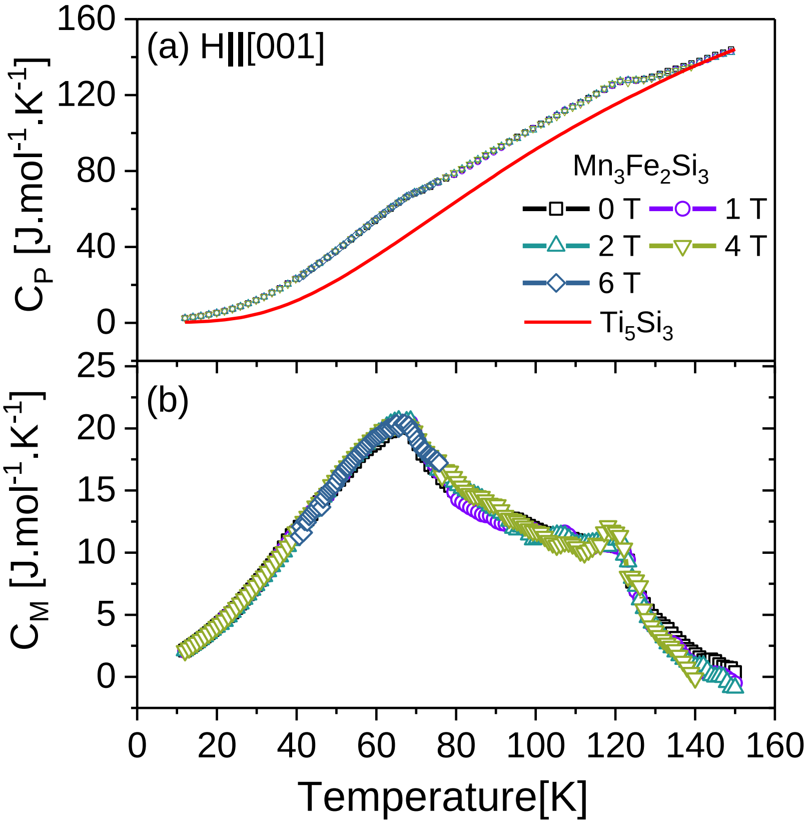

Figure 6.2.: Temperature dependence of (a) total and (b) magnetic heat capacity of $Mn_3Fe_2Si_3$ at different fields with $\vec{H}||[001]$ up to 150 K (HC at 6 T was measured only up 122 K). The red curve in (a) is the total heat capacity of the nonmagnetic compound Ti_5Si_3.

Figure 6.1.a and 6.2.a, show heat capacity results of $Mn_3Fe_2Si_3$ single crystal measured at different fields up to 6 T with $\vec{H}\perp[001]$ and $\vec{H}||[001]$, respectively, together with Ti_5Si_3 for temperatures of up to 150 K, which was scaled according to eq. A.22. As explained in section A.1.5.2 the magnetic contribution to the specific heat capacity of $Mn_3Fe_2Si_3$ is estimated by subtracting the lattice contribution from the molar mass scaled heat capacity of the nonmagnetic isostructural reference compound Ti_5Si_3 which varies monotonically, with no anomaly observed down to 2 K.

Figure 6.1.b and 6.2.b, show the magnetic contribution C_M to specific heat of $Mn_3Fe_2Si_3$ for $\vec{H}\perp[001]$ and $\vec{H}||[001]$, respectively. The magnetic contribution to the specific heat of $Mn_3Fe_2Si_3$ shows two maxima centred around ~120 K and ~69 K, indicating the antiferromagnetic phase transition temperatures as have been observed earlier [4]. The magnetic part of the specific heat changes hardly upon application of the magnetic field. A slight deviation is observed at 6 T, when the field is ⊥ [001], both at the anomaly at 120 K and for the temperature above. It has to be noted, that this measurement was measured with a different addenda, which might also contribute to this result.

The magnetic heat capacity contribution results show no evidence for a field-induced magnetic transition which is in agreement with pulsed field measurements up to 38 T reported by Songlin *et al.* [4]. Furthermore both anomalies in the specific heat don't move upon application of the field. This behavior is distinctly different from Mn_5Si_3. In this compound the AF1-AF2 transition shifts towards lower temperature (see Figure A.19 in appendix) [65].

6.2. Isofield Magnetization

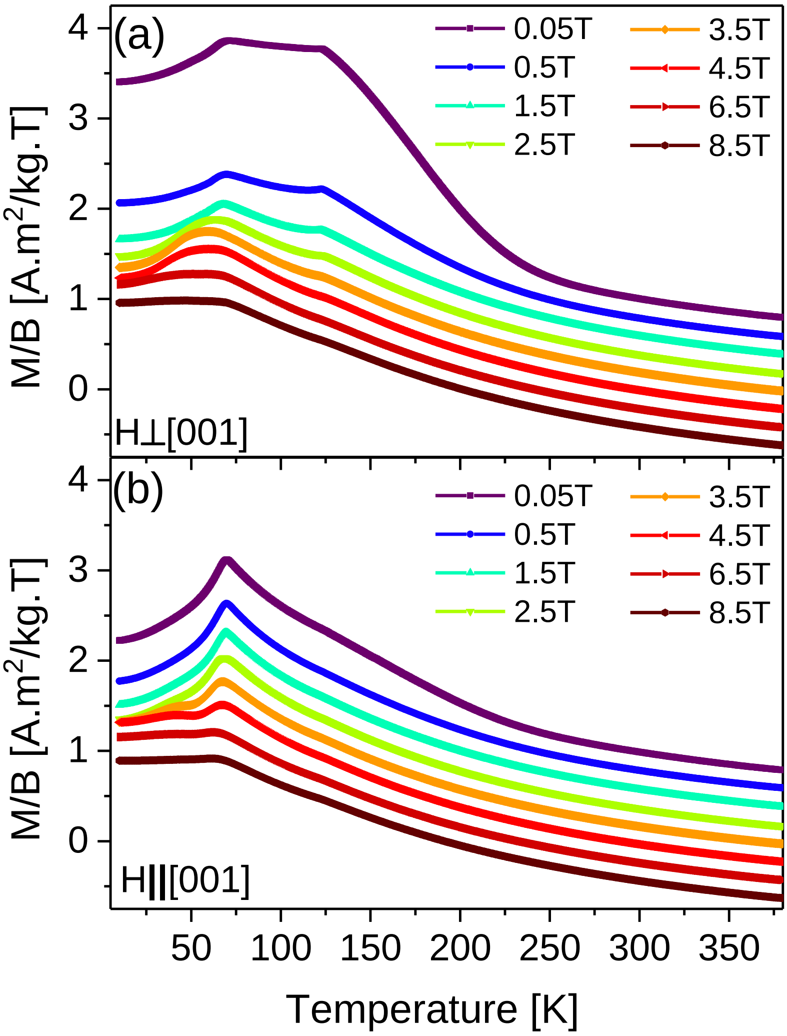

Figure 6.3.: Isofield M/B for different applied field perpendicular to [001] (a) and parallel [001] (b) measured in field cooling conditions. Except for curve at 0.05 T, all curves were shifted down vertically by 0.2 $Am^2kg^{-1}T^{-1}$ for clarity.

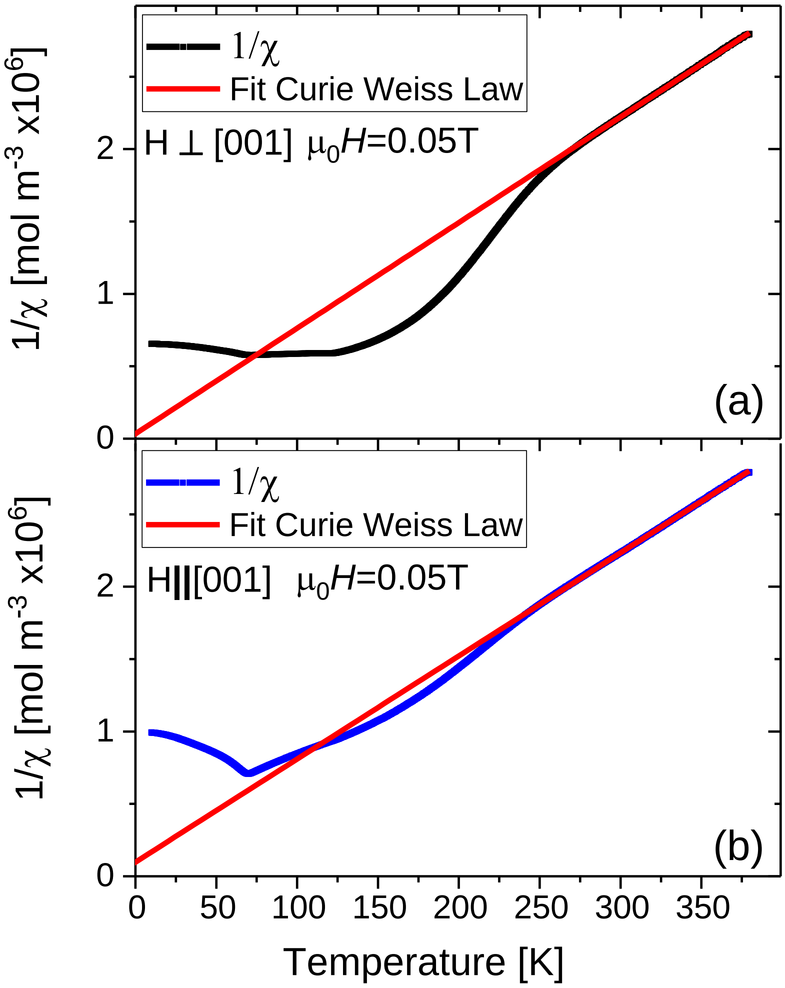

Figure 6.4.: Inverse magnetic molar susceptibility as a function of temperature for applied field (a) perpendicular to [001] and (b) parallel [001]. The red line is a fit to the Curie-Weiss law.

Figure 6.3 presents a summary of isofield magnetization divided by field $\frac{M}{B}$ as a function of temperature T measured on a single crystal sample at different constant fields B with the field applied ⊥ [001] (top) and ∥ [001] (bottom). Except for $\frac{M}{B}$ curve at 0.05 T, all curves at the other fields were shifted down vertically 0.2 $\mathrm{Am^2kg^{-1}T^{-1}}$ for clarity. Apparently the magnetic response is linear in the applied field for temperatures $T > 270K$, indicating the temperature region where the Curie-Weiss analysis is valid.

Figure 6.4 shows $\chi^{-1}_{\mathrm{mol}}(T)$ of $Mn_3Fe_2Si_3$ at μ_0H=0.05 T, with field parallel and perpendicular to [001]. The Curie-Weiss constant was extracted by fitting the high temperature linear region of the inverse magnetic susceptibility (1/χ vs. T plot) using Eq.3.5 and extrapolating the fitted straight line to the x-axis. The intercept value determines the curie-Weiss temperature θ_{CW}.

Multiple temperature ranges have been chosen for the Curie-Weiss analysis in order to have a proper estimate for the uncertainty of the refined mean field parameters. Thus in the fitting, the lower temperature limit has been varied between 280-330 K while keeping the higher temperature limit always at 380 K. The Curie-Weiss temperature and μ_{eff} are slightly different for the different directions and they show small variations with the change in temperature range fitting (280-330 K). The Curie-Weiss temperature is then estimated to be $\theta^{||}_{CW}$=-14 (1) K for $\vec{H}$ parallel to [001] and $\theta^{\perp}_{CW}$=-4.7 (5) K for $\vec{H}$ perpendicular to [001] (The variation of the fitted parameters are indicated within the parenthesis). This difference in the field directions was also observed in the Curie-Weiss analysis performed at each magnetic field with a slight fluctuation in the Curie-Weiss temperatures.

The effective paramagnetic moments per metal atom obtained from the Curie constant C, are $\mu^{||}_{\text{eff}} \simeq 4.23(1)\,\mu_B$ for $\vec{H}$ parallel to [001] and $\mu^{\perp}_{\text{eff}} \simeq 4.18(1)\,\mu_B$ for $\vec{H}$ perpendicular to [001]. The average value of μ_{eff} obtained in this work differs from the μ_{eff} reported by Herlitschke *et al.* for powder data of the $Mn_3Fe_2Si_3$ compound [66], but has a value larger than $\approx 4.1\mu_B$ similar to the other compounds reported by the same author [66]. According to the mean-field approximation discussed in chapter 3.1, the calculated effective paramagnetic moment μ^{cal}_{eff} of $Mn_3Fe_2Si_3$ compound incorporated with Mn^{2+} and Fe^{3+} ions can be described as $\mu^{cal}_{\text{eff}} = \sqrt{(\mu_{\text{Mn}^{2+}})^2 + (\mu_{\text{Fe}^{3+}})^2}$. The observed effective paramagnetic moments per metal atom is smaller than the theoretically expected 5.9 μ_B.

The Curie-Weiss temperatures for both directions are significantly lower than T_N ($\theta^{||}_{CW}, \theta^{\perp}_{CW} \ll T_N$), with $\frac{T_N}{\theta^{||}_{CW}} \approx -5$ and $\frac{T_N}{\theta^{\perp}_{CW}} \approx -14.9$. If we consider the molecular field theory in a simple two-sublattice picture of antiferromagnetism, we can assume λ as the nearest neighbor exchange coupling (inter-sublattice interactions) and Γ as the next nearest neighbor (intra-sublattice interactions), we obtain $\frac{T_N}{\theta_{CW}} = -\frac{|\lambda|-\Gamma}{|\lambda|+\Gamma}$ (see chapter 3). This would suggest that $\frac{|\lambda|}{\Gamma}$ is $\approx$ -1.5 for $\vec{H}$ parallel to [001] and $\approx$ -1.14 for field for $\vec{H}$ perpendicular to [001]. $|\lambda|$ and Γ have opposite sign, so, since $|\lambda|$ presents AFM inter-sublattice interaction this suggest that Γ presents the FM intra-sublattice interaction. In both field directions, $|\lambda| > |\Gamma|$, therefore, the dominant interactions in $Mn_3Fe_2Si_3$ are antiferromagnetic. Below~270 K, $\frac{1}{\chi}$ starts to deviate from the Curie–Weiss fit (Figure 6.4).

In the temperature range between 120 K and 270 K, $\frac{M}{B}$ has an increased response and a concave shape for small applied field $\mu_0 H < 0.5$ T, indicating the existence of some ferromagnetic correlations (Figure 6.3). This effect is seen more strongly for the field applied perpendicular to the [001] direction.

For the low field measurements with $\vec{H}$ perpendicular to the [001]-direction, two strong features are observed at $T_{N2} \approx$121 K and $T_{N1} \approx$72 K. If we evaluate the numerical derivative of the data (see Appendix A.1) we can see also a feature at $\approx$ 121 K for the field applied parallel [001], which is hardly visible in the magnetization data directly. This feature hardly varies with temperature in the entire field range.

The feature at ~72 K, which is local maxima of $\frac{M}{B}$ for small fields, becomes less pronounced with increasing field (Figure 6.3). Figure 6.5 and 6.6 show the temperature derivatives from 70 K to 140 K and from 10 K to 90 K for the different field directions to clarify the changes attributed with the different magnetic phases. They exhibit also distinct features for higher applied fields. The sign change of the temperature derivative shifts to lower temperature with increasing magnetic field (Inset of Figure 6.6 a and b).

For large fields, the magnetization measurements exhibit a complex behavior as seen by the small slope in the temperature region from 45 K to 60 K (Figure 6.3. If the field is applied in [001] direction, the magnetic response (identified by the maximum of the temperature derivative) exhibits a smaller variation, and the zero point of the derivative is well defined for the entire field range (Figure 6.6).

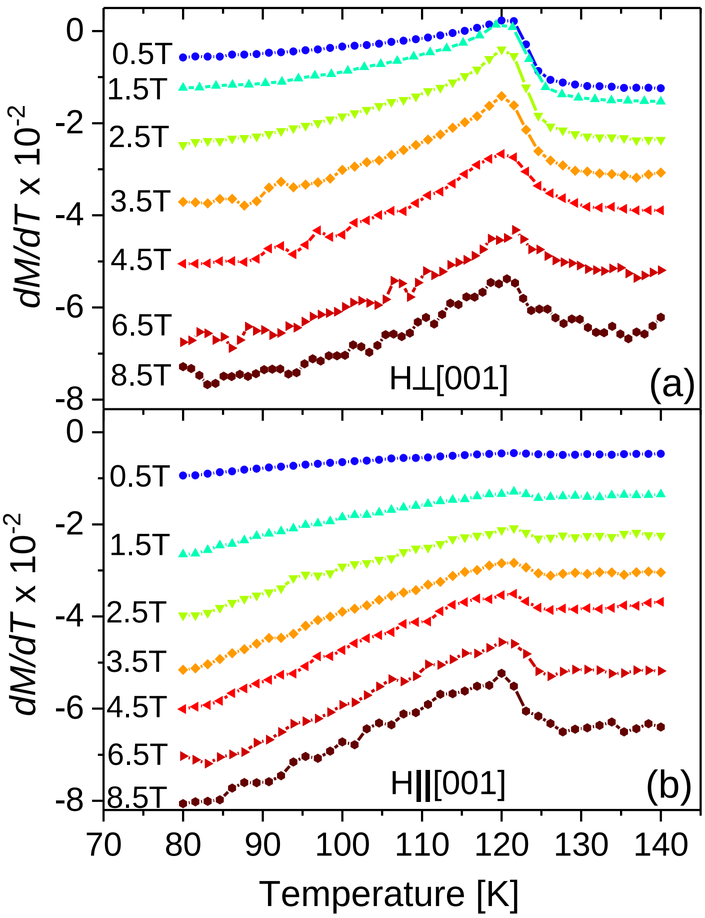

Figure 6.5.: dM/dT curves of $Mn_3Fe_2Si_3$ at different fields, with (a) $\vec{H}\perp[001]$ and (b) $\vec{H}||[001]$. The numerical calculation of the derivative, the measured data has been rebinned to a temperature grid with step-size ~1 K.

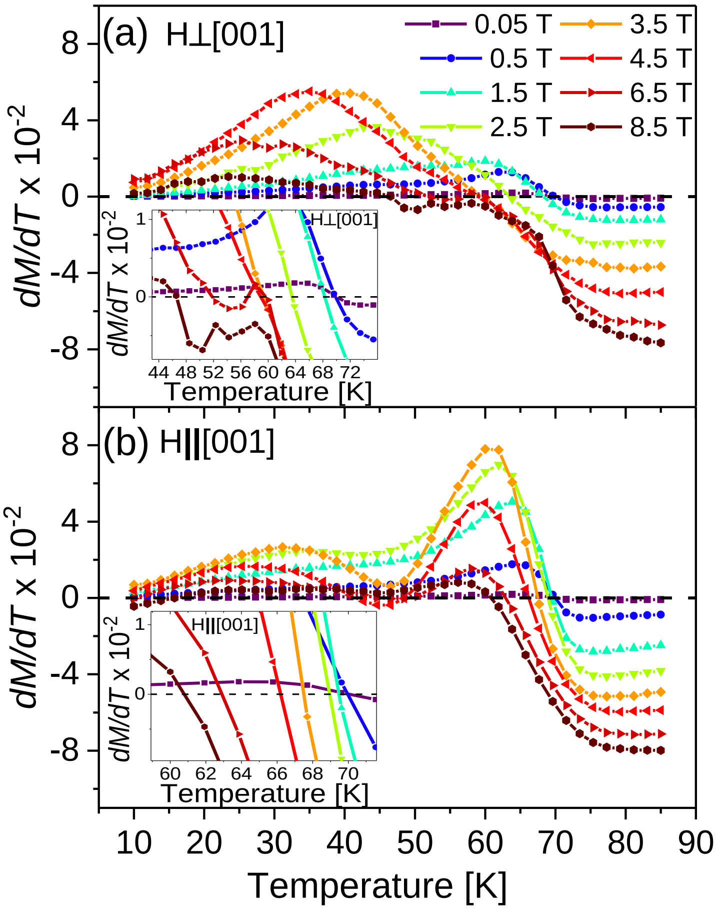

Figure 6.6.: dM/dT curves of $Mn_3Fe_2Si_3$, with (a) $\vec{H}\perp[001]$ (b) $\vec{H}||[001]$; Insert shows zoomed view where the of dM/dT curves cross the point zero. The numerical calculation of the derivative, the measured data has been re-binned to a temperature grid with step-size ~1 K.

6.3. Isothermal Magnetization

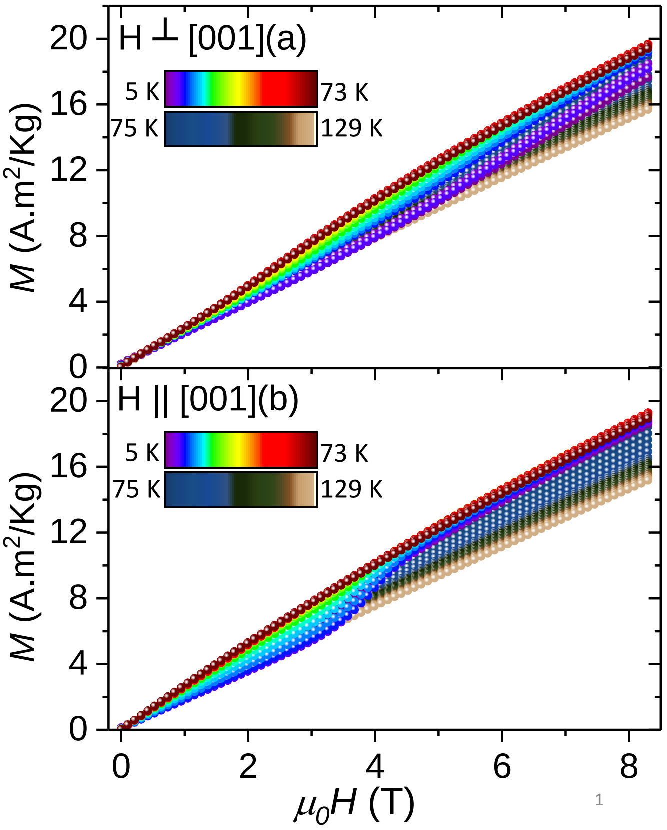

Figure 6.7.: Isothermal magnetization measurements of $Mn_3Fe_2Si_3$ at different temperatures with (a) $\vec{H}\perp[001]$ (b) $\vec{H}||[001]$. The color palettes show the temperature change of the isotherms in the range [5 K-73 K] and [75 K-129 K].

The magnetic response observed by isofield magnetization measurement was further explored by means of isothermal measurements of the magnetization in the field range from 0 T to +8.5, T, again applying the field perpendicular and parallel to the [001] direction (Figure. 6.7). Whereas, the color palettes show the temperature change of the isotherms in the range [5 K-73 K] and [75 K-129 K]. The magnetization as a function of field looks fairly similar for the direction perpendicular and parallel [001]. They approach similar values for the largest applied fields and depart from linear field dependence in the field range from 2 to 6 T. This deviation has been further analyzed by calculating the derivative $\frac{dM}{dH}$. The details about the derivation process used for isothermal data obtained with sweep and driven mode are shown in Chapter A.1.5.1.

At low temperatures, one observes an inflection point, which is easily located as a maximum in the $\frac{dM}{dH}$ curve shown in (Figure.6.8). $\frac{dM}{dH}(H)$ behaves differently depending on the direction of the field: For field applied $||[001]$ the $\frac{dM}{dH}(H)$ exhibits a

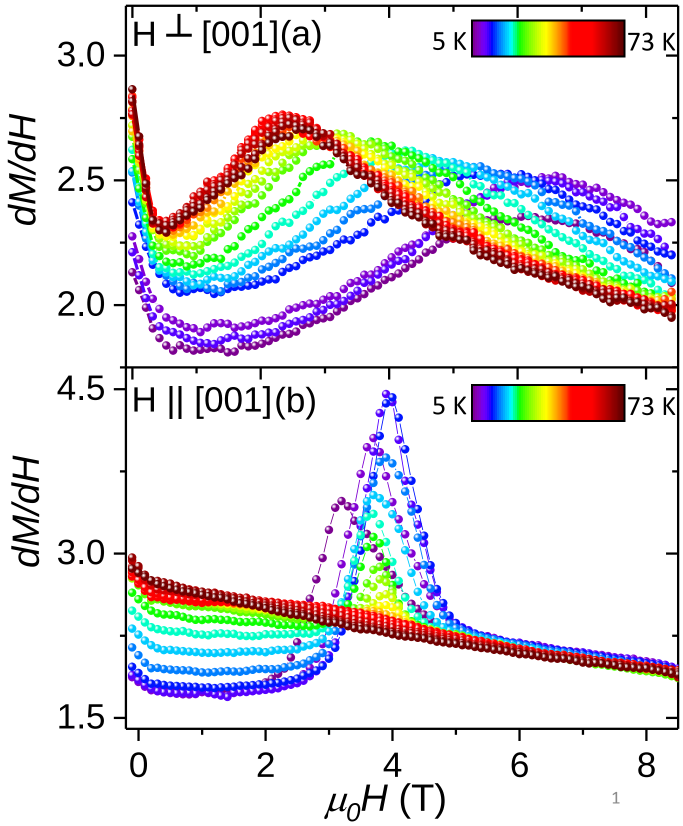

Figure 6.8.: dM/dH curves of $Mn_3Fe_2Si_3$ with (a)$\vec{H}\perp[001]$, calculated from re-binned data measured at sweep mode and (b) $\vec{H}||[001]$, calculated from raw data measured in driven mode. The color palette shows the temperature change of the isotherms in the range [5 K-73 K].

rather sharp maximum that hardly moves with temperature until it disappears completely at approximately 69 K (see Figure.6.8(b)). For the field applied ⊥ [001] (see Figure.6.8(a)), the maximum in the $\frac{dM}{dH}(H)$ is significantly broader and shifts towards lower fields with increasing temperature. The appearance of this maximum remained persistent until it disappears completely at approximately ≈120 K (see Figure.6.9).

The macroscopic response of Mn_5Si_3 has been recently revisited by means of Hall effect measurements by Sürgers *et al.* [24] and magnetization measurements up to 14 T by Das *et al.* [25], they observed an additional low-temperature high-field phase, designated $AF1'$, which was earlier observed based on neutron powder diffraction data reported by Gottschlich *et al.* [2]. The field-driven transition between $AF1'$ and $AF2$, which is evidenced by a steep increase of the magnetization in Mn_5Si_3 [24, 25], is not observed within the investigated field range for $Mn_3Fe_2Si_3$, which is in agreement with pulsed field measurements up to 38 T reported by Songlin *et al.* [4].

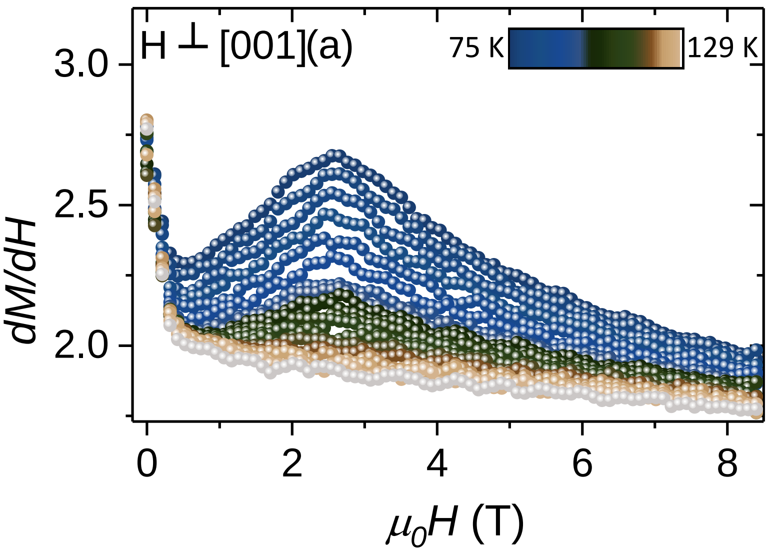

Figure 6.9.: dM/dH curves of $Mn_3Fe_2Si_3$ with $\vec{H}\perp[001]$, calculated from re-binned data measured at sweep mode and. The color palette shows the temperature change of the isotherms in the range [75 K-129 K].

6.3.1. Magnetic field vs. temperature diagram

The results of the macroscopic measurements are summarized in the magnetic field versus temperature diagrams shown in Figure 6.10. From transition observed in heat capacity measurements (Figure 6.1 and 6.1), we determine the phase boundaries $AF1$-$AF2$ and $AF2$-PM shown by open circle symbols in the diagrams (see Figure 6.10). The transition temperature between $AF2$ (purple) and PM (red) is not affected by the application of a magnetic field. Also, the transition between $AF1$ (blue) and $AF2$ (purple) is rather steep compared to the case of Mn_5Si_3 where the $AF1$-$AF2$ transition temperature decreases strongly with increasing field [24]. No evidence for a field-induced magnetic transition was observed in the magnetic heat capacity contribution results in agreement with pulsed field measurements up to 38 T reported by Songlin *et al.* [4].

In contrast to the specific heat measurements the macroscopic magnetization measurements exhibit a plethora of features, both under isothermal and under isofield conditions. Plotted in the field vs. temperature diagram Fig. 6.10, we see that the features measured under different conditions do not coincide. This hints towards a non homogeneous magnetic structure, i.e. a formation of domains, which are populated differently depending on the thermo-magnetic history. In the light of the macroscopic measurements this statement remains speculative and would require spatially resolved methods for further analysis.

The macroscopic measurements show also a clear field direction dependence in the magnetic response. Similar to the behaviors observed in Mn_5Si_3 [67], $Mn_3Fe_2Si_3$ shows an effect only in the low temperature phase when field is applied along [001].

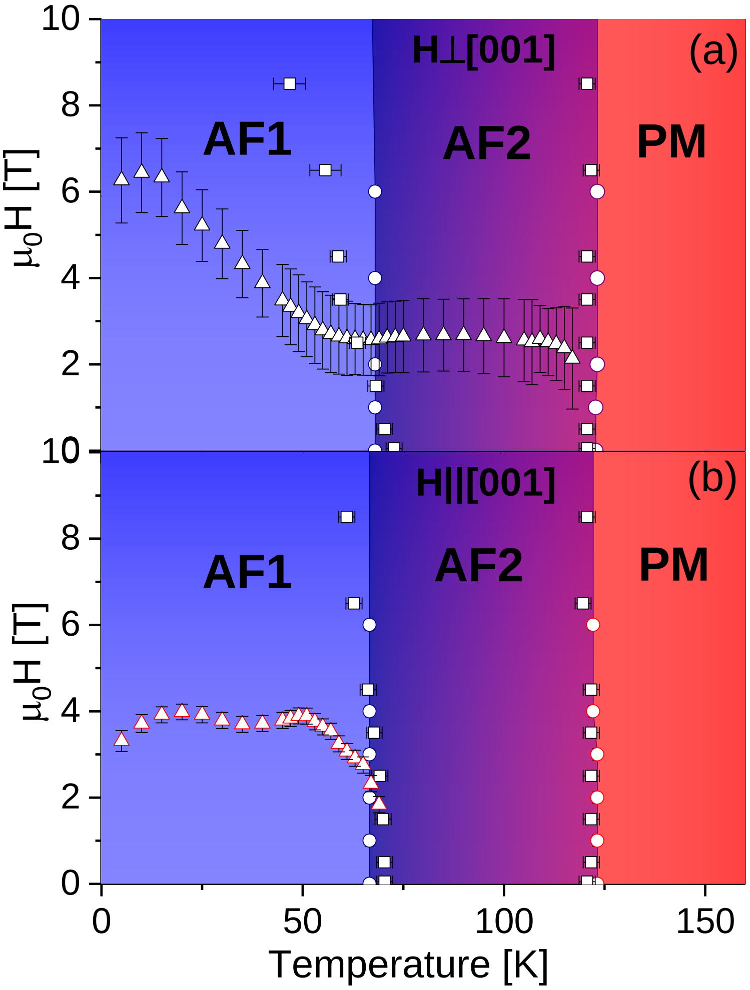

Figure 6.10.: Magnetic field versus temperature diagram. Data obtained from heat capacity measurements (circle symbols), isofield (square symbols) and isothermal (triangle symbols) measurements for the field applied perpendicular (a) and parallel (b) to the [001] direction.

If the field is applied in the perpendicular plane, we observe a feature that shifts with temperature. This feature shifts with temperature in phase $AF1$, but remains at constant field throughout $AF2$ and disappears only at $T_{AF2-PM} = 121$ K.

6.4. Magnetocaloric effect

We analyze the macroscopic magnetization results for its magnetocaloric properties on the basis of eq. 3.17. Typically, the isothermal entropy change is calculated from isothermal magnetization measurements performed at different temperatures [5, 68, 69]. While the Maxwell relation 3.16 connects the isothermal entropy change with the isofield magnetization change, this procedure is typically justified, as many MCE materials do not depend strongly on the thermo-magnetic protocol of the meausurement. As this is clearly different in the case of $Mn_3Fe_2Si_3$, we perform the numerical integration of eq. 3.17 using the isofield measurements presented in the previous chapter. Figure 6.11 shows isothermal entropy changes of $Mn_3Fe_2Si_3$ for $\vec{H}$ parallel and perpendicular to [001] (Figure 6.3) for field changes of 1.5 T, 2.5 T, 3.5 T and 4.5 T. The magneto-caloric effect shows also a field direction dependence as -ΔS_{iso} features different magnitude and shape for the different directions. For the field perpendicular [001], $-\Delta S_{iso}$ exhibits the smaller magnitude and it has a rather broad minimum, which moves with increasing field range towards lower temperature, related to the increase of the transition field with decreasing temperature.

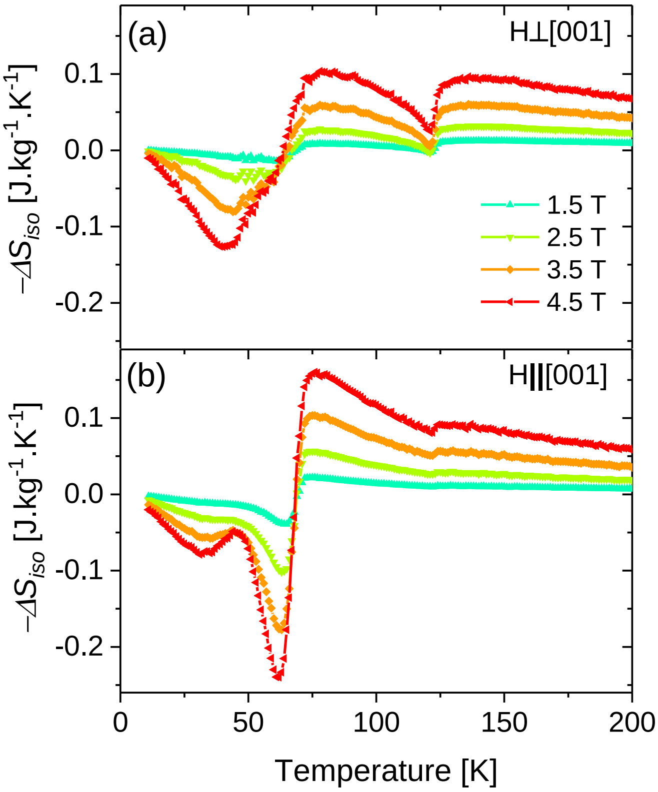

Figure 6.11.: Magnetic entropy changes as a function of temperature and field calculated from isofield magnetization measurements ,for field perpendicular (a) and parallel to [001] (b).

For the field parallel to the [001] direction, we observe an inverse MCE in a narrow temperature region around 60 K. The peak of the entropy changes hardly varies with increasing field. At 30 K we observe a second feature, which becomes more distinct, when the field is increased. For both field directions, the sign of $-\Delta S_{iso}$ changes from negative, i.e. the application of the field increases the entropy, to positive close to the transition temperature between $AF1$ and $AF2$. Also the end member

Mn_5Si_3 shows an inverse MCE, albeit much larger. The size of the inverse MCE for $Mn_3Fe_2Si_3$ is significantly reduced by a factor ~10 [4, 5]. Recently this has been attributed to the transition from the $AF1$ phase into the $AF2$ upon application of a magnetic field and a microscopic explanation on the basis of fluctuations present in the $AF2$ phase has been provided [6]. As the application of the magnetic field does not involve this transition, it seems reasonable that the entropy change is smaller in the case of $Mn_3Fe_2Si_3$ even without detailed knowledge of the magnetic structure upon application of the magnetic field. Close to the transition between $AF2$ and the paramagnetic state a downward kink develops for both field directions, which is more pronounced for the field perpendicular to [001] direction. This seems to be related to the feature observed in the isothermal measurements in the $AF2$ phase.

7. Crystal structure of Mn$_3$Fe$_2$Si$_3$

7.1. Room temperature study

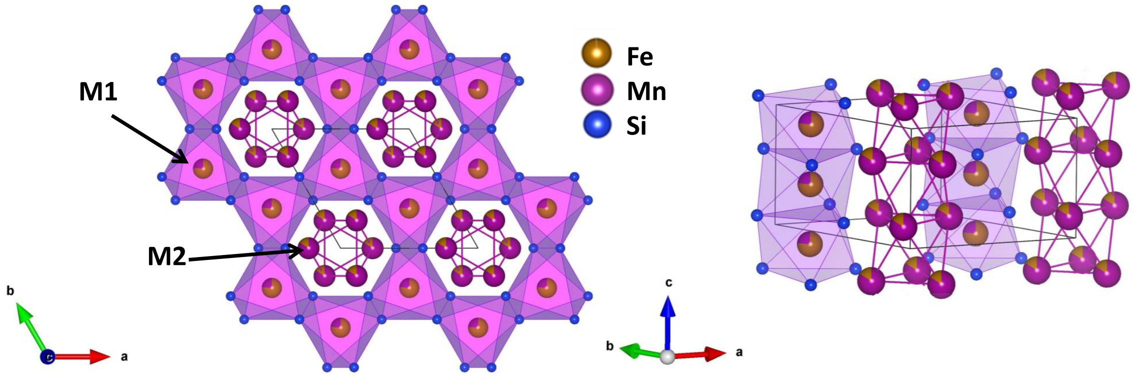

Figure 7.1.: Projection of crystal structure of Mn$_3$Fe$_2$Si$_3$ in space group $P6_3/mcm$ 300 K along (Left) [001]-direction (Right) [120]-direction.

Based on the refinement of the synchrotron X-ray single crystal diffraction data at 300 K, Mn$_3$Fe$_2$Si$_3$ crystallizes in hexagonal space group $P6_3/mcm$ with lattice parameter of a=b=6.85336(11)Å and c=4.75556(8)Å, V=193.437(5)Å^3 which is in good agreement with an earlier study reported in the literature [20], with V=193.56Å^3, a=b=6.8538(5)Å and c=4.7579(5)Å. Atomic positions of Mn$_3$Fe$_2$Si$_3$ refined from synchrotron single crystal diffraction data at 300 K are presented in table 7.1 in Appendix. According to our neutron powder refinement of Mn$_3$Fe$_2$Si$_3$ at room temperature, the M1(WP:4d) in the [M1Si$_6$]-octahedra is occupied by 76.5(1) % Fe and 23.4(1) % Mn, while the M2(WP:6g) site is occupied by 15.6(1) % Fe and 84.4(1) % Mn indicating a partial ordering of Mn and Fe.

This is in agreement with Binczycka *et al* [20], which stated a preferential incorporation of Fe into the M1 site. The same tendency was observed in MnFe$_4$Si$_3$. According to the structural model in P$\bar{6}$ reported by Hering et *al* [3], M2a is occupied by 37.6(2)% Mn and 62.8(2)% Fe; and M2b by 27.7(7)% Mn and 72.3(7) % Fe, while, M1a/M1b sites are exclusively occupied by Fe [3]. The resulting values obtained from the Rietveld refinement of Mn$_3$Fe$_2$Si$_3$ correspond to the ideal stoichiometry resulting from the weighed-in proportions. The stochiometry was also confirmed by chemical analysis using (ICP-OES) (see chapter 5.1).

Atom (WP)	x	y	z	U_{iso}	occ
Fe1 (4d)	0.666667	0.333333	0	0.00619(3)	0.12759
Mn1(4d)	0.666667	0.333333	0	0.00619	0.03907
Mn2(6g)	0.23281(3)	0	0.25	0.00788(4)	0.21092
Fe2 (6g)	0.23281	0	0.25	0.00788	0.03907
Si (6g)	0.59801(5)	0	0.25	0.00692(7)	0.25

Table 7.1.: Atomic coordinates and isotropic displacement parameters of $Mn_3Fe_2Si_3$ at 300 K from refinements of x-ray single crystal diffraction data. Occupation parameters were fixed to the values obtained from the refinement of neutron powder data.

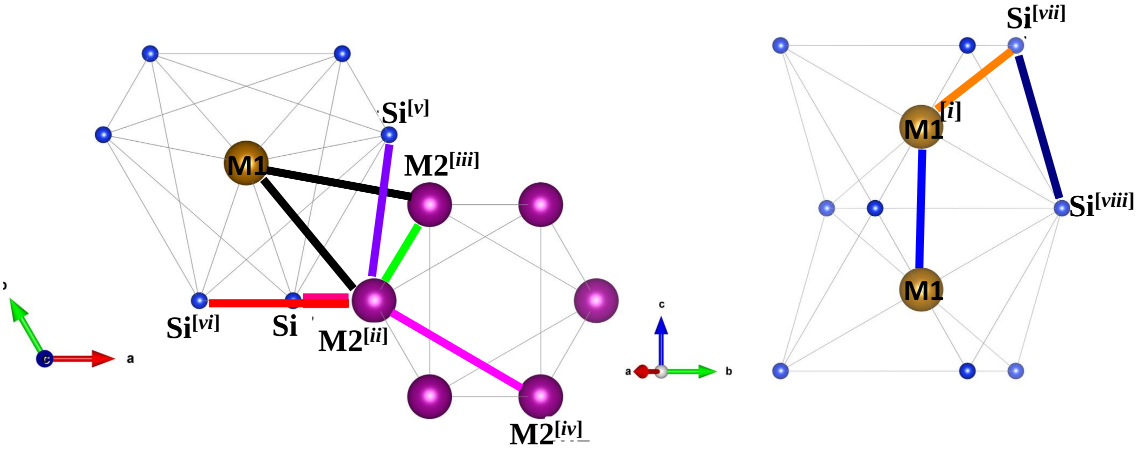

Figure 7.2.: Interatomic distances in the crystal structure of $Mn_3Fe_2Si_3$.

The Fe1/Mn1 (WP:4d) atom is surrounded by six Si atoms at distances of 2.4039(4) Å (see Table 7.2) forming an octahedra with a volume of V_P=17.295 Å^3. The octahedral volume was calculated with the program IVTON [70]. The [(Fe1/Mn1)Si_6] octahedra share common faces with their analogs forming infinite chains of composition $_\infty$[(Fe1/Mn1)Si_3] along the c axis (see Figure 7.1). The distances between the M1 (Fe1/Mn1) sites in neighbouring M1Si_6 are the shortest distances observed in the $Mn_3Fe_2Si_3$ crystal structure with d_{M1-M1}=2.3778(1) Å (see Table 7.2).

The bond angles of the [(Fe1/Mn1)Si_6] octahedra are listed in Table 7.3. The bond angles indicate that there is a distortion deviating from the ideal values of 90° (for the cis angles) and 180° (for the trans angles) for a regular octahedral geometry. The degree of octahedral distortion can be described by the angular distortion $\sum$ defined by the following formula [71]:

$$\sum = \sum_{i=1}^{12} |90 - \phi_i| \qquad (7.1)$$

Bond	d (Å)
2 × M1-M1$^{[i]}$	2.3778(1)
6 × M1-M2$^{[ii]}$/M2$^{[iii]}$	2.94629(15)
4 × M2$^{[ii]}$-M2$^{[iii]}$	2.86352(17)
2 × M2$^{[ii]}$-M2$^{[iv]}$	2.7636(3)
2 × M2$^{[ii]}$-Si	2.3958(4)
1 × M2$^{[ii]}$-Si$^{[v]}$	2.5029(4)
2 × M2$^{[ii]}$-Si$^{[vi]}$	2.6454(2)
6 × M1-Si$^{[vii]}$	2.4039(4)
2 × Si$^{[vii]}$-Si$^{[viii]}$	2.7311(4)

Table 7.2.: Interatomic distances of $Mn_3Fe_2Si_3$ in space group $P6_3/mcm$ obtained from synchrotron X-ray single crystal diffraction at 300 K (The assignment of the interatomic distances is illustrated in figure 7.2). Symmetry code: $[i]x, y, -z-1/2$, $[ii]-x+1, -y, -z$,$[iii]-y+1, x-y, z$, $[iv]-y+1, x-y, z$, $[v]y+1, -x+y, -z$, $[vi]-x+1, -y, -z$, $[vii]y, -x+y+1, -z$, $[viii]-y, x-y, z$.

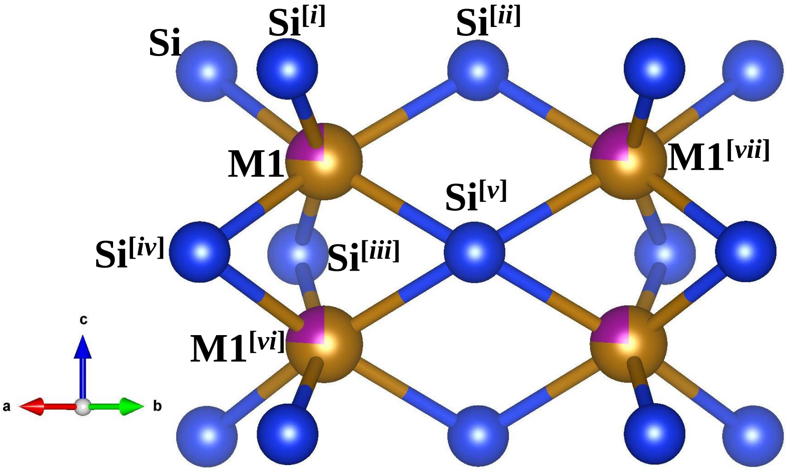

Figure 7.3.: Assignment of the bond angles in the crystal structure of $Mn_3Fe_2Si_3$.

$\sum$ describes the sum of all 12 cis-octahedral angles ϕ_i which should be ideally 90°, i.e. $\sum$ presents the local angular deviation from the octahedral angle of 90° [72]. The calculations result in a significant degree of distortion ($\sum$=133.374°).

The Fe2/Mn2 (WP:6g) atoms are interconnected to form a slightly distorted empty octahedron [□ (Fe2/Mn2)$_6$] with distances of 2.86352(17)Å and 2.7636(3)Å for M2$^{[ii]}$-M2$^{[iii]}$ and M2$^{[ii]}$-M2$^{[iv]}$, respectively(see Table 7.2). The [□ (Fe2/Mn2)$_6$] also share common triangular faces and form infinite chains of composition $_\infty$[□(Fe2/Mn2)$_3$] along the c-direction. Neighbouring $_\infty$[(Fe1/Mn1)Si$_3$] chains share common edges

Bond angles	(°)
Si-M1-Si$^{[i]}$	97.649(9)
Si-M1-Si$^{[ii]}$	97.649(9)
Si-M1-Si$^{[iii]}$	69.229(5)
Si-M1-Si$^{[iv]}$	98.389(12)
Si-M1-Si$^{[v]}$	160.482(11)
M1-Si-M1$^{[vi]}$	147.547(18)
M1-Si-M1$^{[vii]}$	110.771(8)
M1-Si-M1$^{[viii]}$	59.283(4)

Table 7.3.: Bond angles of $Mn_3Fe_2Si_3$ in space group $P6_3/mcm$ obtained from the refinement of synchrotron single crystal diffraction data at 300 K (For assignment of the bond angles see figure 7.3). Symmetry code: $[i]-y, x-y, z$, $[ii]-x+y+1, -x+1, z$, $[iii]-x+1, -y, z-1/2$, $[iv]y+1, -x+y+1, z-1/2$, $[v]x-y, x, z-1/2$, $[vi]-x+1, -y, z+1/2$, $[vii]-x+1, -y, -z$ $[viii]x, y, -z+1/2$.

with each other, forming channels occupied by the chains of empty octahedra [□ $(Fe2/Mn2)_6$](see Figure 7.1).

The [□$(Fe2/Mn2)_6$] empty octahedron have a smaller volume V_P=10.485(2)Å^3 and a significantly smaller angular distortion $\sum$=24.4168° compared to the [(Fe1/Mn1)Si_6] octahedron. For the calculations a dummy atom at position (0,0,0) in the central point of the empty octahedra was introduced. Silicon atoms are surrounded by four M1 atoms at equal distances of 2.4039(4)Å and by five M2 atoms at distances ranging from 2.3958(4)-2.6454(2)Å (see Table 7.2).

7.2. Evolution of the structure as a function of temperature

Figure 7.4 shows the reciprocal space section of the (h0l) plane reconstructed from single crystal synchrotron XRD measurements of $Mn_3Fe_2Si_3$ at 300 K and 20 K. All reflections can be indexed assuming a hexagonal cell. All reflection observed in the (h0l) and (0kl) plane measured at 300 K fulfil the reflection condition $l = 2n$. This reflection condition is not violated even at 20 K, showing extinction rules in accordance with space group $P6_3/mcm$ down to the lowest measured temperature (see Figure 7.4). As, in addition, no splitting of reflections is observed, there is no hint towards a structural phase transition at low temperatures, as observed for Mn_5Si_3 [22, 23, 2].

The lattice parameters and the unit cell volume of $Mn_3Fe_2Si_3$ as a function of temperature are shown in Figure 7.5 and 7.6, respectively. All unit cell parameters were refined from the synchrotron single crystal diffraction measured during cooling. Values are also listed in the appendix A.6). As can be seen in Figure 7.5, the lattice parameter ($a = b$, c) and the unit cell volume decrease smoothly as the temperature

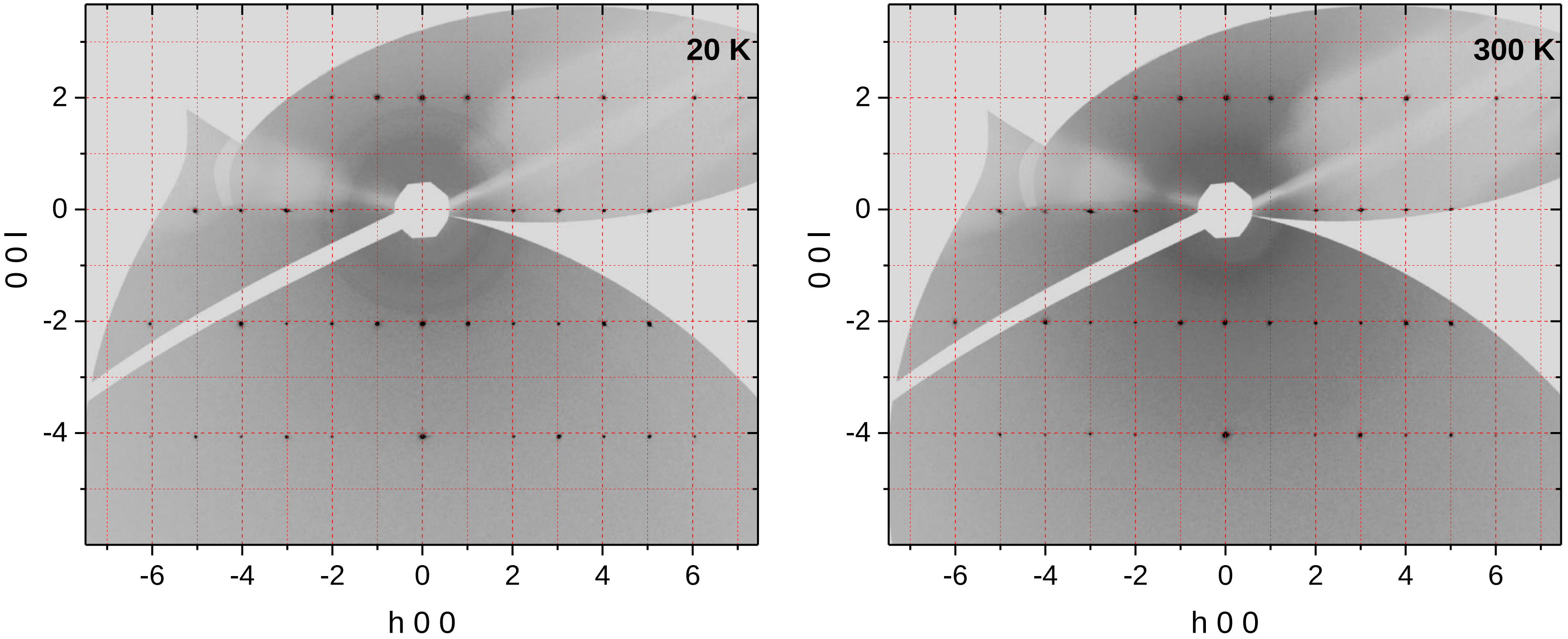

Figure 7.4.: Reciprocal space reconstruction of the (h0l) plane based on the single crystal synchrotron XRD measurements of $Mn_3Fe_2Si_3$ at (Right) 300 K and (Left) 20 K; the reciprocal lattice is indexed on the basis of the hexagonal cell.

decreases, with the slope decreasing towards lower temperatures. Figure 7.6 shows the normalized values of $a = b$, c, $\frac{c}{a}$ ratio and unit cell volume as a function of temperature normalized to the value at 300 K. Here, it is clearly seen that the value of the c-lattice parameter decreases more than the value of the a (b)-lattice parameter. As a consequence the $\frac{c}{a}$ ratio is also decreased with decreasing temperature. As can be seen from Figure 7.5, and 7.6, there is no clear sign of the response of the lattice parameters at the temperatures corresponding to the magnetic transitions $AF1 - AF2$ and $AF2 - PM$ (as determined from our macroscopic studies of $Mn_3Fe_2Si_3$). Figure 7.7 shows the volumetric thermal expansion $\alpha(T)$ of $Mn_3Fe_2Si_3$ obtained from $\alpha(T) = \left[\frac{1}{V(T)}\right]\left(\frac{dV}{dT}\right)$ [73]. $\alpha(T)$ increases slightly down to 200 K, then starts to decrease with decreasing temperature, and shows a slight response to the magnetic transitions $AF1 - AF2$.

The free atomic coordinate of x(Mn2/Fe2) decreases rapidly down to 125 K, then the decrease gets less and starts to become more linear. On the other hand, the free atomic coordinate x(Si) is within error nearly constant and only shows a slight increase with increasing temperature (see Figure A.21 in appendix).

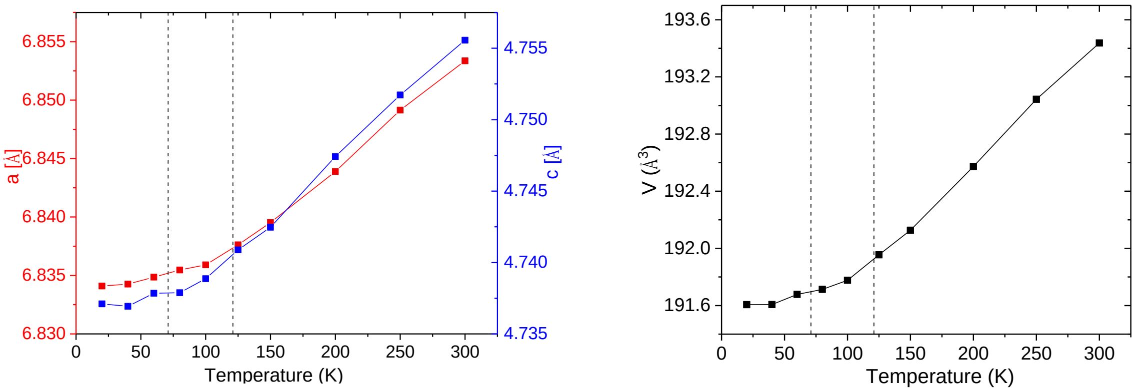

Figure 7.5.: Unit cell volume, a (b) and c-lattice parameter of $Mn_3Fe_2Si_3$ as a function of temperature obtained from synchrotron X-ray single crystal diffraction data measured during cooling down. Temperatures of AF1-AF2 and AF2-PM transitions are indicated by dashed lines. (Estimated standard deviations are smaller than the symbols).

Figure 7.8 shows selected interatomic distances as a function of temperature (normalized to the value at 300 K) (absolute values are given in appendix A.12). Within standard deviations, all interatomic distances decrease with decreasing temperature with no clear sign of a response to the two magnetic transitions $AF1 - AF2$ and $AF2 - PM$. The interatomic distances between the metal atoms located on the same sites (M1-M1, M2-M2', M2-M2") are significantly more reduced than the distances between metal atoms located on different sites (M1-M2). Interatomic M1-Si and Si-Si distances decrease in general less than M-M distances (see Figure 7.8). The change in interatomic distances within both types of octahedra, [(Fe1/Mn1)Si_6] and [□ (Fe2/Mn2)$_6$], is reflected in the change of their polyhedral volumes V_P. Figure

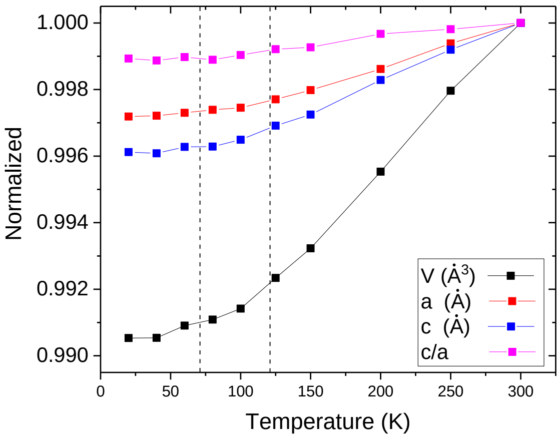

Figure 7.6.: Normalized $a(b)$, c, $\frac{c}{a}$ ratio and unit cell volume of $Mn_3Fe_2Si_3$ as a function of temperature (normalized to the value at 300 K), based on refinements from synchrotron X-ray single crystal diffraction data measured during cooling down. Temperatures of the AF1-AF2 and AF2-PM transitions are indicated by dashed lines

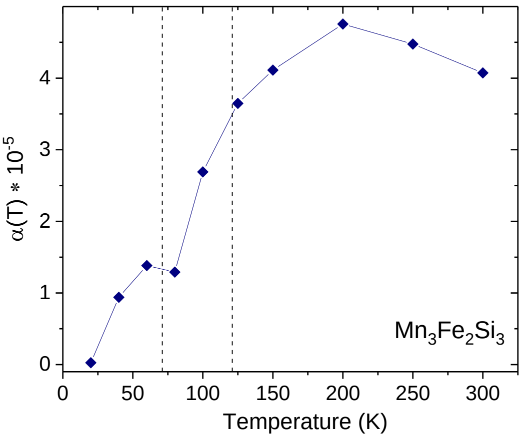

Figure 7.7.: Volumetric thermal expansion coefficient of $Mn_3Fe_2Si_3$ as a function of temperature. Temperatures of the AF1-AF2 and AF2-PM transitions are indicated by dashed lines

7.9 shows the normalized volumes of the unit cell V_{total}, the coordination polyhedra V_P, [(Fe1/Mn1)Si_6], [□ (Fe2/Mn2)$_6$] and the channel occupied by [□ (Fe2/Mn2)$_6$] as a function of temperature. The volumes of [(Fe1/Mn1)Si_6] octahedra and the channel where the [□ (Fe2/Mn2)$_6$] octahedra are incorporated decrease with decreasing temperature in the same way as the unit cell volume. On the other hand, the volume of the [□ (Fe2/Mn2)$_6$] octahedra has a significantly larger decrease in volume in comparison to the volume of the channel where they are incorporated. This might indicate that with decreasing temperature the complete chain of [□ (Fe2/Mn2)$_6$] octahedra

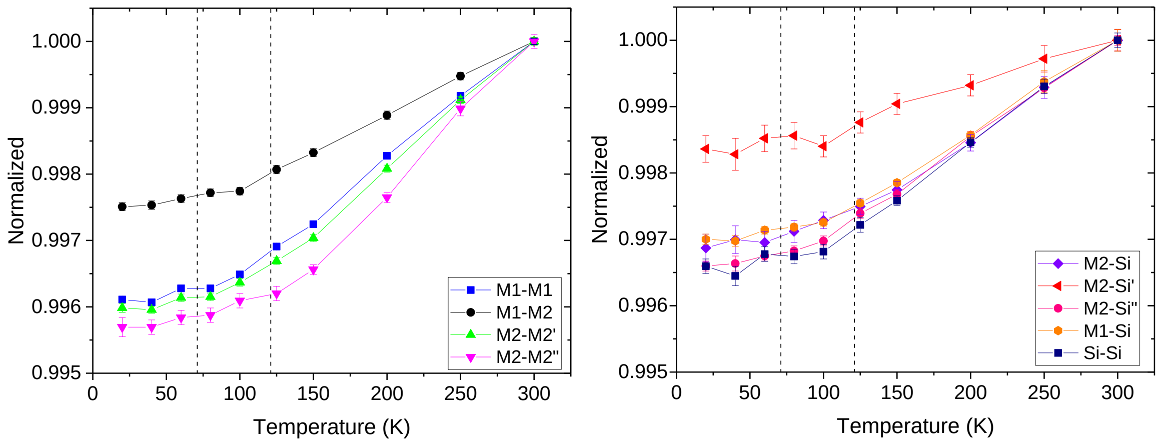

Figure 7.8.: Temperature dependence of selected interatomic distances of $Mn_3Fe_2Si_3$ as a function of temperature, normalized to the value at 300 K, obtained on the basis of refinements from synchrotron X-ray single crystal diffraction data measured during cooling down; Temperatures of the AF1-AF2 and AF2-PM transitions are indicated by dashed lines. The assignment of the distances is shown in Figure 7.2.

has more space to vibrate within the channel.

Figure 7.10 shows the normalized angular distortion $\sum$ of [(Fe1/Mn1)Si_6] and [□ (Fe2/Mn2)$_6$] octahedra as a function of temperature normalized to the value at 300 K. As can be seen, the angular distortion of [□ (Fe2/Mn2)$_6$] octahedra shows a pronounced variation compared to the behaviour of the [(Fe1/Mn1)Si_6]. It is striking that the distortion of the [□ (Fe2/Mn2)$_6$] octahedra increases significantly down to 125 K. At 125 K, i.e. at the temperature of the $AF2{-}PM$ transition a sudden decrease is observed which might well be related to the onset of magnetic ordering.

7.3. Comparison of the temperature dependent behavior of the $Mn_{5-x}Fe_xSi_3$ compounds (x=0, 2, 4)

As already mentioned in first chapter, the unit cell size of $Mn_{5-x}Fe_xSi_3$ decreases with increasing Fe content [20] and $Mn_3Fe_2Si_3$ has a smaller unit cell volume $V^{300K}_{Mn_3Fe_2Si_3} = 193.437(5)\text{Å}^3$ compared to the parent compound Mn_5Si_3, $V^{300K}_{Mn_5Si_3} \approx 199.38\text{Å}^3$ [20, 2]. This change in the unit cell volume is due to a small difference of the atomic radius between iron r(Fe)=156 pm and Manganese r(Mn)=161 pm [74].

Figure 7.12 shows comparison of c and a lattice parameter normalized at 300 K, for the x=2 compound studied in this work with the Mn end member x=0 [20, 2] and the Fe-rich compound x=4 [3] in the $Mn_{5-x}Fe_xSi_3$ system. For $MnFe_4Si_3$, no structural phase transition was observed in [3]. The thermal expansion shows a clear response

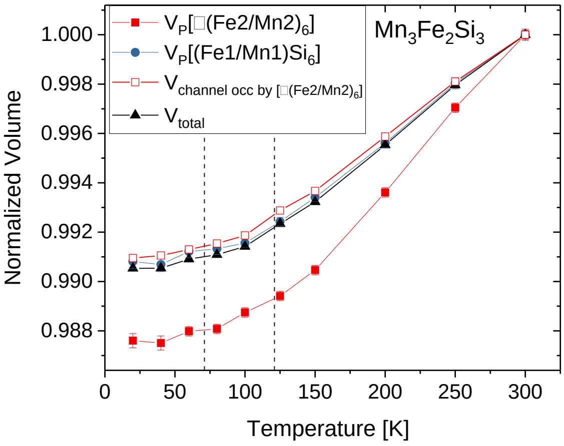

Figure 7.9.: Normalized volumes of the unit cell V$_{total}$, the coordination polyhedra [(Fe1/Mn1)Si$_6$], [□ (Fe2/Mn2)$_6$] and the channel occupied by [□ (Fe2/Mn2)$_6$] as a function of temperature in $Mn_3Fe_2Si_3$ (Values are normalized to the volumes at 300 K). Temperatures of the AF1-AF2 and AF2-PM transitions are indicated by dashed lines.

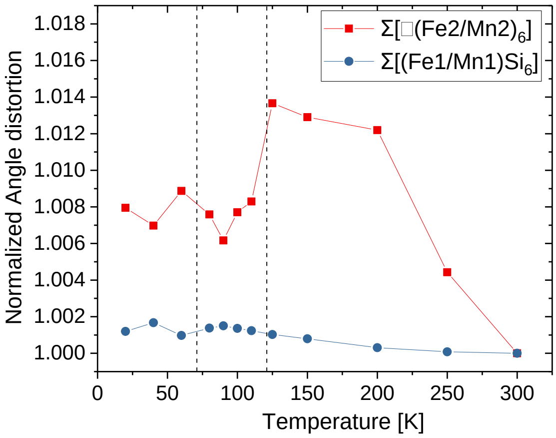

Figure 7.10.: Normalized angular distortion of [(Fe1/Mn1)Si$_6$] and [□(Fe2/Mn2)$_6$] octahedra as a function of temperature in $Mn_3Fe_2Si_3$ (Values are normalized to the volumes at 300 K). Temperatures of the $AF1 - AF2$ and $AF2 - PM$ transitions are indicated by dashed lines.

associated with the ferromagnetic ordering in $MnFe_4Si_3$ [3] (see figure 7.11 (left). Both lattice parameters show different variations indicating strong anisotropy in the compound. The c lattice parameter decreases with decreasing temperature, while $a = b$ shows a slight increase associated with a ferromagnetic ordering (see Figure 7.12) [3]. The increase of the interatomic distances M2-M2 is accompanied with ferromagnetic coupling of spins on the sites with mixed occupancy Fe2/Mn2, this is reflected in the increase of the [□ (Fe2/Mn2)$_6$] octahedra with a significantly larger decrease in the volume of their host channel (see Figure 7.13), this leads to an increase in the $a = b$ lattice parameter [3]. In contrast to this, Mn_5Si_3 exhibits a structural phase transition at T_{PM-AF2} from hexagonal $P6_3/mcm$ to orthorhombic $Ccmm$ accompanied with an increase of a and c lattice parameters and a decrease in the b-lattice parameter (see Figure 7.12) [22, 2]. The Mn_5Si_3 structural phase transition at T_{PM-AF2} from hexagonal $P6_3/mcm$ to orthorhombic $Ccmm$ is also associated with a sudden decrease of the thermal expansion, which then notably increases at $T_{AF2-AF1}$.

In difference to these two compounds, the lattice parameter of $Mn_3Fe_2Si_3$ decrease smoothly as the temperature decreases with no clear sign of a structural phase transition nor with any indication of a clear response of the lattice parameter to the magnetic transitions (see Figure 7.4). On the other hand the thermal expansion shows a slight response associated to $AF1 - AF2$ transition. The concave shape of $\alpha(T)$ in the temperature region [121-300] K might be associated to the short range magnetic correlations observed in our macroscopic studies of $Mn_3Fe_2Si_3$ (see chapter 6).

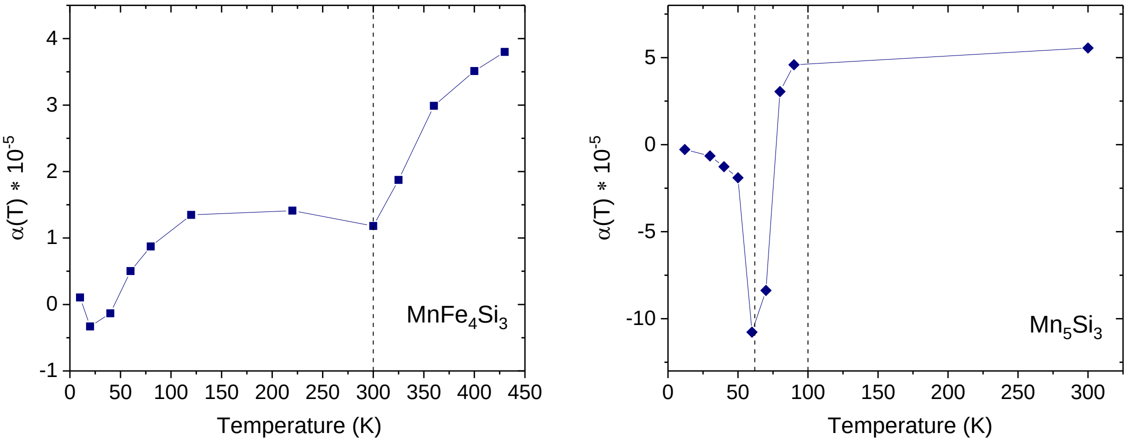

Figure 7.11.: Volumetric thermal expansion coefficient as a function of temperature of (left) $MnFe_4Si_3$ [3] and (right) Mn_5Si_3 [2]. Dashed lines indicate (left) the temperatures of the FM-PM transition in $MnFe_4Si_3$ and (right) the $AF1 - AF2$ and $AF2 - PM$ transition in Mn_5Si_3

According to the literature [2, 22], the orthorhombic distortion which accompanies the formation of the $AF2$ structure in Mn_5Si_3 results in a shortening of the distances between antiferromagnetically coupled M2-M2 atoms. This leads to a significant decrease in the volume of $[\square(M2)_6]$ octahedra compared to the volume of the channel where they are incorporated and the $[(M1)Si_6]$ octahedra volume (see Figure 7.13). This is somewhat similar to what we observe in our compound $Mn_3Fe_2Si_3$ at $AF2 - PM$. However, the unit cell and polyhedral volumes in $Mn_3Fe_2Si_3$ continue to decrease smoothly down to the temperatures corresponding to the stability field of $AF1$ with no clear sign of a response to the magnetic transitions $AF1 - AF2$ (see Figure 7.9). In contrast to this, an expansion of the c-lattice parameter was observed in Mn_5Si_3

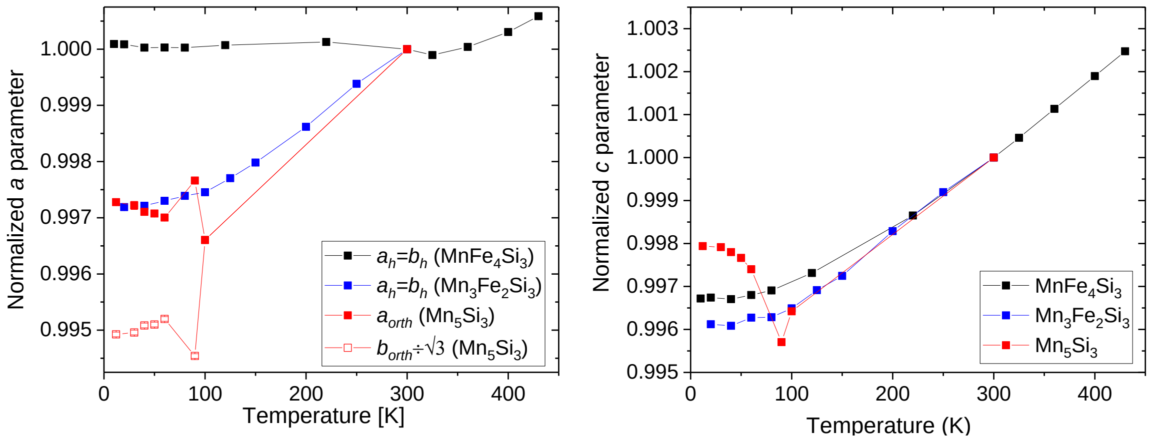

Figure 7.12.: Comparison of a (Left) and c-lattice parameter (Right) for the three individual compounds $Mn_{5-x}Fe_xSi_3$ with x=0[2], 2[This work], 4[3]. (For Mn_5Si_3 in the orthorhombic phase the b-lattice parameter has been divided by $\sqrt{3}$). Values are normalized to the one at 300 K

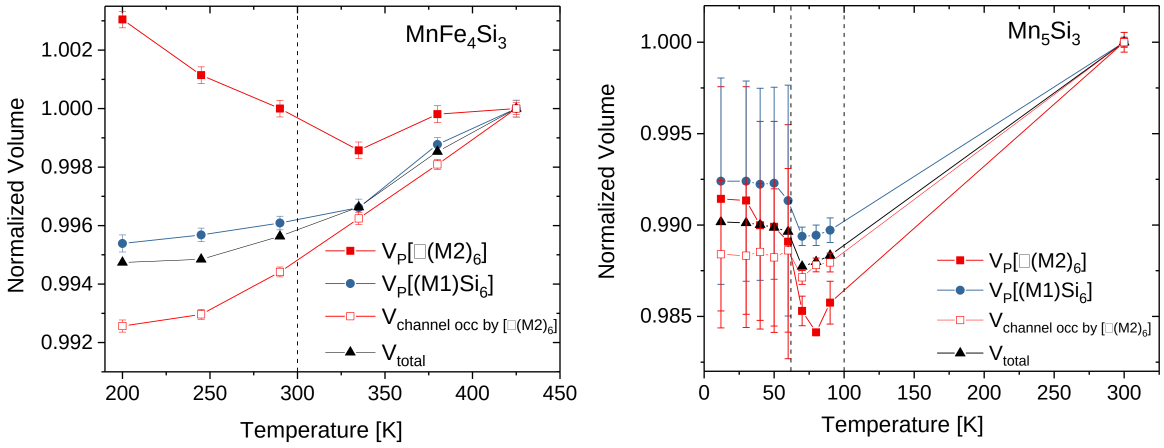

Figure 7.13.: Normalized volumes of the unit cell V_{total}, the coordination polyhedra $[(M1)Si_6]$, $[\square(M2)_6]$ and channel occupied by $[\square\ (M2)_6]$ as a function of temperature in (left) $MnFe_4Si_3$ (Values are normalized to the volumes at 425 K)[3] and (right) Mn_5Si_3 (Values are normalized to the volumes at 300 K) [2]. Dashed lines indicate (left) the temperatures of the FM-PM transition in $MnFe_4Si_3$ and (right) the AF1-AF2 and AF2-PM transition in Mn_5Si_3

at the $AF2-AF1$ transition which leads to a larger M1-M1 distance ($= 0.5\ c$) in the $AF1$ phase, this way enabling the ordering of the moments on the M1 site, which is suppressed by the smaller M1-M1 distance in the $AF2$ phase [22, 75]. On transition to the $AF1$ phase, the distance between the M1 and M2 system are shortened, while the M2-M2 distances expand. As a consequence the volume of $[\square\ (Fe2/Mn2)_6]$ octahedra also expand (see Figure 7.13).

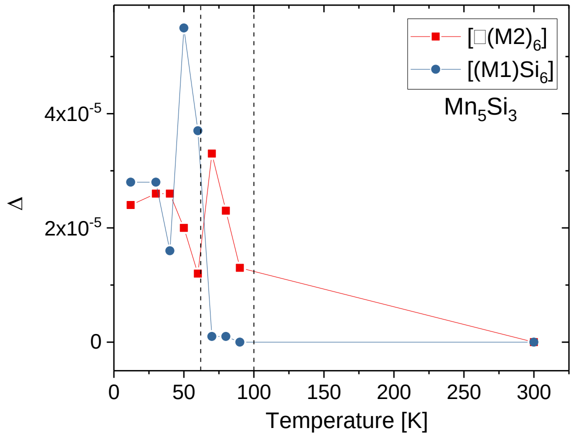

Figure 7.14.: Distance distortion Δ of $[(M1)Si_6]$ and $[\square\,(M2)_6]$ octahedra as a function of temperature in Mn_5Si_3 (Values are normalized to the volumes at 300 K) [2]. Temperatures of the AF1-AF2 and AF2-PM transitions are indicated by dashed lines.

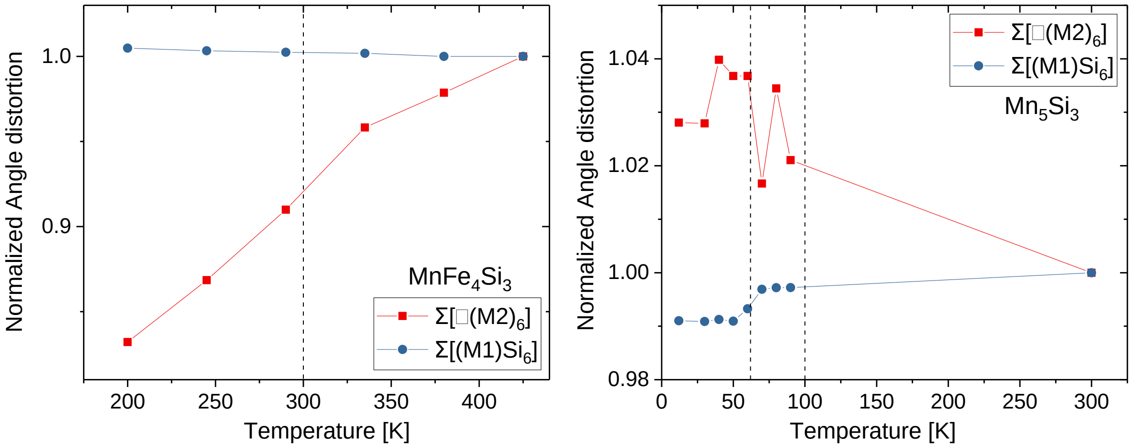

Figure 7.15.: Normalized angular distortion of $[(M1)Si_6]$ and $[\square\,(M2)_6]$ octahedra as a function of temperature in (left) $MnFe_4Si_3$ (Values are normalized to the volumes at 425 K)[3] and (right) Mn_5Si_3 (Values are normalized to the volumes at 300 K) [2]. Dashed lines indicate (left) the temperatures of the FM-PM transition in $MnFe_4Si_3$ and (right) the AF1-AF2 and AF2-PM transition in Mn_5Si_3

In difference to $Mn_3Fe_2Si_3$ and $MnFe_4Si_3$ where all six Mn-Si distances in the octahedra are equal at all temperatures, in Mn_5Si_3 a sudden increase of the distance distortion parameter $\Delta[\square\,(M2)_6]$ octahedra was observed at the temperature of the magnetostructural transition ($PM - AF2$) and Δ[(M1)Si_6] increases even further at the temperature of the $AF2 - AF1$ transition (see Figure 7.14).

Figure 7.15 shows the normalized angular distortion $\sum$ of [(M1)Si_6] and [□ $(M2)_6$] octahedra as a function of temperature normalized to the value (left) at 425 K for $MnFe_4Si_3$ and (right) at 300 K for Mn_5Si_3. As can be seen in figure 7.15, in both compounds, the angular distortion of the [□$(M2)_6$] octahedra shows a more pronounced variation compared to the behaviour of the [(M1)Si_6] octahedra, with a sudden change at the temperature corresponding to the magnetic ordering. This was also observed for $Mn_3Fe_2Si_3$ and this presumably indicates the close relation of the angular distortion to the magnetic ordering.

8. Magnetic structures of $Mn_3Fe_2Si_3$

8.1. Magnetic scattering in $Mn_3Fe_2Si_3$ as seen by single crystal neutron scattering

In Figure 8.1 we present elastic scattering maps recorded at the TOF spectrometer MERLIN at 5 K and at 125 K with E_i=21 meV.

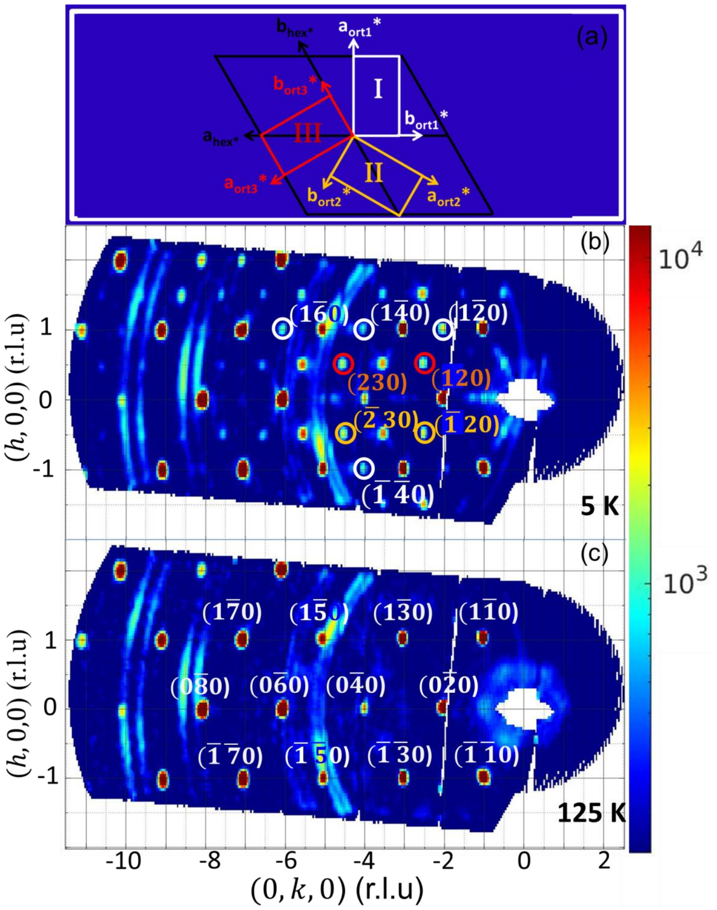

Figure 8.1.: (a) The reciprocal lattices of the three orthorhombic twin individuals. Elastic scattering map of the (hk0) plane measured on Merlin at T=5 K (b) and at T=125 K (c), with E_i=21 meV. The colour code refers to the three different twins. A logarithmic scale was used for the colour axis.

At high temperature, all peaks can be indexed using the orthohexagonal setting corresponding to space group $Ccmm$. Powder rings originate from the sample environment. When the temperature is reduced to 5 K additional reflections appear. They are more than an order of magnitude weaker in intensity and also have a decreasing intensity for increasing momentum transfer as expected for magnetic Bragg peaks due to the magnetic form factor. Taking the orthohexagonal setting as a basis for indexation, the new reflections can be sorted into two groups: the first group of reflections can be indexed with integer values of (hkl) with $h + k = 2n + 1$ indicating the loss of the C-centering. Using the same basis vectors a^* and b^*, the second group of reflections fall onto reflection positions with half-integer values. All reflections can be explained by the formation of three different twin domains which are formed due to the symmetry reduction at the phase transition from hexagonal to orthorhombic; their lattices are related by the 3-fold axis of the hexagonal system (see Figure 8.1 (a)). All observed magnetic reflections can then be indexed with a magnetic propagation vector of (010) referring to the basis of one of the twin domains.

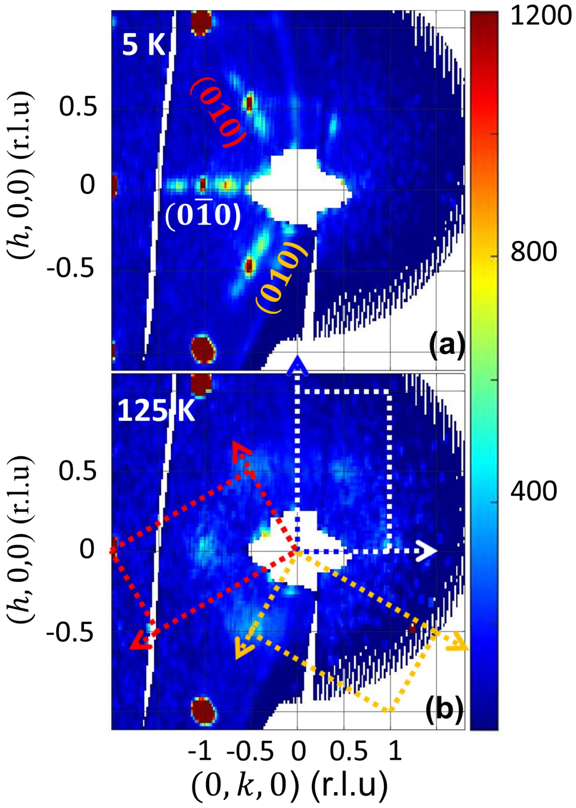

Figure 8.2.: Elastic scattering map of the $(hk0)$ plane measured on Merlin at low Q values with (a) T=5 K, (b) at T=125 K, E_i=13 meV. The colour code refers to the three different orthorhombic twins used to index the reflections. A linear scale was used for the colour axis.

Figure 8.2 shows the low Q region in the $(hk0)$ plane at 5 K and 125 K with E_i=13 meV. The three orthorhombic twin individuals used to index the reflections are shown in 8.2.b). At 5 K we observe rather well defined peaks (0-10) for all three twin individuals. Additionally there seem to be diffuse satellite-like reflections along the [010] direction, which are only observed at these very low angles.

This was also observed in the equivalent magnetic reflections (010) that belong to the second and third twin individual (see Figure 8.2.a). At 125 K, i.e. 5 K above the transition temperature as identified from the macroscopic measurements, we observe still diffuse intensity around the (0-10) positions, most likely indicating the presence of short range magnetic correlations. This observation is in good agreement with the increased response of $\frac{M}{B}$ for small applied field in the temperature range between 120 K and 270 K. (see chapter 6.3).

The temperature dependence of integrated intensities of two different magnetic reflections from two different twin individuals are shown in Figure 8.3. It is obvious that the reflection $(1\bar{4}0)$, which belongs to twin individual I, appears already below 125 K, while the intensity of the second reflection (120), belonging to another twin individual $((0.5, \overline{2.5}, 0)$, if indexed in the basis of twin individual $I)$, increases only below 70 K.

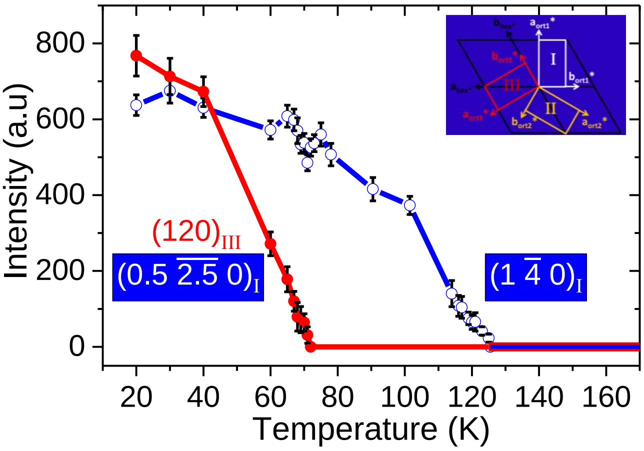

Figure 8.3.: Temperature dependence of magnetic $(1\bar{4}0)$ and (120) Bragg peak intensities from two different twin individuals from data taken of E4 of BER II. Note that the reflections are indexed with respect to the orthohexagonal basis of the respective twin domain to which they belong.

8.2. Determination of the magnetic structures of $Mn_3Fe_2Si_3$ from neutron powder diffraction data

Figure 8.4 shows different d(Å) regions of $Mn_3Fe_2Si_3$ neutron powder diffraction diagrams obtained on POWGEN at different temperatures using large wavelength bandwidth of 2.665Å (the patterns obtained with short wavelength bandwidth are shown in Figure A.24 in Appendix).

The space group describing the symmetry of $Mn_3Fe_2Si_3$ is $P6_3mcm$. No structural phase transition was observed in $Mn_3Fe_2Si_3$ at low temperatures according to our synchrotron data (see chapter 7). This is also in accordance with the refinement of the nuclear structure using the neutron powder diffraction data.

Starting from the nuclear structure and assuming one magnetic propagation vector $k = (\frac{1}{2}\frac{1}{2}0)$ referred to the hexagonal cell (space group: $P6_3mcm$) and in accordance with the twin model described above we obtained the same eight models derived from the *Ccmm* space group of the parent structure and the propagation vector $k = (010)$ (see chapter A.1.2.6). Therefore, in the following the nuclear structure of $Mn_3Fe_2Si_3$ will be described in the orthohexagonal setting corresponding to the *Ccmm* cell (subgroup of $P6_3mcm$) which was also chosen in the literature for the description of the parent compound Mn_5Si_3 [2, 22, 23]). The use of the orthorhombic subgroup *Ccmm* implies that the Fe2/Mn2 site from the hexagonal setting is described by a splitted wyckoff position Fe21/Mn21 and the Fe22/Mn22 sites in the orthorhombic space group [1].

Agreement factors for the refinement of the nuclear structure are shown in table A.13 in the Appendix. Results of the nuclear structure refinement performed on the powder diffraction data taken at 20 K, 50 K, 90 K and 105 K are presented in Table 8.1.

<table>
<tr><td colspan="7">Space group: <i>Ccmm</i>,
Fe1/Mn1 occupy WP 8(e) $(-\frac{1}{2}, -\frac{1}{6}, 0)$
Fe21/Mn21 and Si1 occupy WP 4(c) $(x_1, 0, \frac{1}{4})$
Fe22/Mn22 and Si2 occupy WP 8(g) $(x_2, y_2, \frac{1}{4})$
with $x_2 = \frac{x_1}{2}$ and $y_2 \approx x_2$</td></tr>
<tr><td>T</td><td>a</td><td>b</td><td>c</td><td>x_1(Fe21/Mn21)</td><td>x_1(Si1)</td><td>U_{iso}</td></tr>
<tr><td>105 K</td><td>6.8429 (1)Å</td><td>11.8523Å</td><td>4.7450(1)Å</td><td>-0.2260(5)</td><td>-0.5980(2)</td><td>0.0024(1)</td></tr>
<tr><td>90 K</td><td>6.8421 (1)Å</td><td>11.8509Å</td><td>4.7441(1)Å</td><td>-0.2258(5)</td><td>-0.5981(3)</td><td>0.0024(1)</td></tr>
<tr><td>50 K</td><td>6.8405 (1)Å</td><td>11.8482Å</td><td>4.7427(1)Å</td><td>-0.2261(5)</td><td>-0.5979(3)</td><td>0.0022(1)</td></tr>
<tr><td>20 K</td><td>6.8395 (2)Å</td><td>11.8464Å</td><td>4.7423(1)Å</td><td>-0.2261(5)</td><td>-0.5981(4)</td><td>0.0022(1)</td></tr>
</table>

Table 8.1.: Unit cell parameters, atomic coordinates and isotropic displacement parameters of $Mn_3Fe_2Si_3$ for 105 K, 90 K, 50 K and 20 K. All parameters were restricted to obey the higher hexagonal symmetry $P6_3/mcm$.

The neutron powder diffraction diagrams of $Mn_3Fe_2Si_3$ show the appearance of new Bragg peaks of magnetic origin at 105 K close to d-values of 2.10 Å, 2.15 Å, 3 Å and 11.75 Å. At 50 K additional magnetic peaks exist close to 2.6 Å, 3.1 Å and 4.5Å (see Figure 8.4). In agreement with the observation of neutron single crystal diffraction

---

[1] It should be pointed out here that in all the subsequent refinements the nuclear structure was restricted to obey the higher hexagonal symmetry with the help of local symmetry operations.

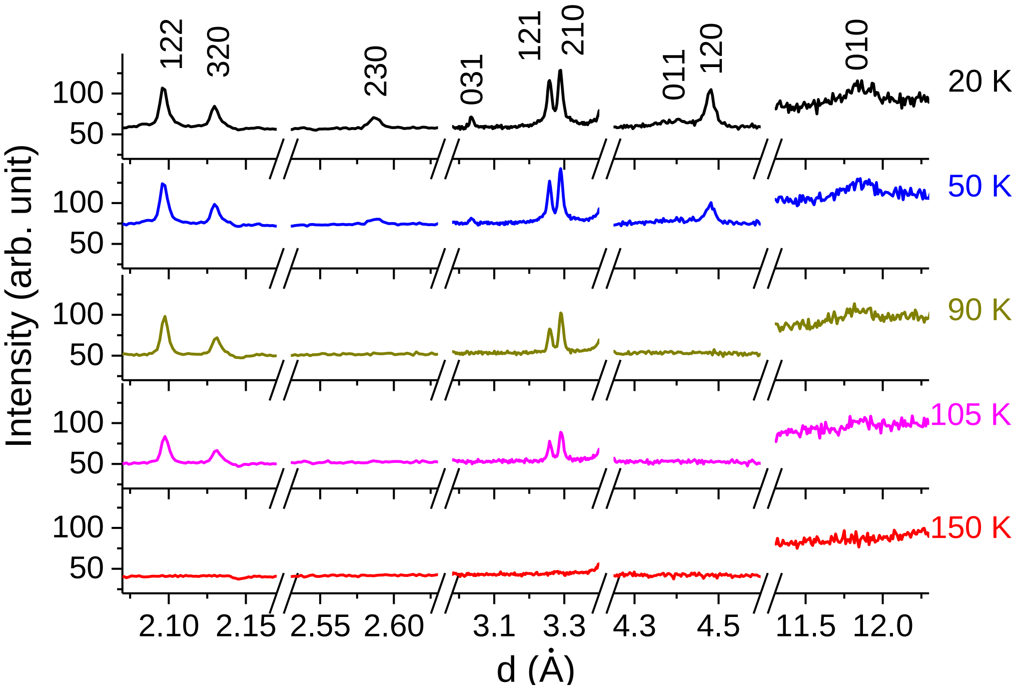

Figure 8.4.: $Mn_3Fe_2Si_3$ neutron powder diffraction obtained on POWGEN at different temperatures for a center wavelength of 2.665 Å. The d(Å) regions with the strongest magnetic Bragg reflections indexed using the *Ccmm* space group are shown.

measured at E4 of BER II, the integrated intensity of the magnetic (120) reflection appears only at temperatures lower than $T_{N1} \approx 70\,K$ (see Figure 8.3).

These magnetic peaks are more than an order of magnitude weaker in intensity compared to the nuclear Bragg peaks (see Figure A.23 in Appendix), and they have reflection positions violating the extinction rules for the *C*-centering ($hkl : h + k = 2n + 1$) (see Figure 8.4). They can be indexed with a magnetic propagation vector (010) along the orthohexagonal *b* direction, as already observed in the single crystal elastic scattering maps recorded at the TOF spectrometer MERLIN.

In order to determine the magnetic structure from neutron diffraction of $Mn_3Fe_2Si_3$ we used the concept of Shubnikov groups (magnetic space groups) (see chapter 3.4.1.1), which combine the crystal symmetry with the time reversal operation. In order to generate all possible magnetic structures that are compatible with the parent nuclear structure (*Ccmm* space group), we have used the mathematical derivation of the grey, black and white space groups implemented in the Jana program [76]. In this case, the corresponding grey group of *Ccmm* which includes the time inversion is $Ccmm1'$. The symmetry of a magnetically ordered phase is then described by a subgroup of this parent group. Table 8.2 summarizes the maximal magnetic space groups (MGS) for the parent space group *Ccmm* and the propagation vector (010), and the allowed magnetic moment directions for the different magnetic models. Only eight maximal magnetic symmetries for magnetic ordering are possible.

The moments on the Fe1/Mn1 sites are restricted to lie either in the a, c plane or they have to be parallel to b. For the Fe21/Mn21 and Fe22/Mn22 sites, four of the models restrict the spins to lie in the a, b-plane, while in the other four models only components along c are allowed (see Table 8.2).

Shubnikov space groups	Allowed magnetic moments ($M_{x,y,z}$)		
	Fe1/Mn1	Fe21/Mn21	Fe22/Mn22
P[C]cmm	(0,M_y,0)	(0,0,0)	(0,0,M_z)
P[C]nam	(M_x,0,M_z)	(0,0,M_z)	(0,0,M_z)
P[C]nmn	(0,M_y,0)	(0,M_y,0)	(M_x,M_y,0)
P[C]can	(M_x,0,M_z)	(M_x,0,0)	(M_x,M_y,0)
P[C]nan	(0,M_y,0)	(M_x,0,0)	(M_x,M_y,0)
P[C]cmn	(M_x,0,M_z)	(0,M_y,0)	(M_x,M_y,0)
P[C]cam	(0,M_y,0)	(0,0,M_z)	(0,0,M_z)
P[C]nmm	(M_x,0,M_z)	(0,0,0)	(0,0,M_z)

Table 8.2.: The resulting magnetic models and the allowed directions of the magnetic moments (based on the symmetry *Ccmm* of the nuclear structure).

The different magnetic models were refined using the Jana program[76]. The wR(obs/all) and R(obs/all) values obtained from refinements of the neutron powder diffraction data measured at different temperatures using the large wavelength bandwidth are shown in Table 8.4 and 8.3 Corresponding values obtained from refinements using the short wavelength bandwidth are shown in Tables A.15, A.14 in appendix).

R(obs/all)								
T (K)	P[C]cmm	P[C]nam	P[C]nmn	P[C]can	P[C]nan	P[C]cmn	P[C]cam	P[C]nmm
105	35.87/ 78.23	23.64/ 63.74	34.34/ 70.94	22.52/ 43.16	6.04/ 10.19	10.09/ 39.20	23.48/ 36.20	46.27/ 67.61
90	46.96/ 71.14	37.02/ 48.90	40.97/ 77.45	28.02/ 36.16	6.02/ 7.01	11.54/ 43.30	28.06/ 40.04	52.22/ 51.92
50	36.65/ 40.51	32.27/ 47.48	46.82/ 52.87	34.53/ 36.90	9.91/ 13.09	24.25/ 34.18	28.74/ 32.01	40.06/ 40.03
20	25.04/ 26.97	26.53/ 49.03	37.72/ 47.65	30.83/ 30.44	14.87/ 19.13	30.03/ 50.56	35.03/ 41.74	37.87/ 41.47

Table 8.3.: R(obs/all) factors for magnetic Bragg reflections of $Mn_3Fe_2Si_3$ based on the neutron powder data measured on POWGEN at different temperatures for a center wavelength of 2.665 Å.

The model in magnetic space group $P[C]nan$ appears to be most reasonable from the eight refined models, as it results in the best agreement factors. Figure 8.5 and

wR(obs/all)								
T (K)	P[C]cmm	P[C]nam	P[C]nmn	P[C]can	P[C]nan	P[C]cmn	P[C]cam	P[C]nmm
105	28.49/34.41	21.25/36.16	27.16/31.50	19.87/25.82	6.37/6.82	10.60/17.44	19.27/20.53	34.98/38.89
90	36.87/36.94	28.20/28.89	31.21/36.06	24.84/26.48	5.46/5.61	11.18/17.87	22.49/27.96	54.06/54.08
50	35.02/35.12	27.25/28.97	36.09/36.39	32.25/32.32	9.41/9.51	15.49/16.41	18.69/19.04	34.83/34.82
20	25.09/25.28	24.57/26.37	34.86/35.97	32.71/32.77	16.42/16.80	19.65/21.87	26.67/27.08	30.80/30.88

Table 8.4.: wR(obs/all) factors for magnetic Bragg reflections of $Mn_3Fe_2Si_3$based on the neutron powder data measured on POWGEN at different temperatures for a center wavelength of 2.665 Å.

8.6 shows the Rietveld refinement corresponding to this magnetic space group in the 2-6 Å region at 20 K and 90 K (The other temperatures can be found in Figure A.25 and A.26 in Appendix).

At $T_{AF1-AF2}$ ≈70 K <T<T_{AF2-PM} ≈120 K, the model in magnetic space group $P[C]nan$ fits the measured neutron diffraction pattern very well: almost all calculated magnetic peaks have intensities close to the observed ones, with the exception of the (010) reflection (see Figure 8.7a). The peak (010) is observed as a broad peak at 20 K and gets broader with increasing temperature until it disappears completely above temperatures higher than T_{AF2-PM} ≈120 K. The (010) peak broadening is in accordance with the diffuse appearance of this reflection in the single crystal elastic scattering maps recorded at the TOF spectrometer MERLIN 8.2.

Below $T_{AF1-AF2}$ ≈70 K, the broad peak (010) is still calculated to zero, in addition the intensities of the newly arising magnetic reflections are underestimated. In particular, the (230) which is weak, yet clearly visible has an intensity calculated to zero (see Figure 8.7b). These discrepancies indicate that the chosen magnetic model is not correct for temperatures below the $T_{AF1-AF2}$ ≈70 K transition. To improve the quality of the refinement of the neutron diffraction data at these lower temperature, we had to lower the magnetic symmetry. For this, the nuclear structure was transformed to the different maximal translationengleiche subgroups of $Ccmm$. The symmetry of the nuclear structure was still restricted to hexagonal with the help of local symmetry operators. Different models using the magnetic space groups were then derived (see Table A.3) and refined. Based on the agreement factors, the model in magnetic space group $P[C]222_1$ (derived from the $C222_1$ space group) appears to be the best of the the forty refined models (see Table A.16 and A.17 in appendix). The Rietveld refinement of this model is shown in Figure 8.8 and Figure A.27.

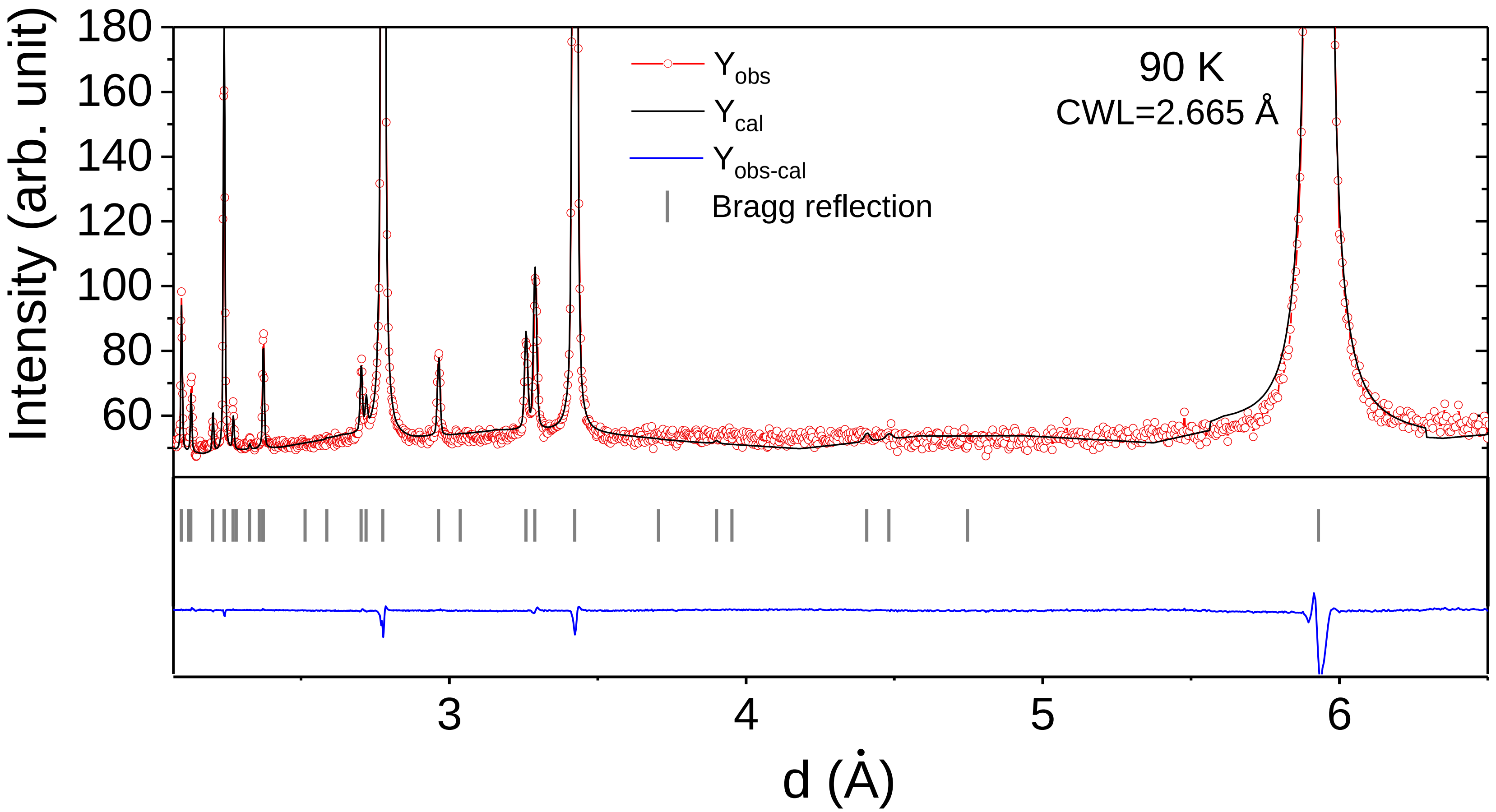

Figure 8.5.: Rietveld refinement of the $Mn_3Fe_2Si_3$ neutron powder data obtained on POWGEN in the 2-6 Å region at 90 K for a center wavelength of 2.665 Å. Gray tick marks indicate the positions of nuclear and magnetic reflections.The difference curve is shown below on the same scale. The magnetic space group model used for the fitting is $P[C]nan$

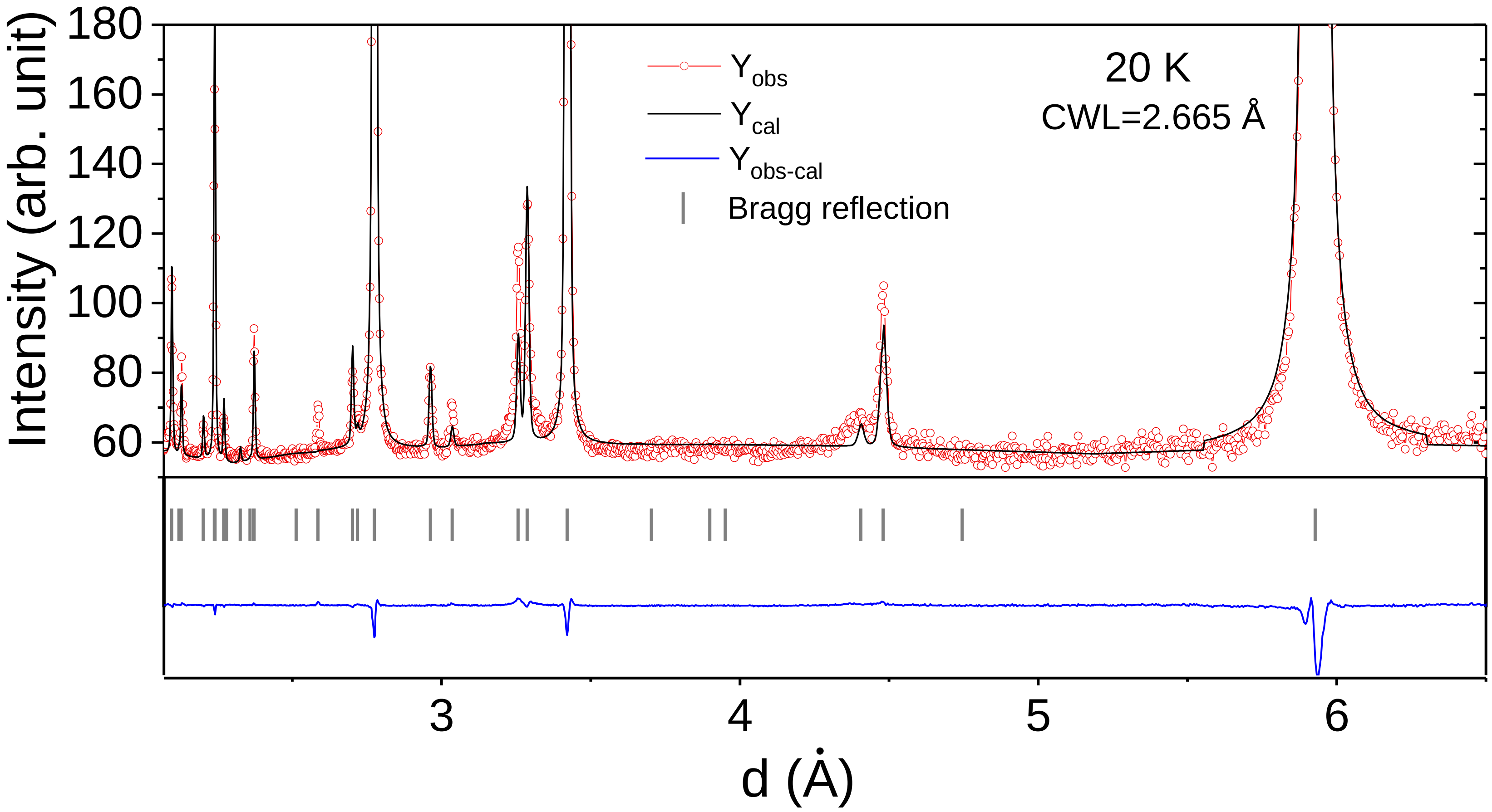

Figure 8.6.: Rietveld refinement of the Mn$_3$Fe$_2$Si$_3$ neutron powder data obtained on POWGEN in the 2-6 Å region at 20 K for a center wavelength of 2.665 Å. Gray tick marks indicate the positions of nuclear and magnetic reflections. The difference curve is shown below on the same scale. The magnetic space group model used for the fitting is $P[C]nan$

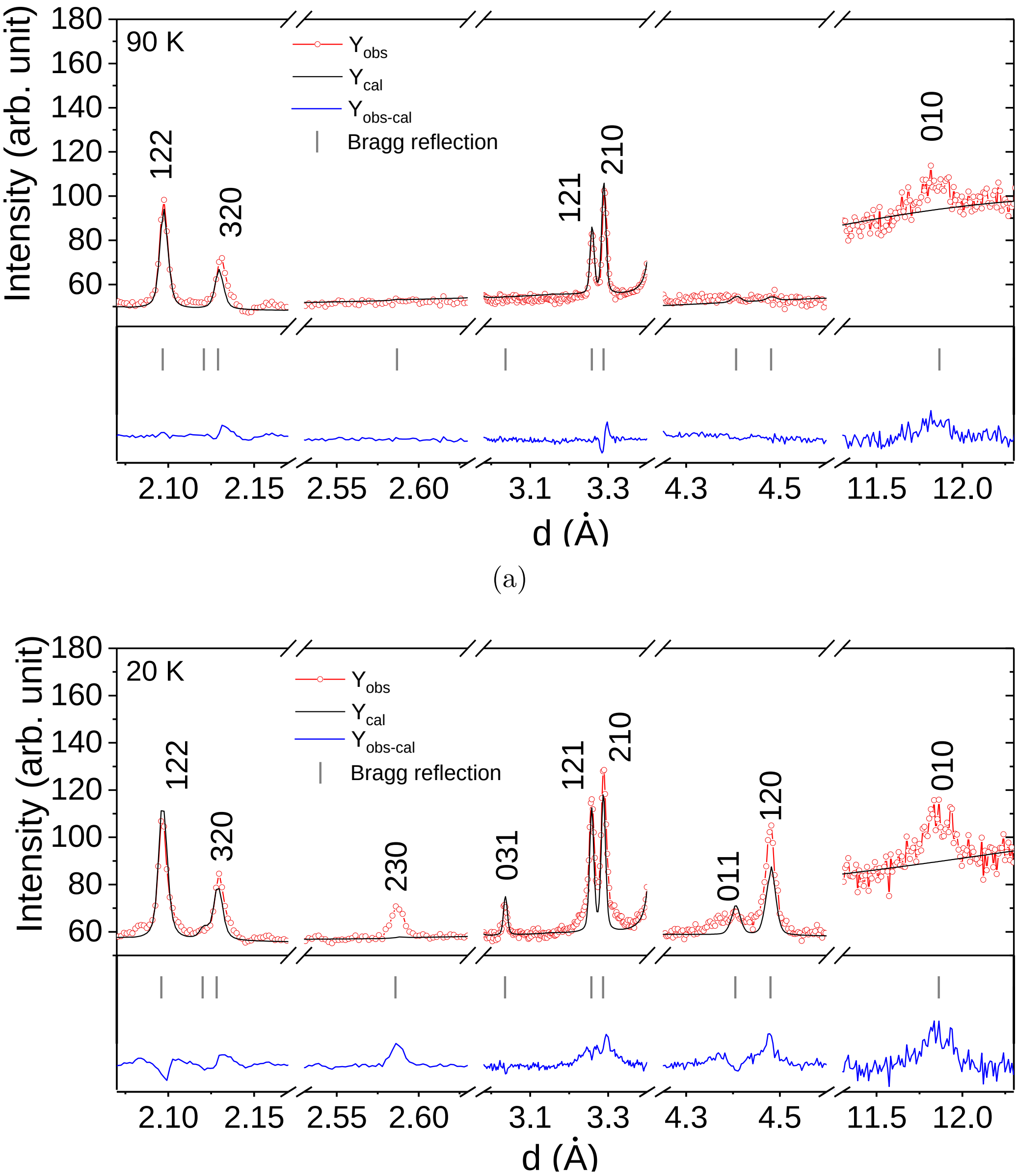

(a)

(b)

Figure 8.7.: Part of the Rietveld refinement of the $Mn_3Fe_2Si_3$ neutron powder data obtained on POWGEN at (a) 90 K and (b) 20 K for a center wavelength of 2.665 Å. Gray tick marks indicate the positions of the magnetic reflections. The difference curve is shown below on the same scale. Only the d(Å) regions with the magnetic Bragg reflections are shown. The magnetic space group model used for the fitting is $P[C]nan$.

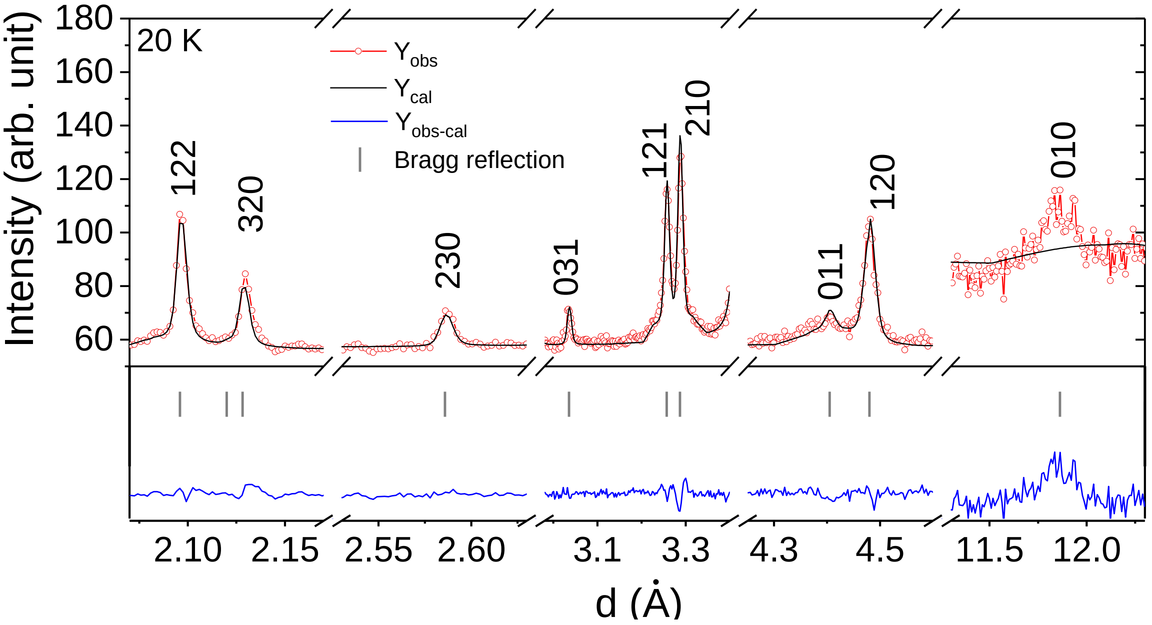

Figure 8.8.: Rietveld refinement of the $Mn_3Fe_2Si_3$ neutron powder data obtained on POWGEN at 20 K for a center wavelength of 2.665 Å. Gray tick marks indicate the positions of the magnetic reflections. The difference curve is shown below on the same scale. Only the d(Å) regions with the magnetic Bragg reflections are shown. The magnetic space group model used for the fitting is $P[C]222_1$.

8.3. Magnetic structures of $Mn_3Fe_2Si_3$

The refinement of the magnetic structures of $Mn_3Fe_2Si_3$ based on the neutron diffraction data at 105 K, 90 K, 50 K and 20 K, show two different antiferromagnetic structures in the temperature ranges that correspond to the $AF2$ ($T_{AF1-AF2} \approx 70\,K < T < T_{AF2-PM} \approx 120\,K$) and $AF1$ ($T < T_{AF1-AF2} \approx 70\,K$) phases determined by heat capacity and magnetization data (see chapter 6).

The magnetic space group $P[C]nan$, which describes the magnetic symmetry of the $AF2$ phase, allows alignment of magnetic moment along the [010] direction for Mn1/Fe1, along [100] for Fe21/Mn21 and in the a, b plane for Fe22/Mn22, respectively, while no components parallel to the c axis are allowed (see Table 8.2). The magnetic space group $P[C]222_1$ describes the symmetry of the magnetic structure of the AF1 phase. Wyckoff positions occupied by Fe1/Mn1 in $Ccmm$ split into two independent Wyckoff positions Fe11/Mn11 and Fe12/Mn12 in $C222_1$. In this magnetic space group alignment of magnetic moment along the [010] direction for Fe11/Mn11 and Fe12/Mn12 sites, along [100] for Fe21/Mn21 and components along all three directions are allowed for Fe22/Mn22. The refined components of the magnetic moments (μ_B)

along the respective directions as obtained from the Rietveld refinement using the magnetic space group $P[C]nan$ and $P[C]222_1$ are listed in Table 8.5 and 8.6.

Atom	M_x (μ_B)	M_y (μ_B)	M_z (μ_B)
105 K			
Fe1/Mn1	0	0.69(6)	0
Fe21/Mn21	0.03(30)	0	0
Fe22/Mn22	0.08(22)	-0.65(6)	0
90 K			
Fe1/Mn1	0	0.82(6)	0
Fe21/Mn21	0.01(27)	0	0
Fe22/Mn22	0.11(20)	-0.75(6)	0

Table 8.5.: Refined magnetic moments of Fe/Mn ions in the magnetic space group $P[C]nan$ for the AF2 structure at 105 and 90 K. M_x, M_y and M_z are the projections of the magnetic moment along the [100], [010] and [001].

Atom	M_x (μ_B)	M_y (μ_B)	M_z (μ_B)
50 K			
Fe11/Mn11	0	0.88(7)	0
Fe12/Mn12	0	-0.79(8)	0
Fe21/Mn21	0.01(60)	0	0
Fe22/Mn22	0.13(41)	-0.75(2)	-0.45(3)
20 K			
Fe11/Mn11	0	0.89(6)	0
Fe12/Mn12	0	-0.82(7)	0
Fe21/Mn21	0.04(50)	0	0
Fe22/Mn22	0.12(76)	-0.78(3)	-0.67(3)

Table 8.6.: Refined magnetic moments of Fe/Mn ions in the magnetic space group $P[C]222_1$ for the AF1 structure at 50 and 20 K. M_x, M_y and M_z are the projections of the magnetic moment along the [100], [010] and [001].

At 105 K and 90 K, all refined M_x components are zero within error. Taking this into account the $AF2$ structure is co-linear with all the spins aligned parallel to the *b*-axis. Both the Fe1/Mn1 and Fe22/Mn22 sites have refined magnetic moments of similar size directed parallel and antiparallel to the *b*-axis $(0.70(7)\mu_B$ and $0.66(7)\mu_B$, respectively (see Figure 8.9a). Within their standard deviations, the Fe21/Mn21 sites have no significant ordered moment. Thus of the Fe/Mn sites forming the empty octahedra, only two thirds of the sites carry an ordered moment in the $AF2$ phase. Within one octahedra, the atoms on the same height z have their spins aligned in an antiparallel way.

At 90 K, the observed magnetic ordering of the AF2 phase is very similar to the structure at 105 K (see Figure 8.9b) and only the magnitude of the refined magnetic moments on Fe1/Mn1 and Fe22/Mn22 are slightly increased, with $\approx 0.82(8)\mu_B$ and $\approx 0.76(8)\mu_B$, respectively.

At temperatures below $T_{AF1-AF2}$ ≈70 K, the magnetic structure changes from the co-linear $AF2$ (MSG: $P[C]nan$) to a non-co-linear $AF1$ phase (MSG: $P[C]222_1$).

At 50 K, (Fe11/Mn11 and Fe12/Mn12) sites, which result from the splitting of the Fe1/Mn1 site due to the lowering of the symmetry, are no longer magnetically equivalent. However, they still have refined magnetic moments of similar size directed parallel and antiparallel to the *b*-axis ($0.88(7)\mu_B$ and $0.79(8)\mu_B$, respectively (see Figure 8.10a and 8.11a). As can be seen in Table 8.6, these magnetic moments basically do not change when the temperature is lowered to 20 K (see Figure 8.10b and 8.11b). Similar to what is observed in the $AF2$ phase, the Fe21/Mn21 sites have no significant ordered moment in the $AF1$ phase.

The most significant difference between the $AF2$ and the $AF1$ phase is that the magnetic moments on the Fe22/Mn22 sites acquire a component in *c*-direction and align in the b, c-plane. It is this re-alignment of the spins on the Fe22/Mn22 sites in the *b*,*c*-plane which breaks the centrosymmetry of the magnetic structure. The spins on these sites form an angle of ≈ 30° at 50 K and ≈ 40° at 20 K with the *b* axis (see Figure 8.11a and 8.11b). The magnitude of the Fe22/Mn22 magnetic moment is $\approx 0.8(3)\mu_B$ and $\approx 1.0(5)\mu_B$ at 50 K and 20 K, respectively.

No abrupt change is observed in the Mn2-Mn2 distances at the two magnetic transitions as demonstrated by the results of the structure determination based on the synchrotron single crystal diffraction data and they decrease quite smoothly in the whole measured temperature range (see Figure 7.8 in chapter 7). The PM-AF2 transitions, however, is accompanied with a significant decrease in the angular distortion of the $[\square\ (Fe2/Mn2)_6]$ octahedra (see Figure 7.10).

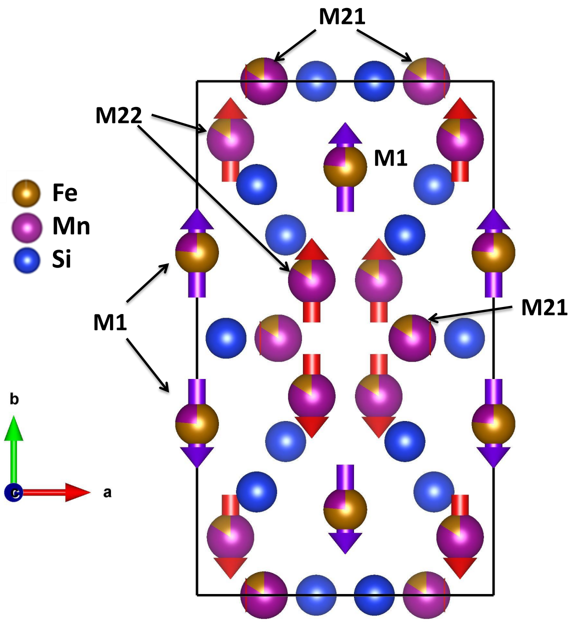

(a)

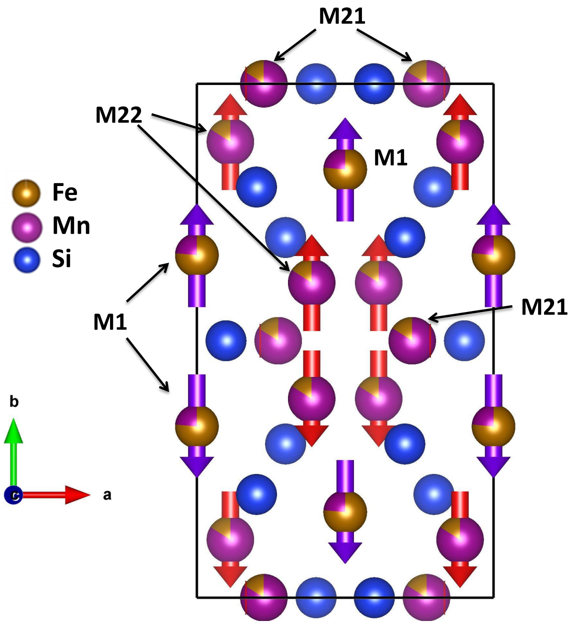

(b)

Figure 8.9.: Magnetic structure of Mn$_3$Fe$_2$Si$_3$ for magnetic space group $P[C]nan$ extracted from refinement performed on diffraction pattern taken at (a) 105 K and (b) 90 K. Note that the refined value of M_x for Fe21/Mn21 and Fe22/Mn22 is smaller than its respective standard deviation. For the drawing, this value was therefore set to zero.

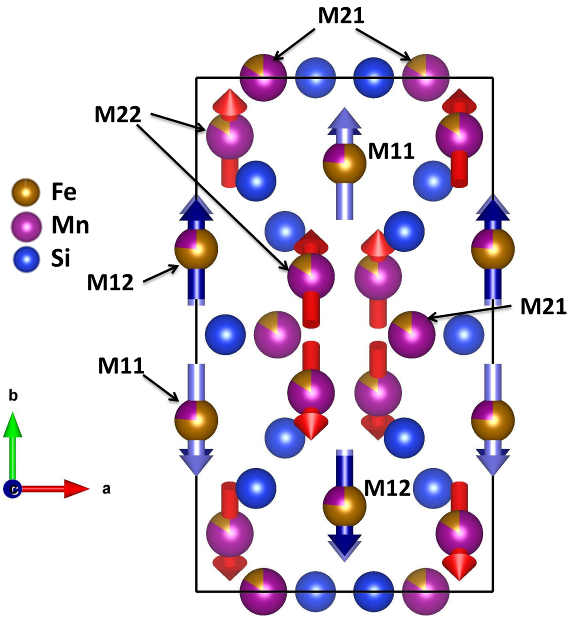

(a)

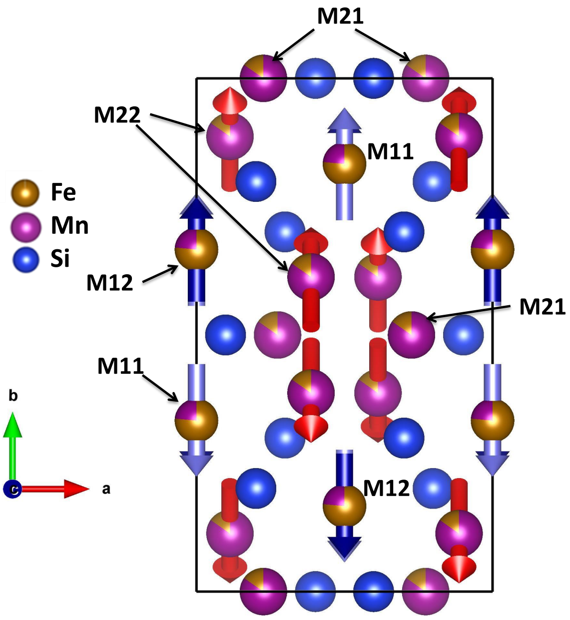

(b)

Figure 8.10.: Magnetic structure of $Mn_3Fe_2Si_3$ for magnetic space group $P[C]222_1$ extracted from refinement performed on diffraction pattern taken at (a) 50 K and (b) 20 K. Note that the refined value of M_x for Fe21/Mn21 and Fe22/Mn22 is basically identical to its standard deviation. For the drawing, this value was therefore set to zero.

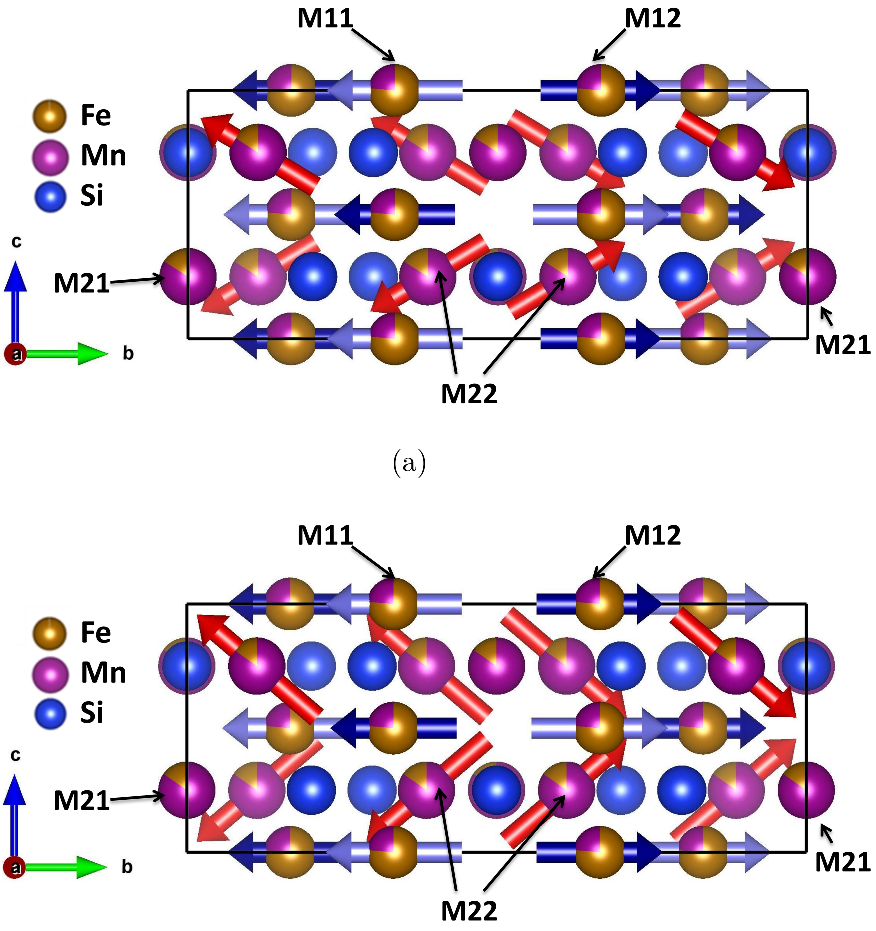

(a)

(b)

Figure 8.11.: Projection along a-direction of $Mn_3Fe_2Si_3$ magnetic structure for magnetic space group $P[C]222_1$ extracted from refinement performed on diffraction pattern taken at (a) 50 K and (b) 20 K. Note that the refined value of M_x for Fe21/Mn21 and Fe22/Mn22 is basically identical to its standard deviation. For the drawing, this value was therefore set to zero.

8.4. Comparison to other magnetic structures in the system $Mn_{5-x}Fe_xSi_3$

Within the $Mn_{5-x}Fe_xSi_3$ system, the Mn-rich compounds exhibit antiferromagnetic (AF) order at temperatures below 125 K, while the Fe-rich compounds show predominantly ferromagnetic (FM) order at comparably high temperature [4]. Up to now, only the magnetic structures of $MnFe_4Si_3$ and Mn_5Si_3 have been characterized in detail.

The compound $MnFe_4Si_3$ with $x = 4$ has a ferromagnetic structure where only the sites with mixed occupancy of Fe/Mn (M2) carry an ordered magnetic moment aligned in the a, b plane of approximately $1.5(2)\mu_B$ [3]. At the temperature of magnetic ordering the interatomic distances between the M2 atoms are increased, which in turn leads to a significant increase of the a lattice parameter and an increase in the volumetric thermal expansion $\alpha(T)$ (see Figure 7.11 in Chapter 7). As for the sites (M1), the refined moment was smaller than the standard deviation [3].

As for the compound Mn_5Si_3 with $x = 0$, it exhibits a structural phase transition from hexagonal to orthorhombic which coincides with the $PM - AF2$ transition [2, 22]. In the $AF2$ phase, the magnetic moments on the M22 position point almost antiparallel to each other along the b-axis and are slightly tilted away from the b-axis down to 60 K [2].

The magnitude of the magnetic moments on the M22 at 90 K is $1.48(1)\,\mu_B$ and it is slightly reduced with decreasing temperature. Neither the M1 and M21 sites carry an ordered magnetic moment in this phase [2, 22].

In $Mn_3Fe_2Si_3$ both sites M1 and M2 (orthohexagonal setting: M21 and M22) have mixed occupancy of Fe/Mn, where Fe preferentially occupies the M1 site and Mn is mainly incorporated in the M2 site. The structural phase transition to an orthorhombic phase is not observed in the studied temperature range. In the $AF2$ phase of $Mn_3Fe_2Si_3$ the spins on the M22 atoms are aligned parallel to b, yet the magnetic moments are smaller ($\approx 0.76(8)\mu_B$) than in the $AF2$ phase of Mn_5Si_3. In difference to the $AF2$ phase of Mn_5Si_3, the M1 sites of $Mn_3Fe_2Si_3$ have an ordered moment of $\approx 0.82(8)\mu_B$ that is also directed along b.

The magnetic structure of Mn_5Si_3 in the low temperature $AF1$ phase is characterized by a monoclinic spin arrangement, where the moments on the M22 sites with $\mu \approx 2.9\mu_B$ form a complex non-collinear structure [23], while there is still no ordered moment observed on the M21 site. M1 carries a smaller magnetic moment, which is approximately parallel to the vector sum of the moments on the four neighbouring M22 sites [23]. The $AF1$ phase of $Mn_3Fe_2Si_3$ is characterized by an orthorhombic spin arrangement, with no ordered moment on the M21 site. In $Mn_3Fe_2Si_3$, the M1 (M11 and M12) moments align parallel and antiparallel along the b-axis with similar size of about $\approx 0.8\mu_B$. At the $AF2 - AF1$ transition, the spins on the M22 sites of $Mn_3Fe_2Si_3$ are canted from the b-direction and oriented in the b, c-plane with a magnitude of $\approx 1.0(5)\mu_B$, resulting in a non-colinear antiferromagnetic structure in the $AF1$ phase (see Figure 8.11a and 8.11b).

It has been found that the stability of an ordered magnetic moment on manganese atoms in a variety of intermetallic compounds such as Laves phases is related to the interatomic distances between Mn atoms which are influenced by thermal expansion, chemical substitution and pressure [78, 77]. The studies on Laves phases indicate that below a critical distance between Mn atoms ≈ 2.67 Å, the Mn atoms do no longer develop a static ordered magnetic moment [78, 79].

The appearance of an ordered moment on the M1 site in the $AF1$ phase of Mn_5Si_3 is an example of a similar effect as the one observed in Laves phases, where, the ordering on M1 site is accompanied with an increase of the volumetric thermal expansion $\alpha(T)$ at the $AF2 - AF1$ transition (see Figure 7.11 in Chapter 7), which leads to an increase in the M1-M1 distance ($d_{M1-M1}=c/2=2.41$Å) [23]. This also could be related to the sudden change in the bond length distortion of the [(M1)Si_6] octahedra at the temperature of the $AF2 - AF1$ transition (see Figure in chapter 7).

In difference to this, all magnetic moment in $Mn_3Fe_2Si_3$ are stable in both phases, the change in volumetric thermal expansion $\alpha(T)$ looks less striking with only a slight increase at the $AF1$-$AF2$ transition (see Figure 7.7 in Chapter 7) and there is no significant sign of a bond length distortion in the [(M1)Si_6] and [□ $(M2)_6$] octahedra at all measured temperatures. However, all three compounds $Mn_{5-x}Fe_xSi_3$ (x=0, 2, 4) show an angular distortion variation at PM-$AF2$ which is significant in the [□ $(M2)_6$] octahedra when compared to the [(M1)Si_6] octahedra (see Figure 7.15 in chapter 7). In particular, a sudden decrease in angular distortion in the [□ $(M2)_6$] octahedra at the PM to $AF2$ transition in $Mn_3Fe_2Si_3$ is noteworthy. In Mn_5Si_3 the angular distortion of both octahedra is clearly changing at the $AF2 - AF1$ transition.

Similar to the Mn based Laves compounds, the Fe based Laves compounds show a dependence of the Fe magnetic moment formation on the Fe–Fe distance [80]. As the atomic radius of Fe is smaller than Mn, the critical distance for Fe is as well smaller [81, 82, 78].

This suggest that the stability of the ordered magnetic moment on the M1 site of $Mn_3Fe_2Si_3$ in the $AF2$ and $AF1$ phase is due to the fact that the interatomic separation between M1-M1 atoms (d_{M1-M1} ≈2.368Å) is already above the critical value d^C_{Fe-Fe} in both phases (see Table A.12 in appendix). The effect is related to the overall shrinkage of the unit cell resulting from the substitution of the smaller Fe on the M1 site. According to a study done on several groups of Fe compounds in the Laves phase [80], it has been found that the Fe magnetic moment decreases with the reduction of the Fe-Fe distance. This might be related to the fact that the refined magnetic moment on M1 site of $MnFe_4Si_3$ [3] is tiny, as here the M1-M1 distance is further reduced ($d^{x=4}_{M1-M1}$ ≈2.359(2)Å) due to the complete substitution of Mn with Fe on the M1 site.

9. Summary

$Mn_3Fe_2Si_3$ crystallizes in hexagonal space group $P6_3/mcm$ at all temperatures down to 5 K and a structural transition to an orthorhombic phase, which occurs in the parent compound Mn_5Si_3 [22, 2], was not observed. Two symmetrically independent sites with significantly different chemical surroundings exist for the paramagnetic ions, the M1(WP:4d) and the M2(WP:6g) sites, respectively. Fe preferentially occupies the M1(WP:4d) site and is octahedrally coordinated by Si, while Mn is mainly incorporated on the M2(WP:6g) site and forms the corners of en empty octahedron. As the atomic radius of Fe (r(Fe)=156 pm) is smaller than Mn (r(Mn)=161 pm) [74], the incorporation of Fe leads to an overall shrinkage of the $Mn_3Fe_2Si_3$ unit cell and a decrease of its interatomic distances when compared to the parent compound Mn_5Si_3 [2].

$Mn_3Fe_2Si_3$ undergoes a sequence of magnetic phase transitions from a paramagnetic PM phase to two distinct antiferromagnetic phases $AF2$ and $AF1$ with decreasing temperature. Based on the refinement of neutron powder data, the $AF2$ magnetic structure was determined to be co-linear with the spins on the M1 sites and on two thirds of the M2 sites aligned parallel and antiparallel to the b-axis. The refined magnetic moments on the two sites are of similar size. For the remaining one third of the M2 sites, no significant ordered magnetic moment was determined from the neutron powder data.

At the $AF2 - AF1$ transition the magnetic structure changes from the centrosymmetric co-linear $AF2$ phase to the non-co-linear, non-centrosymmetric $AF1$ phase. The most significant difference between the $AF2$ and the $AF1$ phase is that the spins on the M2 sites which carry an ordered magnetic moment acquire a component in the c-direction and re-align in the b, c-plane. This re-alignment of the spins breaks the centrosymmetry of the magnetic structure.

The ordered magnetic moment on the M1 site is stable in both the $AF1$ and $AF2$ phase, in contrast to what is observed for the parent compound Mn_5Si_3, where the ordered moment on the M1 site only appears in the $AF1$ phase. The appearance of this ordered moment in Mn_5Si_3 has been attributed to the fact that the critical M1-M1 distance, which was given as ($d_{M1-M1}=c/2=2.41$Å)[23], has been exceeded.

In $Mn_3Fe_2Si_3$ the preferential substitution of Mn with Fe leads evidently to a reduction of the critical distance for the formation of an ordered moment on the $4d$ site and allows an ordered moment on this site already in the $AF2$ phase.

Different from the phase diagram for the series published by Songlin *et al.* [4] based on powder data, our macroscopic measurements on single crystalline $Mn_3Fe_2Si_3$ show an increased transition temperature not only for the $AF2$ to PM, but also for the $AF1$ to $AF2$ transition. Comparing the macroscopic response of $Mn_3Fe_2Si_3$

and Mn_5Si_3, we note the missing strong increase of the magnetization at high field found in Mn_5Si_3 [25]. Based on the comparison of the magnetic structures in both compounds, we attribute this increase in Mn_5Si_3 to the loss of AF order on the 4d site when undergoing the transition from $AF1$ to $AF2$.

For $Mn_3Fe_2Si_3$ the ratio $|f| = \frac{|\theta_{CW}|}{T_N}$, was calculated to be much less than one. This can be explained within the mean field approximation for two sublattices with FM intra-sublattice interaction. On the other hand the increased response of the low field $\frac{M}{B}$, in particular for the field applied perpendicular to [001] direction above the ordering temperature at 120 K, can be interpreted as a trace of FM order, which develops towards the Fe rich side of the phase diagram [4].

Like the end member Mn_5Si_3 [4], $Mn_3Fe_2Si_3$ features an inverse MCE. However, the size of the effect is significantly reduced compared to Mn_5Si_3. For comparable field changes the entropy change is reduced by a factor ~10 [4]. We attribute the much smaller gain in entropy through the transition to the persistent order on the M1 site in $Mn_3Fe_2Si_3$, which does not contribute to the magnetic entropy change. We conclude therefore, that in particular the M1 site moments contribute to the strong inverse MCE observed in Mn_5Si_3 [4].

Bibliography

1. V. Franco et al. "The Magnetocaloric Effect and Magnetic Refrigeration Near Room Temperature: Materials and Models". In: *Annual Review of Materials Research* 42.1 (2012), pp. 305–342.

2. M. Gottschilch et al. "Study of the antiferromagnetism of Mn_5Si_3: an inverse magnetocaloric effect material". In: *Journal of Materials Chemistry* 22 (2012), pp. 15275–15284.

3. P. Hering et al. "Structure, Magnetism, and the Magnetocaloric Effect of $MnFe_4Si_3$ Single Crystals and Powder Samples". In: *Chemistry of Materials* 27.20 (2015), pp. 7128–7136.

4. Songlin et al. "Magnetic phase transition and magnetocaloric effect in $Mn_{5-x}Fe_xSi_3$". In: *Journal of Alloys and Compounds* 334 (2002), pp. 249–252.

5. O. Tegus et al. "Magnetic-phase transitions and magnetocaloric effects". In: *Physica B: Condensed Matter* 319.1 (2002), pp. 174–192.

6. N. Biniskos et al. "Spin dynamics of the magnetocaloric compound $MnFe_4Si_3$". In: *Physical Review B* 96 (2017), p. 104407.

7. N. Biniskos et al. "Spin Fluctuations Drive the Inverse Magnetocaloric Effect in Mn_5Si_3". In: *Phys. Rev. Lett.* 120 (25 2018), p. 257205.

8. F. J.dos Santos et al. "Spin waves in the collinear antiferromagnetic phase of Mn_5Si_3". In: *Phys. Rev. B* 103 (2 2021), p. 024407.

9. E. Warburg. "Magnetische Untersuchungen". In: *Annalen der Physik* 249.5 (1881), pp. 141–164.

10. A. Smith. "Who discovered the magnetocaloric effect?" In: *The European Physical Journal H* 38.4 (2013), pp. 507–517.

11. P. Weiss and A. Piccard. "Le phénomène magnétocalorique". In: *Journal de Physique Théorique et Appliquée* 7.1 (1917), pp. 103–109.

12. W. F. Giauque and D. P. MacDougall. "Attainment of Temperatures Below 1 ° Absolute by Demagnetization of $Gd_2(SO_4)_3{\cdot}8H_2O$". In: *Physical Review* 43 (1933), pp. 768–768.

13. G. V. Brown. "Magnetic heat pumping near room temperature". In: *Journal of Applied Physics* 47.8 (1976), pp. 3673–3680.

14. V. K. Pecharsky and Jr. K. A. Gschneidner. "Giant Magnetocaloric Effect in $Gd_5(Si_2Ge_2)$". In: *Physical Review Letters* 78.23 (1997), pp. 4494–4497.

15. Ekkes Brück. "Developments in magnetocaloric refrigeration". In: *Journal of Physics D: Applied Physics* 38.23 (2005), R381–R391.

16. A. Fujita et al. "Itinerant-electron metamagnetic transition and large magnetocaloric effects in $La(Fe_xSi_{1-x})_{13}$ compounds and their hydrides". In: *Physical Review B* 67.10 (2003), p. 104416.

17. J. Lyubina et al. "Multiple Metamagnetic Transitions in the Magnetic Refrigerant $La(Fe,Si)_{13}H$". In: *Physical Review Letters* 101.17 (2008), p. 177203.

18. G. Li et al. "Thermodynamic-state and kinetic-process dependent dual ferromagnetic states in high-Si content FeMn(PSi) alloys". In: *Journal of Applied Physics* 118.21 (2015), p. 213903.

19. H. Zong. "Magnetic Characterization of Powder Samples from the Magnetocaloric compound Series $Mn_{5-x}Fe_xSi_3$". Bachelor's Thesis. Aachen university of applied sciences: Fachhochschule Aachen, 2016.

20. H. Bińczycka et al. "Atomic and magnetic structure of $Mn_{5-x}Fe_xSi_3$". In: *physica status solidi (a)* 19.1 (1973), K13–K17.

21. A. Eich et al. "Magnetocaloric Mn_5Si_3 and $MnFe_4Si_3$ at variable pressure and temperature". In: *Materials Research Express* 6.9 (2019), p. 096118.

22. P. J. Brown and J. B. Forsyth. "Antiferromagnetism in Mn_5Si_3: the magnetic structure of the AF2 phase at 70 K". In: *Journal of Physics: Condensed Matter* 7.39 (1995), pp. 7619–7628.

23. P. J. Brown et al. "The low-temperature antiferromagnetic structure of Mn_5Si_3 revised in the light of neutron polarimetry". In: *Journal of Physics: Condensed Matter* 4.49 (1992), pp. 10025–10036.

24. C. Sürgers et al. "Switching of a large anomalous Hall effect between metamagnetic phases of a non-collinear antiferromagnet". In: *Scientific Reports* 7.1 (2017), Art.Nr.: 42982.

25. S. C. Das et al. "Observation of inverted hysteresis loop and thermomagnetic irreversibility in the antiferromagnetic Mn_5Si_3 alloy". In: *Physical Review B* 100.2 (2019), p. 024409.

26. K. M. Krishnan. *Fundamentals and Applications of Magnetic Materials*. Oxford Scholarship Online, 2016. ISBN: 9780199570447.

27. C. Kittel. *Introduction to Solid State Physics, 8th Edition.* John Wiley & Sons Inc, 2004. ISBN: 978-0-471-41526-8.

28. A. Haug. *Theoretical Solid State Physics.* Ed. by Albert Haug. Vol. 2. Pergamon, 1972. ISBN: 9781483159799.

29. P. W. Anderson. “Generalizations of the Weiss Molecular Field Theory of Antiferromagnetism”. In: *Physical Review* 79 (1950), pp. 705–710.

30. S. Blundell. *Magnetism in Condensed Matter.* Oxford University Press, Aug. 1, 2001. ISBN: 9780198505914.

31. J. I. Hoppe. “Effective magnetic moment”. In: *Journal of Chemical Education* 49.7 (1972).

32. S. de Brion et al. “Magnetic and electric properties of $La_{1-\delta}MnO_3$”. In: *Physical Review B* 59.2 (1999), pp. 1304–1310.

33. H. Ibach and H. Lüth. *Solid-State Physics-An Introduction to Principles of Materials Science.* Ed. by Springer. 4th ed. 2009. ISBN: 978-3-540-93804-0.

34. D.G. Westlake. “Hydrides of intermetallic compounds: A review of stabilities, stoichiometries and preferred hydrogen sites”. In: *Journal of the Less Common Metals* 91.1 (1983), pp. 1–20.

35. W. H. Bragg et al. *The crystalline state.* Ed. by Macmillan New York. 1934.

36. C. Hammond. *The Basics of Crystallography and Diffraction.* Ed. by Oxford. 4th ed. 2015. ISBN: 9780198738671.

37. W. Massa. *Crystal Structure Determination.* Springer, 2000. ISBN: 978-3-540-65970-9.

38. R. X. Fischer and E. Tillmanns. “The equivalent isotropic displacement factor”. In: *Acta Crystallographica Section C* 44.4 (1988), pp. 775–776.

39. K. N. Trueblood et al. “Atomic Dispacement Parameter Nomenclature. Report of a Subcommittee on Atomic Displacement Parameter Nomenclature”. In: *Acta Crystallographica Section A* 52.5 (1996), pp. 770–781.

40. E. N. Maslen. “X-ray absorption”. In: *International Tables for Crystallography.* International Union of Crystallography, 2006, pp. 599–608.

41. J. de Meulenaer and H. Tompa. “The absorption correction in crystal structure analysis”. In: *Acta Crystallographica* 19.6 (1965), pp. 1014–1018.

42. T.Brückel. *JCNS Neutron Lab Course.* Ed. by T.Brückel et al. Vol. 28. Forschungszentrum Jülich GmbH, JCNS / RWTH Aachen / Univ.Münster, 2005, pp. 3.1–3.28. ISBN: 3-89336-395-5.

43. T.Brückel. *JCNS Neutron Lab Course.* Ed. by T.Brückel et al. Vol. 106. Forschungszentrum Jülich GmbH, JCNS / RWTH Aachen / Univ.Münster, 2015, pp. 1.1–1.12. ISBN: 978-3-95806-055-5.

44. A. Furrer, T. Strässle, and J. Mesot. *Neutron Scattering in Condensed Matter Physics.* Ed. by Singapore Hackensack NJ : World Scientific. Vol. 4. Series on neutron techniques and applications. 2009. ISBN: 978-981-4280-92-1.

45. G. Heger. *JCNS Neutron Lab Course.* Ed. by T.Brückel et al. Vol. 28. Forschungszentrum Jülich GmbH, JCNS / RWTH Aachen / Univ.Münster, 2005, pp. 12.1–12.13. ISBN: 3-89336-395-5.

46. J. Rodríguez-Carvajal and J. Villain. "Magnetic structures". In: *Comptes Rendus Physique* 20.7 (2019), pp. 770–802.

47. Garam Park et al. "Magnetic Structure of Inorganic-Organic Hybrid (C6H5CH2CH2NH3)2Mn
Using Magnetic Space Group Concept". In: *Symmetry* 12.12 (2020), p. 1980.

48. J. Rodríguez-Carvajal and F. Bourée. "Symmetry and magnetic structures". In: *EPJ Web of Conferences* 22 (2012), p. 00010.

49. A.V. Shubnikov, N.V. Belov, et al. *Colored symmetry, by A.V. Shubnikov, N.V. Belov, and others. Translated from the Russian by Jack Itzkoff and Jack Gollob. Edited by William T. Holser.* eng. New York: Macmillan, 1964.

50. A. P. Cracknell. "Group theory and magnetic phenomena in solids". In: *Reports on Progress in Physics* 32.2 (1969), pp. 633–707.

51. "International Tables for Crystallography". In: (2006). Ed. by Th. Hahn.

52. M.Beyss and H.Gier. *Schmelzverfahren fur die Herstellung von Reinstmaterialien.* Poster. Forschungszentrum Jülich GmbH., 2014.

53. A. Jouan et al. "Multiple applications of cold crucible melting". In: *Radwaste Magazine* 3(2) (1996), pp. 77–81.

54. J. Czochralski. "A new method for the measurement of the crystallization rate of metals". In: *Zeitschrift für Physikalische Chemie* 92 (1918), pp. 219–221.

55. Quantum Design. *Physical Property Measurement System-Heat Capacity Option User's Manual.* 11th edition. Quantum Design. 11578 Sorrento Valley Rd. San Diego, CA 92121-1311 USA, 2004.

56. J.C. Lashley et al. "Critical examination of heat capacity measurements made on a Quantum Design physical property measurement system". In: *Cryogenics* 43.6 (2003), pp. 369–378.

57. A. B. Greilinger. “A Back-Reflection Laue Method for determining Crystal Orientation”. In: *Zeitschrift für Kristallographie - Crystalline Materials* 91 (1935), pp. 424–432.

58. Multiwire Laboratories. *MWL120 Real-Time, Back-Reflection Laue Camera System.* Multiwire Laboratories, Ltd. Cornell Business and Technology Park 95 Brown Road, MS 1018 266A Langmuir Building Ithaca, NY 14850 USA, 2013.

59. DESY Photon Science. *PETRA III Extension Project, Beamline P24-Chemical Crystallography.* Tech. rep. DESY Photon Science, FS-PEX and University Hamburg, Mineralogy Department, 2014.

60. Helmholtz-Zentrum Berlin für Materialien und Energie. “E4: The 2-Axis Diractometer at BER II”. In: *Journal of large-scale research facilities* 3 (2017), A104.

61. R.I. Bewley et al. “MERLIN, a new high count rate spectrometer at ISIS”. In: *Physica B: Condensed Matter* 385-386 (2006), pp. 1029–1031.

62. A. Huq et al. “Powgen: A third-generation high-resolution high-throughput powder diffraction instrument at the spallation neutron source”. In: *zeitschrift für kristallographie* 1 (2011), pp. 127–135.

63. Ashfia Huq et al. “POWGEN: rebuild of a third-generation powder diffractometer at the Spallation Neutron Source”. In: *Journal of Applied Crystallography* 52.5 (2019), pp. 1189–1201.

64. R.A. Ewings et al. “Horace: Software for the analysis of data from single crystal spectroscopy experiments at time-of-flight neutron instruments”. In: *Nuclear Instruments and Methods in Physics Research Section A: Accelerators, Spectrometers, Detectors and Associated Equipment* 834 (2016), pp. 132–142.

65. N. Maraytta. “Structure and Dynamics of Magnetocaloric Materials”. PhD thesis. JCNS-2 / PGI-4: Forschungszentrum Jülich GmbH/RWTH Aachen, 2021.

66. M. Herlitschke et al. “Elasticity and magnetocaloric effect in $MnFe_4Si_3$”. In: *Physical Review B* 93.9 (2016).

67. N. Abboushi. “Magnetocaloric materials”. 2021.

68. F.Q. Zhao et al. “Magnetic-entropy change in $Mn_5Ge_{3-x}Si_x$ alloys”. In: *Journal of Alloys and Compounds* 416.1-2 (2006), pp. 43–45.

69. D.M. Rajkumar et al. “Magnetocaloric effect in high-energy ball-milled $Gd_5Si_2Ge_2$ and $Gd_5Si_2Ge_2$/Fe nanopowders”. In: *Journal of Magnetism and Magnetic Materials* 320.8 (2008), pp. 1479–1484.

70. T. Balić-Žunić and I. Vicković. “IVTON : a program for the calculation of geometrical aspects of crystal structures and some crystal chemical applications”. In: *Journal of Applied Crystallography* 29.3 (1996), pp. 305–306.

71. M. G. B. Drew et al. “Geometric control of manganese redox state”. In: *Journal of the Chemical Society, Chemical Communications* 10 (1995), p. 1035.

72. R. Ketkaew et al. *OctaDist: A tool for calculating distortion parameters in coordination complexes.* 2019. URL: `https://octadist.github.io`.

73. Y. Fei. “Thermal Expansion”. In: *Mineral Physics & Crystallography.* American Geophysical Union (AGU), 1995, pp. 29–44. ISBN: 9781118668191.

74. E. Clementi, D. L. Raimondi, and W. P. Reinhardt. “Atomic Screening Constants from SCF Functions. II. Atoms with 37 to 86 Electrons”. In: *The Journal of Chemical Physics* 47.4 (1967), pp. 1300–1307.

75. M. R. Silva, P. J. Brown, and J. B. Forsyth. “Magnetic moments and magnetic site susceptibilities in Mn_5Si_3”. In: *Journal of Physics: Condensed Matter* 14.37 (2002), pp. 8707–8713.

76. V. Petříček, M. Dušek, and L. Palatinus. “Crystallographic Computing System JANA2006: General features”. In: *Zeitschrift für Kristallographie - Crystalline Materials* 229.5 (2014), pp. 345–352.

77. M. Shiga. “Magnetism and spin fluctuations of laves phase manganese compounds”. In: *Physica B+C* 149.1 (1988), pp. 293–305.

78. H. Wada et al. “Stability of Mn moments and spin fluctuations in RMn_2 (R: Rare earth)”. In: *Journal of Magnetism and Magnetic Materials* 70.1 (1987), pp. 134–136.

79. C. Ritte, R. Cywinski, and S. H. Kilcoyne. “The Nature of the Mn Moment in Laves Phase Compounds: Evolution of the Magnetic Order in $Ho_{1-x}Y_xMn_2$”. In: *Zeitschrift für Naturforschung A* 50.2-3 (1995), pp. 191–198.

80. K. Kai and T. Nakamichi. “Magnetic Moment of the Iron Atom in the Laves Phase Compounds”. In: *Journal of the Physical Society of Japan* 30.6 (1971), pp. 1755–1755.

81. R. Lübbers, G. Wortmann, and H. F. Grünsteudel. In: *Hyperfine Interactions* 123/124.1/4 (1999), pp. 529–559.

82. R. Lübbers, K. Rupprecht, and G.Wortmann. In: *Hyperfine Interactions* 128.1/3 (2000), pp. 115–135.

83. A. C. Larson and R. B. Von Dreele. *General Structure Analysis System (GSAS).* LAUR 86-748. Los Alamos National Laboratory Report LAUR. 2004.

84. J. Rodríguez-Carvajal. *An introduction to the program FullProf 2000.* 2001st ed. Laboratoire Léon Brillouin (CEA-CNRS). CEA/Saclay, 91191 Gif sur Yvette Cedex, FRANCE, 2001.

85. J.-F. Bérar and G. Baldinozzi. “Modeling of line-shape asymmetry in powder diffraction”. In: *Journal of Applied Crystallography* 26.1 (1993), pp. 128–129.

86. H. M. Rietveld. “Line profiles of neutron powder-diffraction peaks for structure refinement”. In: *Acta Crystallographica* 22.1 (1967), pp. 151–152.

87. H. M. Rietveld. “A profile refinement method for nuclear and magnetic structures”. In: *Journal of Applied Crystallography* 2.2 (1969), pp. 65–71.

88. L. B. McCusker et al. “Rietveld refinement guidelines”. In: *Journal of Applied Crystallography* 32 (1999), pp. 36–50.

89. Rigaku Oxford Diffraction. *CrysAlisPro Software System, Version 1.171. 38.41 l, Rigaku Coorporation.* 2015.

90. M. S. Weiss and R. Hilgenfeld. “On the use of the merging R factor as a quality indicator for X-ray data”. In: *Journal of Applied Crystallography* 30.2 (1997), pp. 203–205.

91. K. Friese et al. “Refinement of high pressure single-crystal diffraction data using Jana2006”. In: *High Pressure Research* 33.1 (2013), pp. 196–201.

92. V. Petříček and M. Dušek. *Jana 98, The crystallographic computing system.* Institute of Physics Academy of Sciences of the Czech Republic. Praha, 2000.

93. J.M. Perez-Mato et al. “Symmetry-Based Computational Tools for Magnetic Crystallography”. In: *Annual Review of Materials Research* 45.1 (2015), pp. 217–248.

94. D. Richard, M. Ferrand, and G.J. Kearley. “Analysis and Visualisation of Neutron-Scattering Data”. In: *Journal of Neutron Research* 4 (1996), pp. 33–39.

95. M. Bouvier, P. Lethuillier, and D. Schmitt. “Specific heat in some gadolinium compounds. I. Experimental”. In: *Physical Review B* 43.16 (1991), pp. 13137–13144.

96. R. L. Carlin and A. J. van Duyneveldt. *Magnetic Properties of Transition Metal Compounds.* Ed. by Springer-Verlag Berlin Heidelberg. Vol. 2. Springer Berlin Heidelberg, 1977. ISBN: 978-3-642-87392-8.

97. A. Candini et al. “Revised magnetic phase diagram for $Fe_xMn_{5-x}Si_3$ intermetallics”. In: *Journal of Applied Physics* 95.11 (2004), pp. 6819–6821.

98. Quantum Design. *PPMS Vibrating Sample Magnetometer Application Note.* Tech. rep. Rev 05.09. Quantum Design, 2019.

99. Quantum Design. *PPMS Resistivity Option User’s Manual.* Second edition. Quantum Design. 11578 Sorrento Valley Rd. San Diego, CA 92121-1311 USA, 1999.

100. K. K. Kelley and E. G. King. “Contribution to the Data on Theoretical Metallurgy: Part 14. Entropies of the elements and inorganic compounds.” In: *U.S. Bureau of Mines.* Bulletin 592 (1961).

101. E. Makovicky and T. Balic-Zunic. “New Measure of Distortion for Coordination Polyhedra”. In: *Acta Crystallographica Section B* 54.6 (1998), pp. 766–773.

102. C. Ritter et al. “Intrinsic and induced Mn moments in $Dy_{1-x}Y_xMn_2$”. In: *Phys. Rev. B* 50 (1994), pp. 9894–9905.

103. C. Sürgers et al. “Large topological Hall effect in the non-collinear phase of an antiferromagnet”. In: *Nature Communications* 5.1 (2014), Art.Nr. 3400.

104. A. Tari. *The Specific Heat of Matter at Low Temperatures.* Ed. by Imperical College Press. 2003. ISBN: 1-86094-314-4.

105. O. Tegus et al. “Transition-metal-based magnetic refrigerants for room-temperature applications”. In: *Nature* 415 (2002), pp. 150–152.

106. C. Mayer, S. Miraglia, and S. Gorsse. “Matériaux magnétocaloriques”. In: *Techniques de l’ingénieur Propriétés électriques et électrochimiques* base documentaire : TIB336DUO.ref. article : k733 (2017).

107. G. Wang. “Magnetic and Calorimetric Study of the Magnetocaloric Effect in Intermetallics Exhibiting First-order Magnetostructural Transitions”. PhD thesis. Universidad de Zaragoza: Física de la Materia Condensada, 2012.

108. V. Franco. “application note Determination of the Magnetic Entropy Change from Magnetic Measurements : the Importance of the Measurement Protocol”. In: 2015.

109. H. Neves Bez et al. “Best practices in evaluation of the magnetocaloric effect from bulk magnetization measurements”. In: *Journal of Magnetism and Magnetic Materials* 458 (2018), pp. 301–309.

110. V. Seshu Bai and T. Rajasekharan. “Evidence of a critical Mn-Mn distance for the onset of ferromagnetism in NiAs type compounds”. In: *Journal of Magnetism and Magnetic Materials* 42.2 (1984), pp. 198–200.

A. Appendix

A.1. Data processing

A.1.1. Structural refinement from neutron powder data (Ambient temperature)

Structural refinement of $Mn_3Fe_2Si_3$ at ambient temperature was performed with the program JANA2006 [76] which can handle a wide range of data formats including time-of-flight data in the GSAS format. The starting parameters for the crystal structure model were taken from [20]. An Instrument Parameter File containing information about the POWGEN diffractometer was provided by the beamline staff. Then, we performed Le Bail fitting to determine the zero shift, the profile shape function, background and cell parameters. Afterwards, a Rietveld refinement was performed in which the scale factor, atomic positions, atomic occupations, and atomic displacement parameters (ADP) were refined.

A.1.1.1. Le Bail refinement of time-of flight data

For a time-of-flight neutron diffraction measurement, the three parameters $DIFC$, $DIFA$ and $ZERO$ relate the d-spacing of a specific powder line to its time of flight, as follows:

$$t = DIFC * d + DIFA * d^2 + ZERO, \tag{A.1}$$

where $ZERO$ is the zero shift and $DIFC$ and $DIFA$ are coefficients for a specific bank on a time of flight diffractometer.

As for the peak shape, we described it with a convolution between a Pseudo-Voigt (PV) function and a back-to-back exponential[83]:

$$\Omega(x) = \int_{-\infty}^{+\infty} PV(x-t)E(t)dt, \tag{A.2}$$

The parameter x is the location of the peak, where the exponentially modelled neutron pulse goes from being exponentially rising to exponentially decaying. The back-to-back exponential function is expressed by the parameters α and β describing the exponential rising and the exponential decay constant of neutron pulse as follows [83]:

$$
\begin{aligned}
E(t) &= \frac{\alpha\beta}{(\alpha+\beta)} e^{\alpha t} \quad t \leq 0 \\
E(t) &= \frac{\alpha\beta}{(\alpha+\beta)} e^{\alpha t} \quad t > 0,
\end{aligned}
\tag{A.3}
$$

According to the GSAS manual [83], the profile coefficients α and β can be defined by:

$$
\begin{aligned}
\alpha &= alpha0 + \frac{alpha1}{d} \\
\beta &= beta0 + \frac{beta1}{d^4},
\end{aligned}
\tag{A.4}
$$

The Pseudo-Voigt function (PV) is a linear combination of Gaussian (G) and Lorentzian (L) functions [84]:

$$pV(x) = \eta L(x) + (1-\eta)G(x), \tag{A.5}$$

where η is a mixing factor. In the case of neutron TOF-data, the Gaussian (σ_G) and Lorentzian (γ_L) components of the Pseudo-Voigt function have the following dependence with d-spacing[83]:

$$\sigma_G^2 = \sigma_0^2 + (\sigma_1^2 + DST2(1-\xi)^2)d^2 + (\sigma_2^2 + Gsize)d^4) \tag{A.6}$$

$$\gamma_G = \gamma_0 + (\gamma_1 + \xi\sqrt{8ln2DST2})d + (\gamma_2 + F(sz)d^2) \tag{A.7}$$

Where $Gsize$ is a Gaussian size parameter, $DST2$ is the contribution of the anisotropic strain, ξ is the Lorentzian strain fraction and F(SZ) represents a Lorentzian anisotropic size contribution. (σ_0) $Sig0$, (σ_1) $Sig1$, (σ_2) $Sig2$ and (γ_0) $Gam0$, (γ_1) $Gam1$, (γ_2) $Gam2$, present the variance parameter of the Gaussian and Lorentzian component of the psuedo-voigt function, respectively.

The Le Bail refinement strategy used is the following. The background was described by 10 terms of Legendre polynomial combined with 70 background points assigned manually. The lattice parameters, $DIFA$ and the peak shape parameters $Sig0$, $Sig1$, $Sig2$, $Gam0$, $Gam1$, $Gam2$, $alpha0$, $beta0$ were carefully refined, while $ZERO$, $DIFC$ and $alpha1$, $beta1$ are instrument dependent and were fixed to the values taken from the instrument parameter file provided by the instrument scientist. In order to get a realistic standard deviation on the lattice parameter, Berar's correction [85] was applied.

Only the instrumental contribution to the peak shape and width were considered in the profile fitting, while, the additional sample effects such as strain, stress or size effects were neglected.

A.1.1.2. Rietveld refinement

After the LeBail refinement, we used the Rietveld refinement [86, 87] to extract information about the $Mn_3Fe_2Si_3$ structure.

Molecular formula	$Mn_3Fe_2Si_3$
Molecular weight (g/mol)	360.77
ρ_{calc} (g/cm^{-3})	6.18(7)
Z	2
Space group	P$6_3/mcm$ (193)
a(Å)	6.85763(18)
c(Å)	4.75799(15)
V(Å^3)	193.77(1)
R_p	3.46
wR_p	2.39
R_{obs}	2.06
wR_{obs}	3.04
GOF	2.53
CWL(Å)	0.8
d-spacing coverage(Å)	0.1340-8.200

Table A.1.: Lattice parameter, unit cell volume and final agreement factors from the Rietveld refinement of $Mn_3Fe_2Si_3$ at 300 K

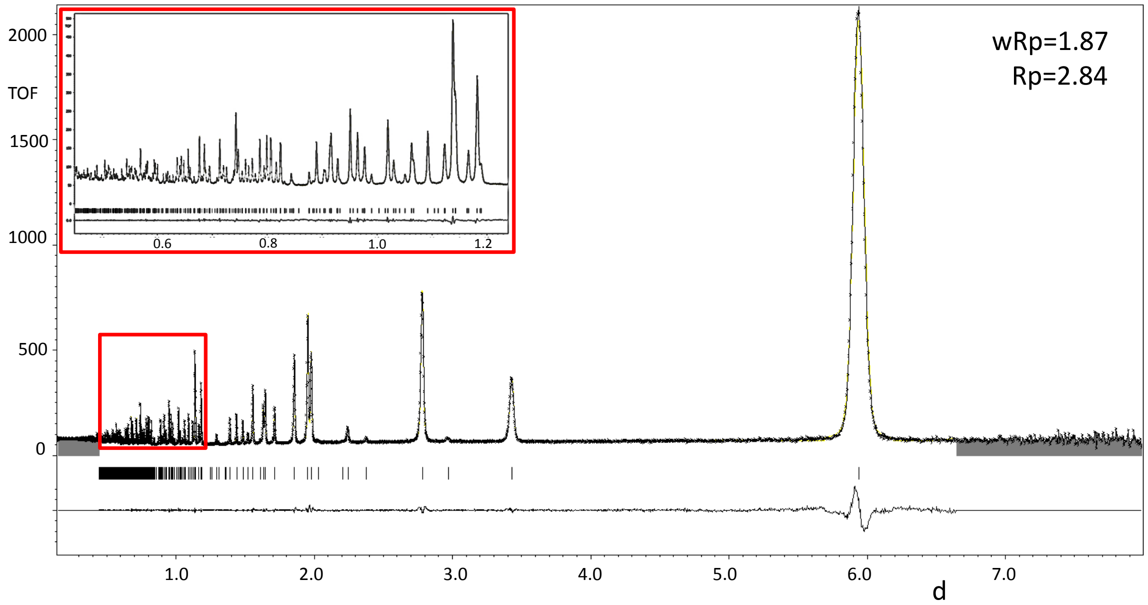

Figure A.1.: LeBail refinement of the ToF neutron powder diffraction data taken on $Mn_3Fe_2Si_3$ at 300 K.

Initially, only the scale factor was refined. Then, the atomic positions, the ADP and the occupancy parameters were subsequently added to the refinement. Based on the starting model which was taken from [20], we considered that both the 4d and 6g sites are occupied by Mn and Fe. The ADPs and coordinates were kept identical for the pair of atoms located on the same site and for each of the sites the sum of occupancies was restricted to the ideal value. As the resulting values corresponded within their standard deviations to the ideal stoichiometry, the occupancies were restricted to the ideal proportions 3 Mn and 2 Fe. This did not lead to a significant change in the overall agreement factors.

In the final refinement stage, the value of the intensity, was corrected for the effects of sample absorption, using [83]:

$$A_k = exp[-\mu R d], \tag{A.8}$$

where μR is a refinable parameter and presents the product of the radius of the cylindrical sample and its linear absorption coefficient.

Finally, a correction for preferred orientation according to March-Dollase was applied [83]:

$$P_k = \frac{1}{M_p} \sum_{K=1}^{M_p} [P1^2 cos^2\alpha_k + P1^{-1} sin^2\alpha_k]^{\frac{-3}{2}}, \tag{A.9}$$

where P1 is a refinable parameter, and α_k is the angle between the preferred orientation axis ([001] in this case) and the reflection vector P_k. M_p is the multiplicity of a reflection.

Final agreement factors are given in table A.1. Structural parameters are provided in table A.2. The quality of a Rietveld refinement can be judged by the following criteria:

a) The profile fit which can be evaluated visually by looking at the plot of the observed and calculated patterns

b) This can be also expressed numerically with quantities related to the least-square process employed in the Rietveld method. These quantities are as follows [88]:

$$R_p = \frac{\sum_i |y_i(obs) - y_i(cal)|}{\sum_i y_i(obs)}, \tag{A.10}$$

$$wR_p = \left(\frac{\sum_i w_i[y_i(obs) - y_i(cal)]^2}{\sum_i w_i[y_i(obs)]^2} \right)^{\frac{1}{2}}, \tag{A.11}$$

$$R_{exp} = \left(\frac{N - P}{\sum_i w_i[y_i(obs)]^2} \right)^{\frac{1}{2}}, \tag{A.12}$$

$$GOF = \left(\frac{wR_p}{R_{exp}} \right)^2, \tag{A.13}$$

where R_p, wR_p, R_{exp} are the profile, weighted profile, and expected R factors, GOF is the goodness of fit, respectively. $y_i(obs)$, $y_i(cal)$ are the observed and calculated intensity at the point i,respectively. The weights w_i are taken from the experimental errors. P is the number of least-squares parameters and N is the number of observations.

c) Reasonable inter-atomic distances, bond angles and atomic displacement parameters

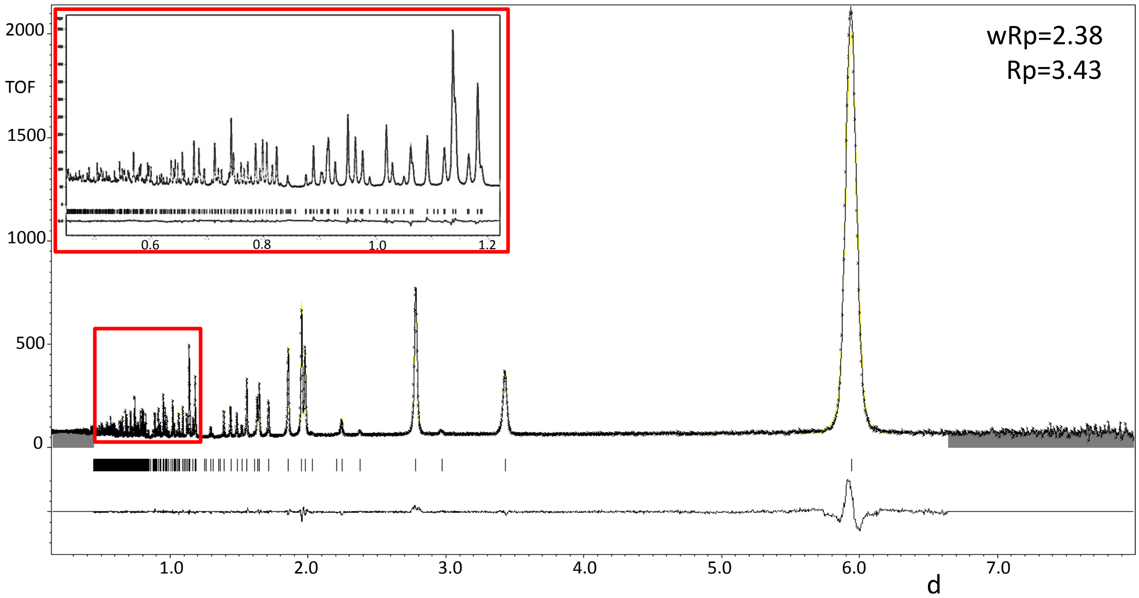

Figure A.2.: Rietveld refinement of neutron TOF powder diffraction pattern of $Mn_3Fe_2Si_3$ at 300 K.

Atom (WP)	x	y	z	U_{iso}	occ
Fe1 (4d)	0.666667	0.333333	0	0.0047(2)	0.1275(7)
Mn1 (4d)	0.666667	0.333333	0	0.0047	0.0390
Mn2 (6g)	0.2263(4)	0	0.25	0.0017(4)	0.2109
Fe2 (6g)	0.2263(4)	0	0.25	0.0017	0.0390
Si (6g)	0.5980(2)	0	0.25	0.0049(3)	0.25

Table A.2.: Atomic coordinates, isotropic displacement parameters and occupation factors of $Mn_3Fe_2Si_3$ at 300 K, from refinements of neutron powder diffraction data.

A.1.2. Processing of single crystal x-ray data

A.1.2.1. Conversion of the synchrotron data

The processing of the synchrotron data in the current thesis was done with the $CrysAlis^{Pro}$ software [89]. The measured images in the tiff format were renamed and converted to the Esperanto format using this software. Initial values for x_0 and y_0 describing the position of the primary beam on the measured frames, as well as an initial value for the detector distance were extracted using a calibration measurement on corundum. At all temperatures, the runs corresponding to the ϕ scans (see Table 5.4) were initially combined together using $CrysAlis^{Pro}$.

A.1.2.2. Indexing and determination of detector parameters.

Prior to data processing, all the frames were checked visually, to make sure that they are not corrupted. Then, a peak hunting procedure was started using the peak hunting option of CrysAlis^{Pro}. The program automatically searches through all frames for pixels above a threshold level. For the search, the default, with 1000 for the threshold for peak intensities and 20 for the average intensity in a $7x7$ pixel area was used [89].

Once the peak hunting was done, the distribution of reflections was checked with the reciprocal lattice viewer. Then, the orientation matrix (UB-matrix) was determined based on the positions of the peaks using an algorithm implemented into $CrysAlis^{Pro}$ [89]. This matrix describes the orientation of the reciprocal axes with respect to a reference system of the diffractometer.

Afterwards, in order to get an accurate orientation matrix, we refined the lattice parameter restricted according to the hexagonal symmetry together with the sample-to-detector distance d and the values of x_0, y_0 describing the position of the primary beam. Additional values describing goniometer offsets and detector inclination were also refined.

Special care was taken that all runs at a specific temperature had the same orientation matrix to ensure that the data could be easily combined afterwards. Data at other temperatures were treated in an analogous way, however, refined instrument parameters obtained at room temperature were kept fixed and used for all other temperatures. This is important to ensure consistency of the unit cell parameters at all temperatures.

A.1.2.3. Data integration and finalization

Once the orientation matrix was refined, we started the data reduction by integrating the runs individually. During the integration of each run a proper mask was applied to the beam stop and to the shadowed region caused by the cryostat. For the definition of the individual runs see Table 5.4. The data reduction was done by assuming $P1$ as symmetry in the integration.

The program predicts the positions of the reflections based on the UB-matrix, then it reconstructs reflections with split profiles over several frames. The integrated intensity is then deduced based upon the reflection shape and the background [89].

After the data integration, a frame scaling of data from different runs was done via common reflections in the individual data sets. Four frames were used by default for a single scale factor. Then, the absorption correction was applied empirically by the Scale3 Abspack program implemented in CrysAlisPro [89].

A.1.2.4. Space Group Determination

The files containing the integrated intensities of reflections hkl as well as their standard deviation were used in $Jana2006$ for structure refinement.

After we imported the data corresponding to the different runs into $Jana2006$, they were first scaled together using common reflections. Only common reflections with an overall intensity $F^2(obs)/\sigma(I)$ above 3% were chosen.

To determine the space group symmetry, first the crystal systems are chosen which are in accordance with the supplied unit cell parameters within their accuracy limits.

The overall quality of the data collection was inspected by checking R_{int} values after data reduction. The R_{int} describes the quality of merging intensities of the symmetry-equivalent reflections assuming a certain Laue group, and also helps in the determination of the space group symmetry. The R_{int} is defined as follows [90]:

$$R_{int} = \frac{\sum_i \sum_j |F^2_{i,j}(obs) - \langle F^2_i(obs)\rangle|}{\sum_i \sum_j |F^2_{i,j}(obs)|}, \tag{A.14}$$

where $F^2(obs)$ is the intensity of an individual reflection corrected for Lorentz-polarization, $\langle F^2(obs)\rangle$ is the average value over all measured symmetry equivalent reflections in the chosen Laue group. The first summation includes all independent reflections i, and the second summation runs over all symmetry equivalent reflections j corresponding to the $i-th$ independent reflection [90].

The higher the symmetry, the more reflections are merged. This is reflected in the so-called Redundancy which can be calculated by dividing the total number of measured reflections by the number of reflections after symmetry averaging.

For all the possible Laue symmetries which are in accordance with the lattice parameter, the program averages the reflection intensities and calculates the internal R-values.

Then, the Laue symmetry was selected from the Laue classes suggested by the program. The basis for this choice was a low R_{int} and a high redundancy. On the basis of this criteria the Laue class was chosen as $6/mmm$. In the last step, all space groups in accordance with the Laue symmetry were compared and their extinction rules were checked.

The following extinction rules were fulfilled at all temperatures:

$$\begin{aligned} h0l, 0kl &: l \neq 2n \\ 00l &: l \neq 2n, \end{aligned} \tag{A.15}$$

leading to the two possible space groups $P6_3/mcm$ or $P6_3cm$. Before starting the structural refinement we used the 'manual culling option' in *Jana*2006 [91] to identify and reject eventual outliers on the basis of the intensities of symmetry equivalent reflections (see Table A.7). In order to confirm whether a reflection is an outlier or not, we checked it on the original frame. At all temperatures, only very few reflections (<10) that were integrated close to the shadowed region of the detector had to be rejected.

A.1.2.5. Structure refinement

The starting structural model used for the single crystal refinement at all temperatures was taken from the data refinement of the neutron powder data at room temperature described above. We started structural refinement by refining only the scale factor. Then, the atomic positions and the isotropic as well as anisotropic ADPs were subsequently refined. The occupancies for the Mn and Fe sites were fixed to the values obtained from the Rietveld refinement of the neutron powder data.

The agreement factor between the calculated model and the observed experimental data for single-crystal refinements is similar to the one reported for powder refinements. It is based on the agreement between the observed and calculated structure factors, F_{hkl}.

$$R = \frac{\sum_{hkl} ||F_{hkl}(obs)| - F_{hkl}(cal)||}{\sum_{hkl} |F_{hkl}(obs)|}, \tag{A.16}$$

$$wR = \frac{\sum_{hkl} w_{hkl}||F_{hkl}(obs)| - |F_{hkl}(cal)||}{\sum_{hkl} w_{hkl}|F_{hkl}(obs)|}, \tag{A.17}$$

where w_{hkl} is the weighting factor derived for each measured reflection based on its standard uncertainty. w_{hkl} is usually based on counting statistics and it is defined by expression [92]:

$$w_{hkl} = \frac{1}{\sigma^2_{hkl}(|F_{hkl}(obs)|) + (uF_{hkl}(obs))^2}, \tag{A.18}$$

σ^2_{hkl} is the variance and u is the instability factor. For the refinements, we used the default instability factor 0.01. The 300 K data refinement using $P6_3cm$ didn't show a significantly better R-values compared to the higher-symmetry space group $P6_3/mcm$. On the basis of this results the centrosymmetric space group $P6_3/mcm$ was preferred.

Further details concerning the refinement as well as atomic coordinates and displacement parameters are given in tables A.8, A.7, 7.1, A.9, A.10 and A.11.

A.1.2.6. Magnetic structure refinement

Below transition temperature between $AF2$ and PM, T_{AF2-PM}, additional reflections were observed in the neutron diffraction pattern of $Mn_3Fe_2Si_3$. These reflections are due to the ordering of the magnetic moments of the magnetic ions.

Figure A.3 shows maximal magnetic symmetries for a magnetic phase with propagation vector $k = (\frac{1}{2}, \frac{1}{2}, 0)$ and parent space group $P6_3/mcm$. The graph was obtained using the k-SUBGROUPSMAG tool of the Bilbao Crystallographic Server [93]. Starting from the nuclear structure and the magnetic propagation vector $k = (\frac{1}{2}, \frac{1}{2}, 0)$ referred to the hexagonal cell (space group: $P6_3/mcm$) we obtained the same eight models as derived on the basis of the orthohexagonal setting of the parent structure with space group $Ccmm$ and the propagation vector $k = (0, 1, 0)$ (See Chapter 3.4.1.3). The mathematical derivation of Shubnikov groups related to the space group of the parent structure is also implemented in the Jana program [76].

As already explained in Chapter 3.4.1.3, the most likely magnetic structures of $Mn_3Fe_2Si_3$ below T_{AF2-PM}, crystallize in one of the Shubnikov groups derived from the space group of the parent structure.

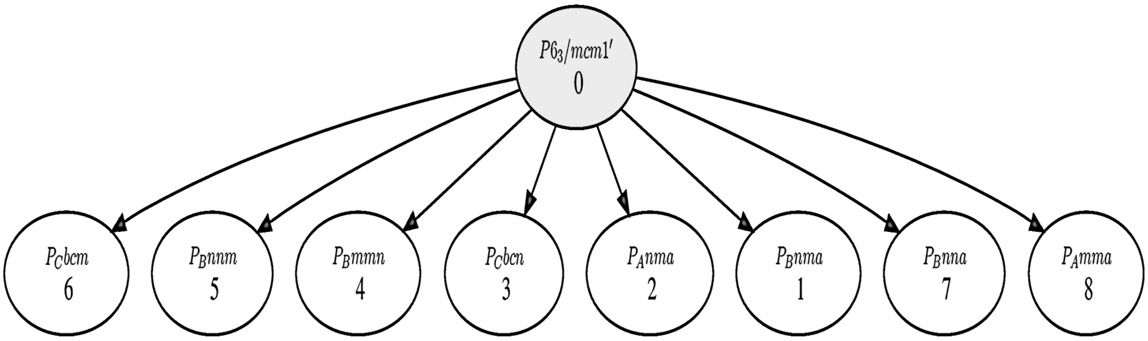

Figure A.3.: Possible magnetic symmetries for a magnetic phase with propagation vector $k = (\frac{1}{2}, \frac{1}{2}, 0)$ and parent space group $P6_3/mcm$. The graph was obtained using k-SUBGROUPSMAG tool of the Bilbao Crystallographic Server.

The magnetic structure refinement of $Mn_3Fe_2Si_3$ was started by importing the parent structure at the desired temperature below T_{AF2-PM}, defining the magnetic atoms, magnetic form factors and propagation vector.The profile and the structure parameters of the parent structure with the exception of the background parameters were fixed to the values obtained by the LeBail and Rietveld refinement of the nuclear structure.

For each selected magnetic symmetry, the magnetic ions occupying the same site were restricted to having identical magnetic moments. Then, the magnetic moments were refined using the selected magnetic symmetry as defined by the specific Shubnikov space group. A polynomial background was also refined and combined with the manual background. Finally, the magnetic space group which led to the magnetic model that best fitted the measured neutron diffraction pattern was chosen as the correct one.

Below $T_{AF1-AF2}$ at 50 and 20 K, additional magnetic reflections are observed in the neutron powder diffraction diagrams. For some of them significant discrepancies between observed and calculated intensities are observed, indicating that the chosen model is not correct for the low temperature AF1 phase. To obtain a more satisfactory fit we had to lower the magnetic symmetry. This was achieved by deriving the maximal translationengleiche subgroups of *Ccmm* for the description of the nuclear structure (See Table A.3) using Jana [76]. The symmetry of the nuclear structure was still restricted to *Ccmm* with the help of local symmetry operators. Different magnetic space groups based on the maximal translationengleiche subgroups of *Ccmm* were then derived (See Table A.3) and refined.

<table>
<tr><td>N.I.S.G</td><td colspan="8">Cc2m</td></tr>
<tr><td>M.S.G</td><td>P[C]c2m</td><td>P[C]n2n</td><td>P[C]c2$_1$n</td><td>P[C]n2$_1$m</td><td>P[C]c2m</td><td>P[C]n2n</td><td>P[C]c2$_1$n</td><td>P[C]n2$_1$m</td></tr>
<tr><td>N.I.S.G</td><td colspan="8">C2mm</td></tr>
<tr><td>M.S.G</td><td colspan="2">P[C]2mm</td><td colspan="2">P[C]2an</td><td colspan="2">P[C]2$_1$am</td><td colspan="2">P[C]2$_1$mn</td></tr>
<tr><td>N.I.S.G</td><td colspan="8">Cmc2$_1$</td></tr>
<tr><td>M.S.G</td><td colspan="2">P[C]cm2$_1$</td><td colspan="2">P[C]na2$_1$</td><td colspan="2">P[C]nm2$_1$</td><td colspan="2">P[C]ca2$_1$</td></tr>
<tr><td>N.I.S.G</td><td colspan="8">C222$_1$</td></tr>
<tr><td>M.S.G</td><td colspan="2">P[C]222$_1$</td><td colspan="2">P[C]2$_1$2$_1$2$_1$</td><td colspan="2">P[C]22$_1$2$_1$</td><td colspan="2">P[C]2$_1$22$_1$</td></tr>
<tr><td>N.I.S.G</td><td colspan="8">C2/c</td></tr>
<tr><td>M.S.G</td><td colspan="2">P[C]-1</td><td colspan="2">P[C]-1</td><td colspan="2">P[C]-1</td><td colspan="2">P[C]-1</td></tr>
<tr><td>N.I.S.G</td><td colspan="8">C2/m</td></tr>
<tr><td>M.S.G</td><td colspan="2">P[C]2/m</td><td colspan="2">P[C]2$_1$/a</td><td colspan="2">P[C]2/a</td><td colspan="2">P[C]2$_1$/m</td></tr>
<tr><td>N.I.S.G</td><td colspan="8">C2$_1$/m</td></tr>
<tr><td>M.S.G</td><td colspan="2">P[C]2$_1$/m</td><td colspan="2">P[C]2$_1$/n</td><td colspan="2">P[C]2$_1$/n</td><td colspan="2">P[C]2$_1$/m</td></tr>
</table>

Table A.3.: Magnetic space groups **M.S.G** derived from each non-isomorphic subgroup **N.I.S.G** of *Ccmm*. All magnetic space groups correspond to the setting of a C-centered cell of the nuclear structure.

A.1.3. Extraction of Merlin data

A.1.3.1. Converting $I(t, x, y, \psi)$ to $S(\vec{Q}, \omega)$

During the so called Horace scan the instrument records the intensity as function of time-of-flight t between the sample and the detector pixel (x, y) into a .nxspe file for each setting of the angle ψ, which describes the rotation around the vertical axis, and for each initial energy E_i, i.e. we recorded 5 .nxspe files per angle setting. All files for a given E_i are then converted into $S(\vec{Q}, \omega)$, transforming the time-of-flight into energy transfer $\hbar\omega$ and using the pixel information to calculate the momentum transfer $\vec{Q}$. As the energy transfer is a quadratic function of the time-of-flight t the transformation from measured intensity into the scattering function involves a multiplication by a factor t^4, which can lead to a overestimation of the background for large t, i.e. large energy transfer from the neutron to the sample.

This procedure of the conversion is rather time consuming even on a powerful computer and takes up to several hours depending on the number of files to be combined. In the end we had acquired 5 .sqw files containing $S(\vec{Q}, \omega)$ for each initial energy

E_i. The largest E_i covers the largest reciprocal lattice volume albeit with the most relaxed resolution of momentum and energy transfer.

Similar to creating the UB matrix at a single crystal diffractometer, the spectrometer coordinate system has to be aligned to the crystal coordinate system. For that we created a list of reflections based on the preliminary alignment and the ambient temperature lattice parameter in the orthohexagonal setting. After we determined the peak positions for this list the software calculates the goniometer angles G_S, G_L and the offset of the $\psi, d\psi$ and refines the lattice parameters to transform from the starting coordinate system to the actual crystal orientation, see Fig. A.4. Since we intended to refine 6 parameters and keep the lattice angles fixed, our list contained 22 reflections.

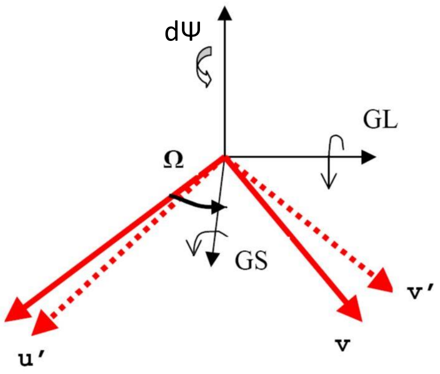

Figure A.4.: Diagram describing virtual goniometer angles. GL and GS describe the settings of the large and small goniometers, Ω is the offset of the axis of the small goniometer Gs with respect to the vector v and $D\psi$ specify the offset in ψ, taken from [64].

A.1.3.2. Data visualisation

Once the .sqw files had been created for all E_i at 5 K and 125 K, we used Horace [64] to visualize and analyze the data. So, in order to make and view cuts and slices, we needed to define the filename of the $sq\omega$ file and the projection axes for our data visualization u=[1,0,0] and v=[0,0,1](we can also choose projection axes irrespective of the orientation of the sample). In general, cuts with Horace are made by specifying axes of each component of Q and energy as either plot with axis range and step size or integration axes. This way Horace provides complete flexibility to plot 3D volumes, 2D slices and 1D cuts along specified trajectories in (Q, ω)-space.

Table A.4 lists input details about the E_i integration range, the Q_l integration range (perpendicular to the plot plane) and the plot axis Q_h and Q_k between given limits with a given minimum possible step size, used to cut 2D elastic slices of (hk0) planes at different E_i (See Figures A.14, A.15, A.16 and A.17).

E_i (meV)	[lower bound, upper bound]		[low, step,high]	
	E	Q_l	Q_h	Q_k
9	[-1,1]	[-0.1,0.1]	[-1.5,0.03,1.5]	[-8,0.03,2]
13	[-1,1]	[-0.1,0.1]	[-2,0.03,1.5]	[-9,0.03,3]
21	[-2,2]	[-0.1,0.1]	[-2.5,0.05,2]	[-11.5,0.05,2.5]
40	[-3,3]	[-0.1,0.1]	[-3,0.05,3]	[-16,0.05,3]
108	[-5,5]	[-0.1,0.1]	[-4,0.1,3.6]	[-25.5,0.1,5]

Table A.4.: Input details for hk0-slices at different E_i integrated over the full elastic line

The minimum the momentum transfer step size listed in Table A.4 have been specified during the data manipulation. If a smaller momentum transfer step size is chosen, one observes artefact described by the white breaks in the low Q_k regions i.e. the step size within Horace is much wider than the chosen one (see Figure A.5).

Considering the calculation of integrated intensities, as already mentioned in section 5.5.1 the measurement was done with large angular steps. Therefore, we cannot be sure that we have collected the integrated peak intensity. Figure A.6 shows a 1D-cut along the (Q_h,-2,0) axis. Only two data points above the FWHM were observed in the magnetic peak (-1,-2,0) indexed in the orthohexagonal setting. This is similar for all measured magnetic peaks and the number of data points is not sufficient to determine the integrated intensities reliably.

A.1.4. Extraction of integrated intensity from HZB data

The extraction of integrated intensity has been performed using the LAMP program (Large Array Manipulation Program) [94]. After launching LAMP, the appropriate instrument calibration file provided by the instrument scientist was loaded into LAMP. Then, the collected data for an individual reflection (*.NeXus format) were imported by selecting the corresponding run number and plotted.

Each Bragg reflection was measured by performing an ω scan with fixed 2θ over about 4.1 ° in steps of 0.1 °. Detector images were taken for every point in the scan (see Figure A.12). With the help of a macro written by the instrument scientist, all spectra were summed up and stored into a new workspace (See Figure A.13). The two dimensional Bragg peaks were integrated over the x and y axes of the detector and plotted as a function of ω using LAMP. The extracted one-dimensional peaks were then fitted using a Gaussian function plus linear background (see figure A.7). The high background level limits the reliability of the determination of integrated intensities as the transition temperature was approached.

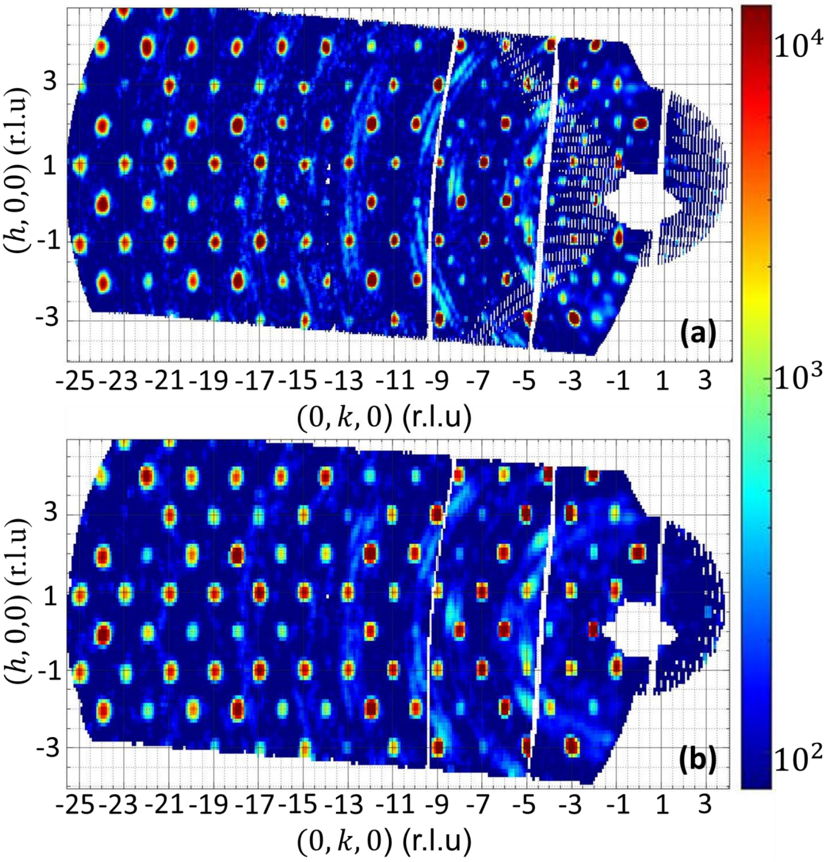

Figure A.5.: Elastic scattering maps of the $(hk0)$ plane measured on Merlin at T=125 K with E_i=108 meV, by integrating in the energy range between -5 meV and 5 meV and integrating $(0, 0, l)$ between -0.1 and 0.1, with different momentum transfer step size for the $(h, 0, 0)$ and $(0, k, 0)$ axis (a) h=[-2,0.05,13], k =[-10.5,0.05,8], (b) h=[-2,0.1,13], k=[-10.5,0.1,8].

A.1.5. Processing of macroscopic data

A.1.5.1. Magnetization data

As described in section 5 the data at the Quantum Design systems were typically collected in sweep mode. Therefore the individual scans of field- or temperature-series did not share the same abscissa values, which is needed, when we treat data from different scans. The calculation of the numerical derivatives from sweep measurements yields a very noisy signal due to the small step size of the x-values (See Figure A.8).

To account for that, the temperature and magnetic field dependent magnetization data were re-binned using a linear interpolation algorithm before performing the numerical differentiation. The linear interpolation was done first by reducing the 1D data-set size to a tenth of its original size. Then a data point was estimated by constructing a line between two neighboring data points. The derivative calculation was

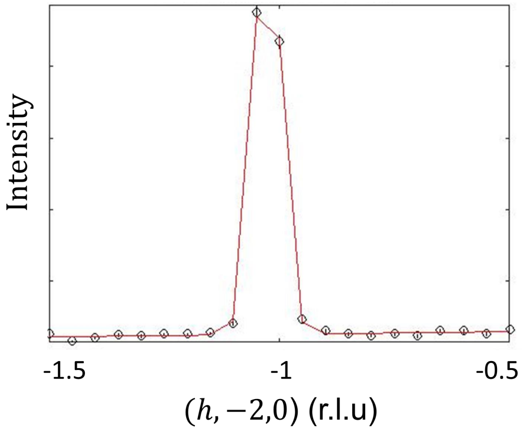

Figure A.6.: 1D-cut along the (Q_h,-2,0) axis at 5K and E_i=21 meV, with E=[-2,2], Q_l=[-0.1,0.1], Q_k=[-2.1,-1.9] and Q_h=[-1.525,0.05,-0.475,]. [low,high] for integration between two limits, [low,step,high] for a plot axis between given limits with a given step size.

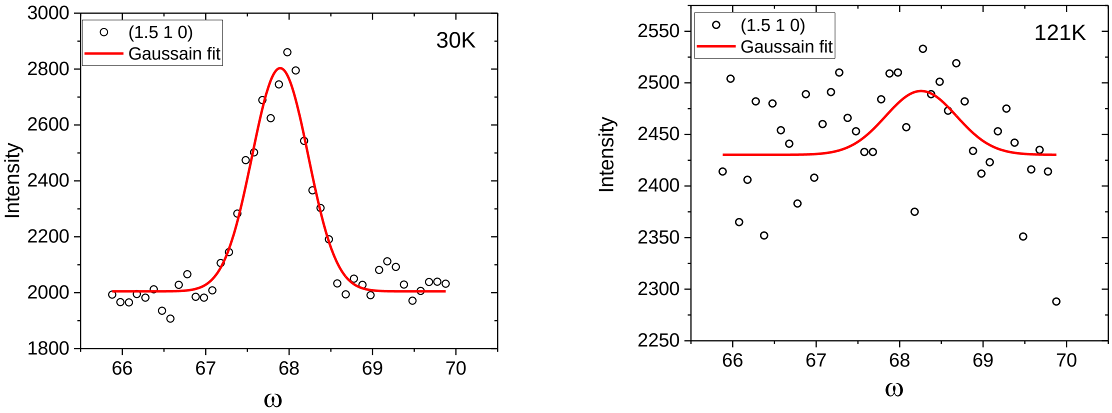

Figure A.7.: Gaussian fitting of the magnetic peak (1.5 1 0) measured at 30 K and 121 K.

then done by taking the average of the slopes between the point and its two closest neighbors using the central difference approximation.

As for the magnetic field dependent magnetization derivative, the re-binned data measured when the field is in sweep mode is consistent with the raw data measured with smaller steps at the same temperatures when the field is in driven mode (see Figure A.9a). The critical field is determined by fitting a Gaussian peak shape on a sloping background. We use the peak width (FWHM) as a measure for the width of the metamagnetic transition (see Figure A.9b).

A python script was built to extract isofield data from the isothermal measurements. An array was created, which contained all the temperatures measured for the construction of the file names. Four columns of the field dependent measurements

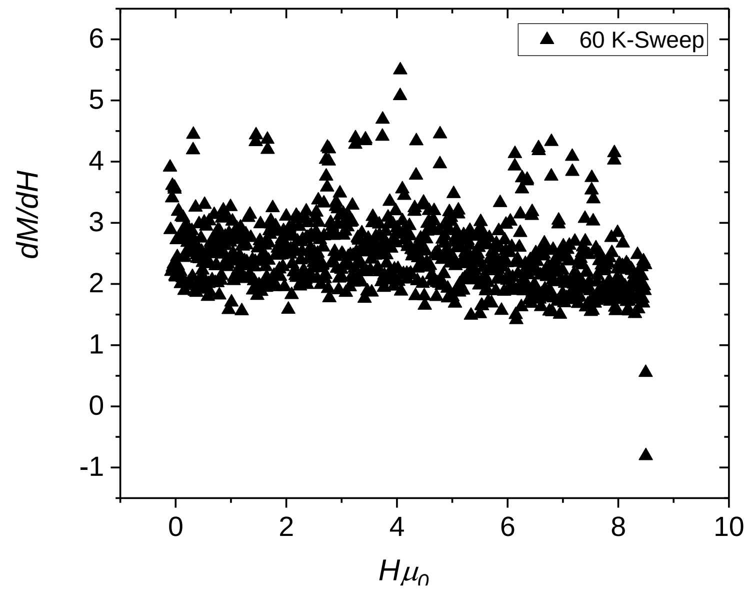

Figure A.8.: dM/dH curve calculated from raw data measured when the field is in sweep mode.

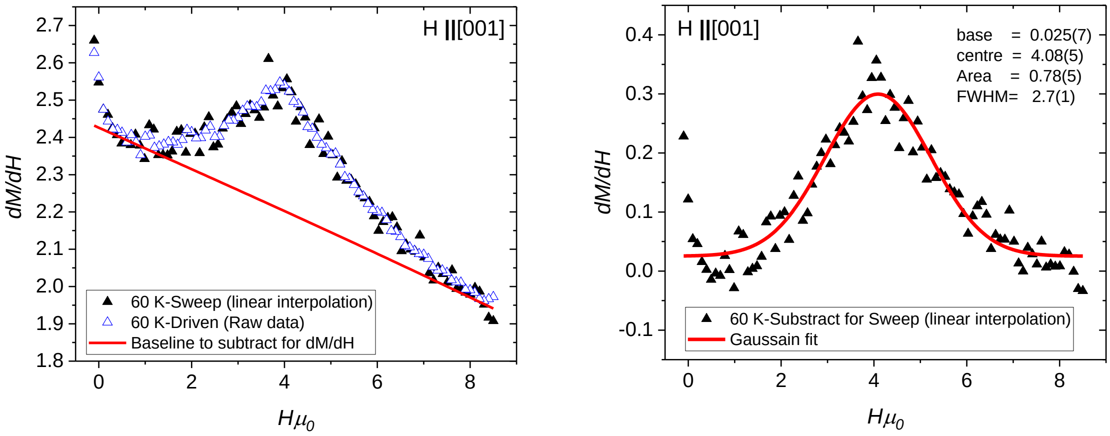

(a) (b)

Figure A.9.: (a) a comparison between dM/dH curves (blue) calculated from raw data measured when the field is in driven mode and (black) data measured in sweep mode and smoothed using linear interpolation; the base line (red line) is used to substract the dM/dH data ; (b) Gaussian fit of the subtracted dM/dH.

from the data files were loaded. These were the temperature, the applied field, the magnetization and the error on the magnetization. Then the data was interpolated to fixed field values (from 0 to 7.9 T) and arranged in a temperature x field matrix. The interpolation using Python was done using the PCHIP algorithm which stands for Piecewise Cubic Hermite Interpolating Polynomial. This interpolator preserves monotonicity in the interpolation data and does not overshoot if the data is not smooth, which guarantees a calculation of continuous first derivatives. The entropy change $-\Delta S_{iso}$ was calculated using the formulae presented in Eq. 3.19. The calculation was done by taking the numerical temperature derivative of the isofield magnetization curves and taking the sum over the discrete field settings that were measured (see Figure A.18).

A.1.5.2. Heat capacity

In the case of magnetic materials, the total heat capacity at constant pressure C_p, can be divided into three constituents, namely, the lattice heat capacity C_l, the electronic heat capacity C_e and the magnetic heat capacity C_m :

$$C_p = C_{p,l} + C_{p,e} + C_{p,m} \tag{A.19}$$

The lattice contribution is estimated with the Debye model. In the framework of the Debye model, the acoustic modes give the dominant contribution to the heat capacity. Debye assumed a linear dispersion relation for the lattice vibration up to the cut-off frequency ω_D. This yields a density of states of $D(\omega) = \frac{V\omega^2}{2\pi^2\nu^3}$ up to ω_D. This leads to the following expression for the Debye specific heat [27]:

$$C_v = 9NR\left(\frac{T}{\theta_D}\right)^3 \int_0^{\frac{\theta_D}{T}} \frac{x^4 e^x}{(e^x - 1)^2} dx \tag{A.20}$$

Where N is the number of atoms in the unit cell, $R = 8.314 J\,mol^{-1} K^{-1}$ is the ideal gas constant and $\theta_D = \frac{\hbar\omega_D}{K_B}$ is the Debye temperature [27].

Besides the lattice contribution to the total specific heat A.19, the electronic contribution of the conduction electron subsystem has to be considered. The small fraction of electrons filling the band up to the Fermi level can be excited thermally (defined by Fermi-Dirac statistics) and make a small contribution to the heat capacity. This electronic contribution to heat capacity is proportional to T at any temperature and may become a dominant term at very low temperatures. The electronic heat capacity for the Fermi gas model is given by [27]:

$$C_{v,e} = \left[\frac{\pi^2 N K_B^2}{2E_F}\right] T = \gamma_e T, \tag{A.21}$$

where E_F is the Fermi energy and γ_e is the Sommerfeld coefficient.

So, below 10 K, the heat capacity of the non magnetic isostructural reference compound Ti_5Si_3 was fitted to the equation sum of the lattice C_l and the electronic contribution C_e. The electronic contribution was estimated to be $\gamma_e = 15.4(4)\, mJ\, mol^{-1} K^{-2}$ and Θ_D=547(5) K.

Then, the magnetic contribution C_m to the total specific heat of $Mn_3Fe_2Si_3$, was estimated by subtracting the interpolated nonmagnetic isostructural reference compound Ti_5Si_3 curve from that of $Mn_3Fe_2Si_3$. For this, the Ti_5Si_3 curve was scaled with the factor of 0.9473 to account for the different Debye temperature due to the different molar mass of the compounds [95]:

$$\frac{\theta_D(Mn_3Fe_2Si_3)}{\theta_D(Ti_5Si_3)} = \left[\frac{M(Ti_5Si_3)}{M(Mn_3Fe_2Si_3)}\right]^{\frac{1}{2}} \tag{A.22}$$

A.2. Graphs

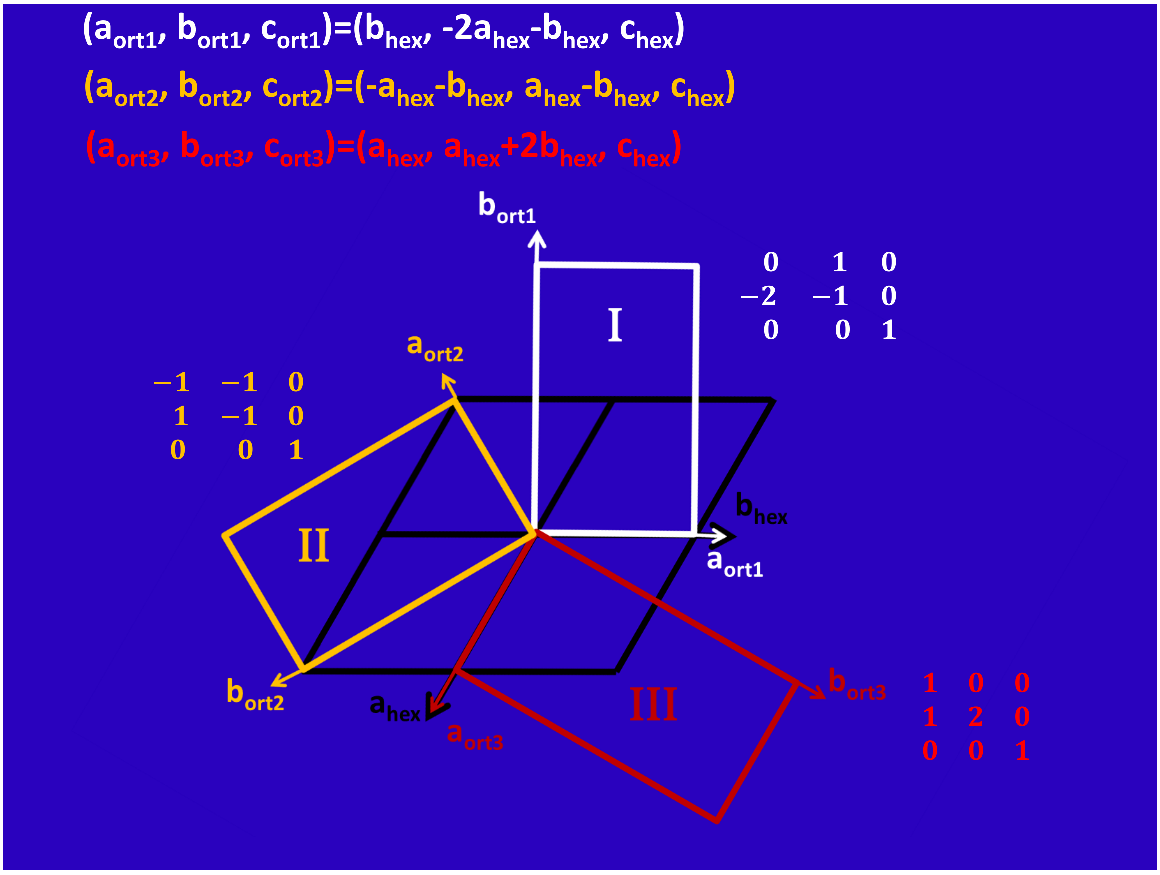

Figure A.10.: The transformation from the hexagonal to the corresponding ortho-hexagonal coordinates in the real space.

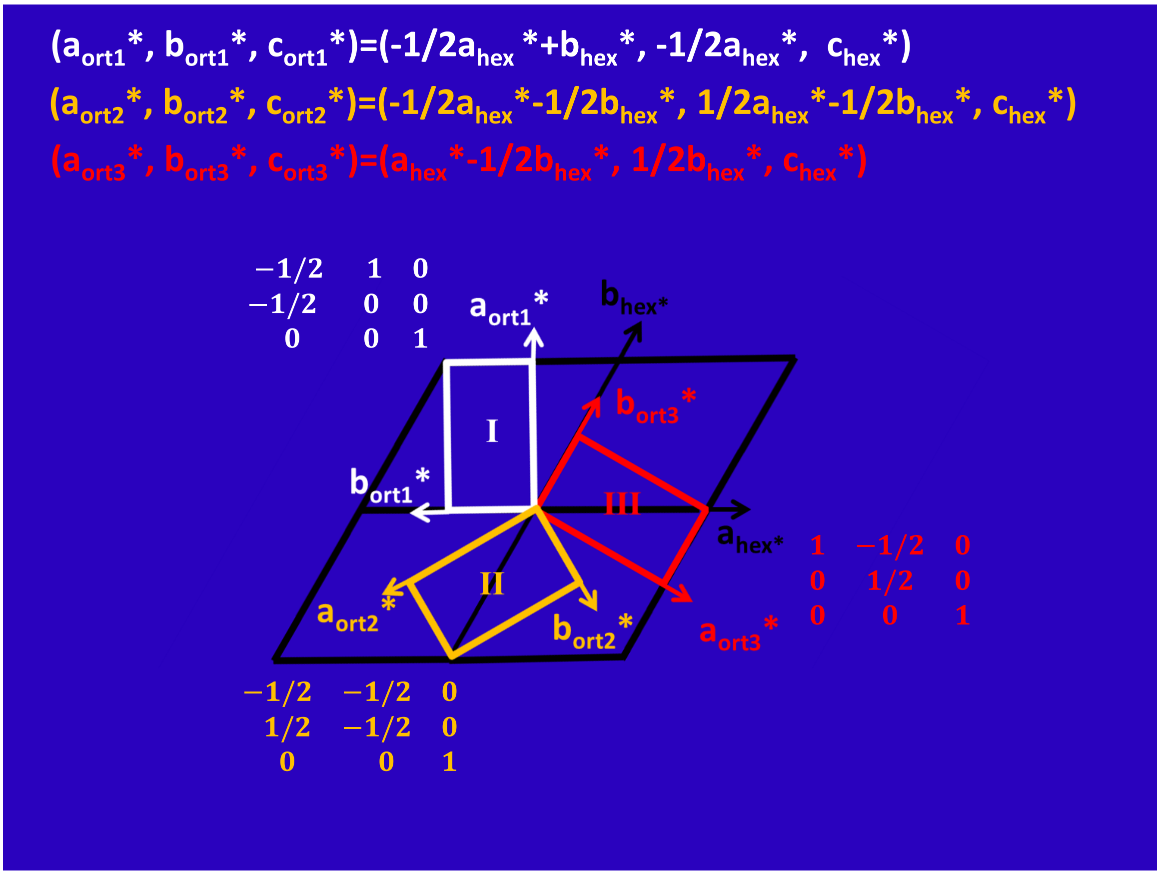

$(a_{ort1}^{*}, b_{ort1}^{*}, c_{ort1}^{*})=(-1/2a_{hex}^{*}+b_{hex}^{*}, -1/2a_{hex}^{*}, c_{hex}^{*})$

$(a_{ort2}^{*}, b_{ort2}^{*}, c_{ort2}^{*})=(-1/2a_{hex}^{*}-1/2b_{hex}^{*}, 1/2a_{hex}^{*}-1/2b_{hex}^{*}, c_{hex}^{*})$

$(a_{ort3}^{*}, b_{ort3}^{*}, c_{ort3}^{*})=(a_{hex}^{*}-1/2b_{hex}^{*}, 1/2b_{hex}^{*}, c_{hex}^{*})$

$$\begin{matrix} -1/2 & 1 & 0 \\ -1/2 & 0 & 0 \\ 0 & 0 & 1 \end{matrix}$$

$$\begin{matrix} 1 & -1/2 & 0 \\ 0 & 1/2 & 0 \\ 0 & 0 & 1 \end{matrix}$$

$$\begin{matrix} -1/2 & -1/2 & 0 \\ 1/2 & -1/2 & 0 \\ 0 & 0 & 1 \end{matrix}$$

Figure A.11.: The transformation from the hexagonal to the corresponding ortho-hexagonal coordinates in the reciprocal space.

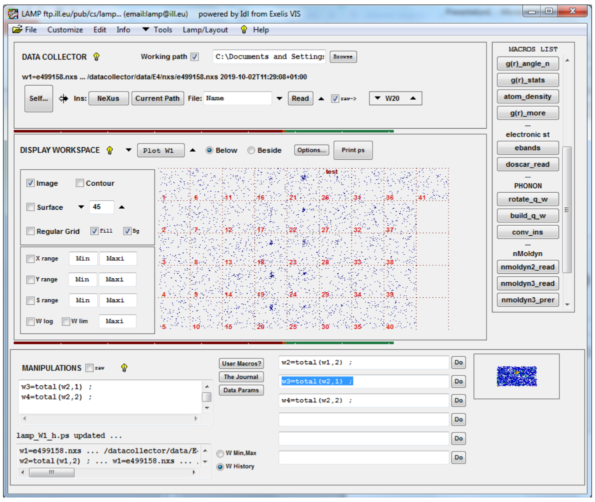

LAMP ftp.ill.eu/pub/cs/lamp... (email:lamp@ill.eu) powered by Idl from Exelis VIS

Working path ☑ C:\Documents and Settings

w1=e499158.nxs ... /datacollector/data/E4/nxs/e499158.nxs 2019-10-02T11:29:08+01:00

File: Name

☑ Image ☐ Contour

☐ Surface 45

☐ Regular Grid ☑ Fill ☑ Bg

```
w3=total(w2,1) ;
w4=total(w2,2) ;
```

lamp_W1_h.ps updated ...

```
w1=e499158.nxs ... /datacollector/data/E
w2=total(w1,2) ; ... w1=e499158.nxs ...
```

```
w2=total(w1,2) ;
w3=total(w2,1) ;
w4=total(w2,2) ;
```

Figure A.12.: LAMP window: Detector images of the magnetic reflection (1.5 1 0) measured at 20 K.

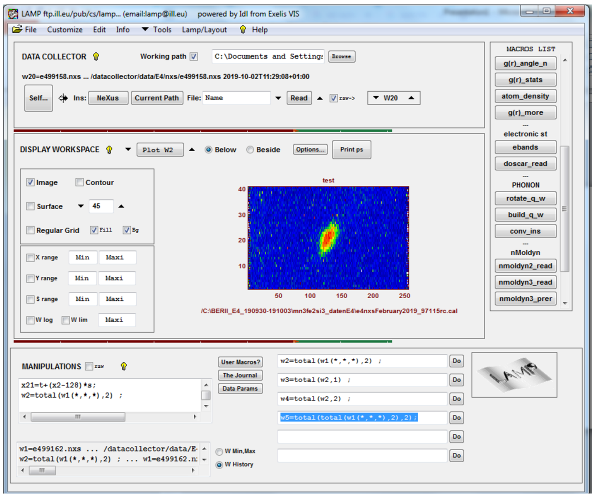

Working path ☑ C:\Documents and Setting:

w20=e499158.nxs ... /datacollector/data/E4/nxs/e499158.nxs 2019-10-02T11:29:08+01:00

File: Name ☑ raw->

● Below ○ Beside

☑ Image ☐ Contour
☐ Surface 45
☐ Regular Grid ☑ Fill ☑ Bg
☐ X range Min Maxi
☐ Y range Min Maxi
☐ S range Min Maxi
☐ W log ☐ W lim Maxi

/C:\BERII_E4_190930-191003\mn3fe2si3_datenE4\e4nxsFebruary2019_97115rc.cal

☐ raw

```
x21=t+(x2-128)*s;
w2=total(w1(*,*,*),2) ;
```

```
w2=total(w1(*,*,*),2) ;
w3=total(w2,1) ;
w4=total(w2,2) ;
w5=total(total(w1(*,*,*),2),2);
```

```
w1=e499162.nxs ... /datacollector/data/E
w2=total(w1(*,*,*),2) ; ... w1=e499162.n
```

○ W Min,Max
● W History

Figure A.13.: LAMP window: Detector image of the magnetic reflection (1.5 1 0) measured at 20 K.

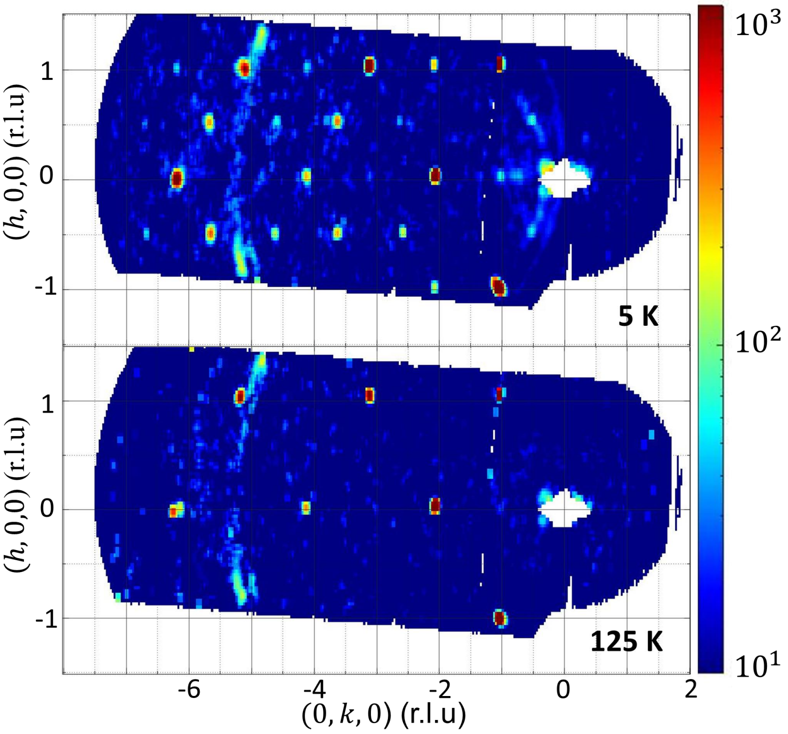

Figure A.14.: Elastic scattering maps of the $(hk0)$ plane measured on Merlin at T=125 K with E_i=9 meV, by integrating energy between -1 meV and 1 meV and integrating $(0, 0, l)$ between -0.1 and 0.1, with h=[-1.5,0.03,1.5], k =[-8,0.03,2]

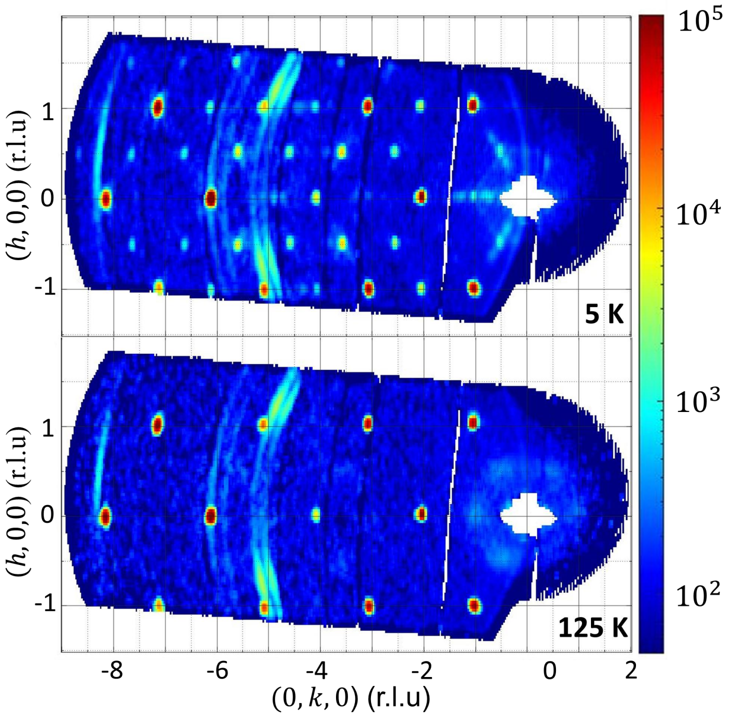

Figure A.15.: Elastic scattering maps of the $(hk0)$ plane measured on Merlin at T=125 K with E$_i$=13 meV, by integrating energy between -1 meV and 1 meV and integrating $(0, 0, l)$ between -0.1 and 0.1, with h=[-1.5,0.03,2], k =[-9,0.03,2]

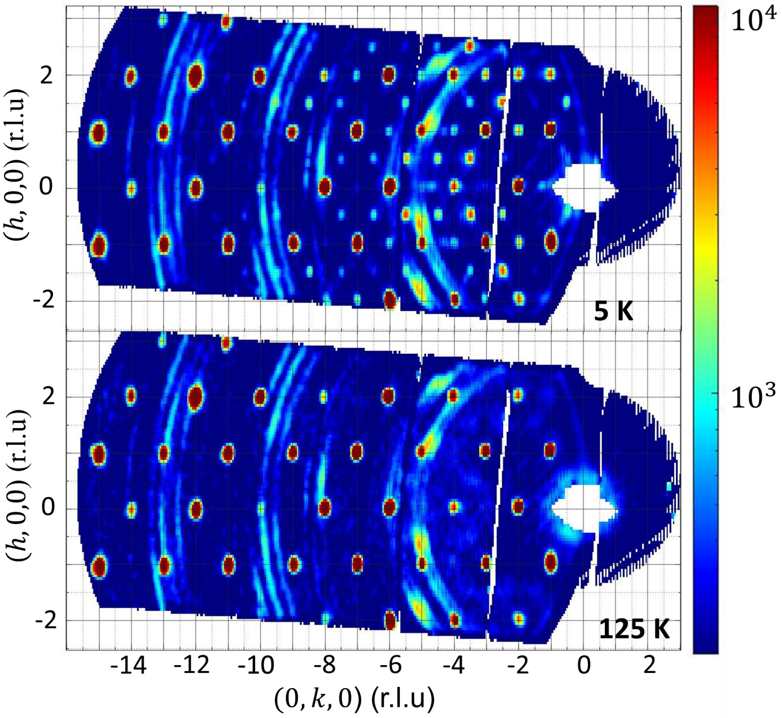

Figure A.16.: Elastic scattering maps of the $(hk0)$ plane measured on Merlin at T=125 K with E_i=40 meV, by integrating energy between -3 meV and 3 meV and integrating $(0, 0, l)$ between -0.1 and 0.1, with h=[-2.5,0.05,4], k=[-16,0.05,3]

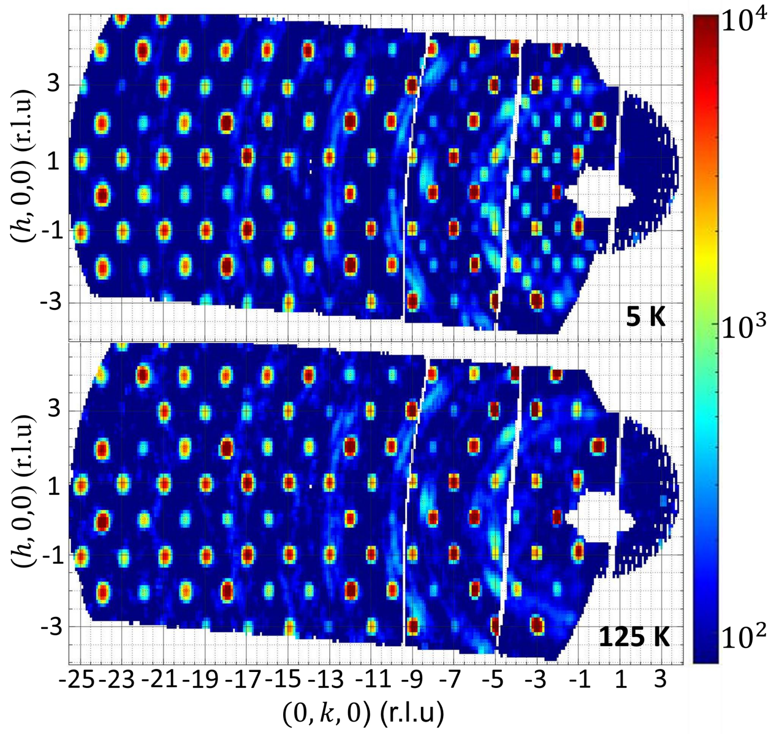

Figure A.17.: Elastic scattering maps of the $(hk0)$ plane measured on Merlin at T=125 K with E_i=108 meV, by integrating energy between -3 meV and 3 meV and integrating $(0, 0, l)$ between -0.1 and 0.1, with h=[-3.5,0.1,4], k=[-25.5,0.1,1.5]

```
In [1]: from pylab import *
        %matplotlib inline
        import numpy as np
        #import jvtools
        from scipy.interpolate import interp1d, PchipInterpolator
```

```
In [2]: name = lambda n:"MN3FE2SI3_AB_ISOFIELD_{0}OE.DAT".format(n)
        B_set = [500, 5000, 15000, 25000, 35000, 45000, 65000, 85000]
        B = []
        M_inter = []
        for n in range(len(B_set)):
            t,b,m=genfromtxt(name(B_set[n]),unpack=True, usecols=(2,3,4), skip_header=25, delimiter=',')
            b =  b*1e-4
            B.append(mean(b))
            index = t.argsort()
            m = m/11.2e-3
            M_inter.append(PchipInterpolator(t[index[::4]],m[index[::4]]))
```

```
In [3]: temp = arange(11,350)
        dmdt = [x.derivative(1) for x in M_inter]
        dB = diff(B)
        dS = zeros(size(temp))
        dS = dS + B[0]*dmdt[0](temp)
        for x in range(5):
            dS = dS + (B[x+1]-B[x])*0.5*(dmdt[x](temp)+dmdt[x+1](temp))
            plot(temp, -dS,"-v", label="{:2.1f} T".format(B[x+1]))
        legend=plt.legend(loc="upper left", bbox_to_anchor=[1, 1], ncol=1, shadow=None, title="H$\perp$[001]", fancybox=True,fontsize=16)
        legend.get_title().set_fontsize('15')
        xlabel("Temperature [K]",fontsize=14)
        ylabel(r"$-\Delta S$ J kg$^{-1}$K${-1}$", fontsize=14)
        array_out = np.column_stack((temp, -dS))
```

Figure A.18.: Python scripts used to calculate $-\Delta S_{iso}$ for $H\perp[001]$.

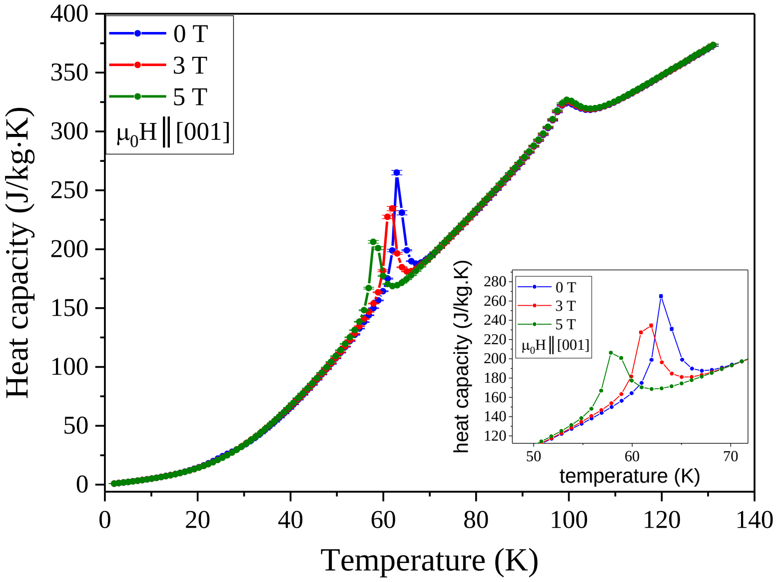

Figure A.19.: Temperature dependence of total heat capacity of Mn_5Si_3 at different fields with $\vec{H}\|[001]$ up to 150 K. Data taken from [65]

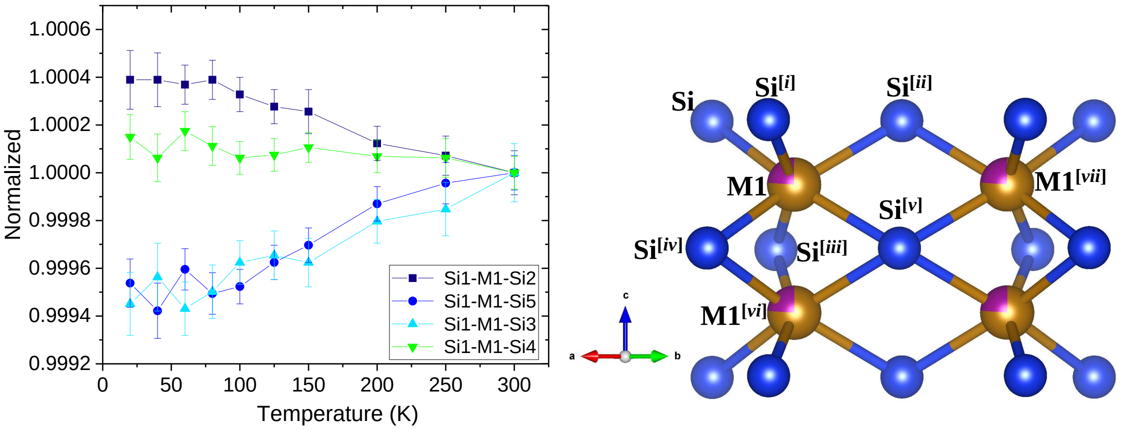

Figure A.20.: Temperature dependence of the bond angles in the crystal structure of $Mn_3Fe_2Si_3$.

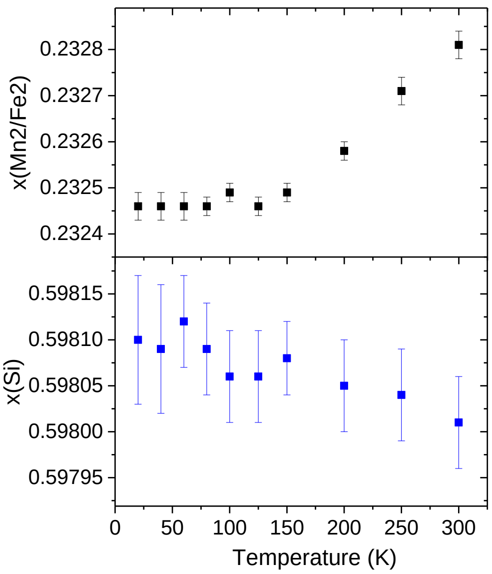

Figure A.21.: Temperature dependence of the x(Mn2/Fe2) and x(Si) atomic coordinates in $Mn_3Fe_2Si_3$.

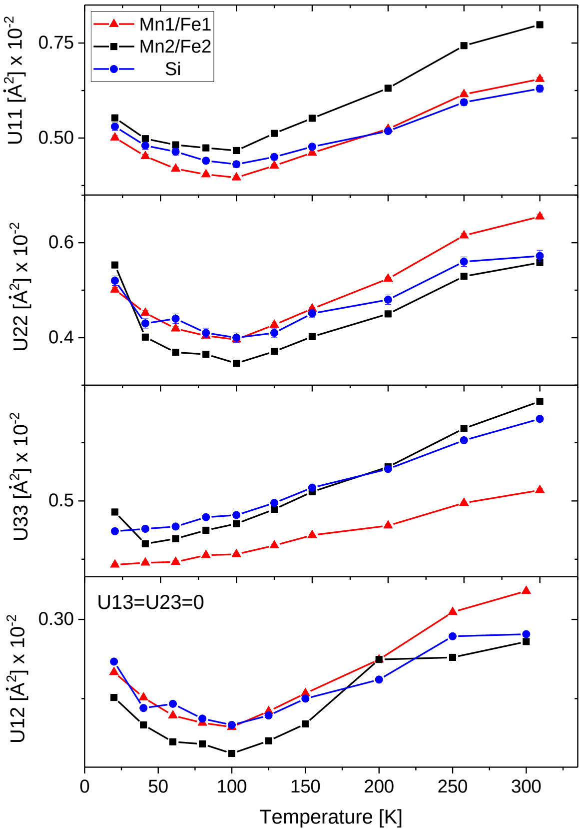

Figure A.22.: Temperature dependence of Anisotropic displacement parameters of (Mn1/Fe1), (Mn2/Fe2) and Si in $Mn_3Fe_2Si_3$.

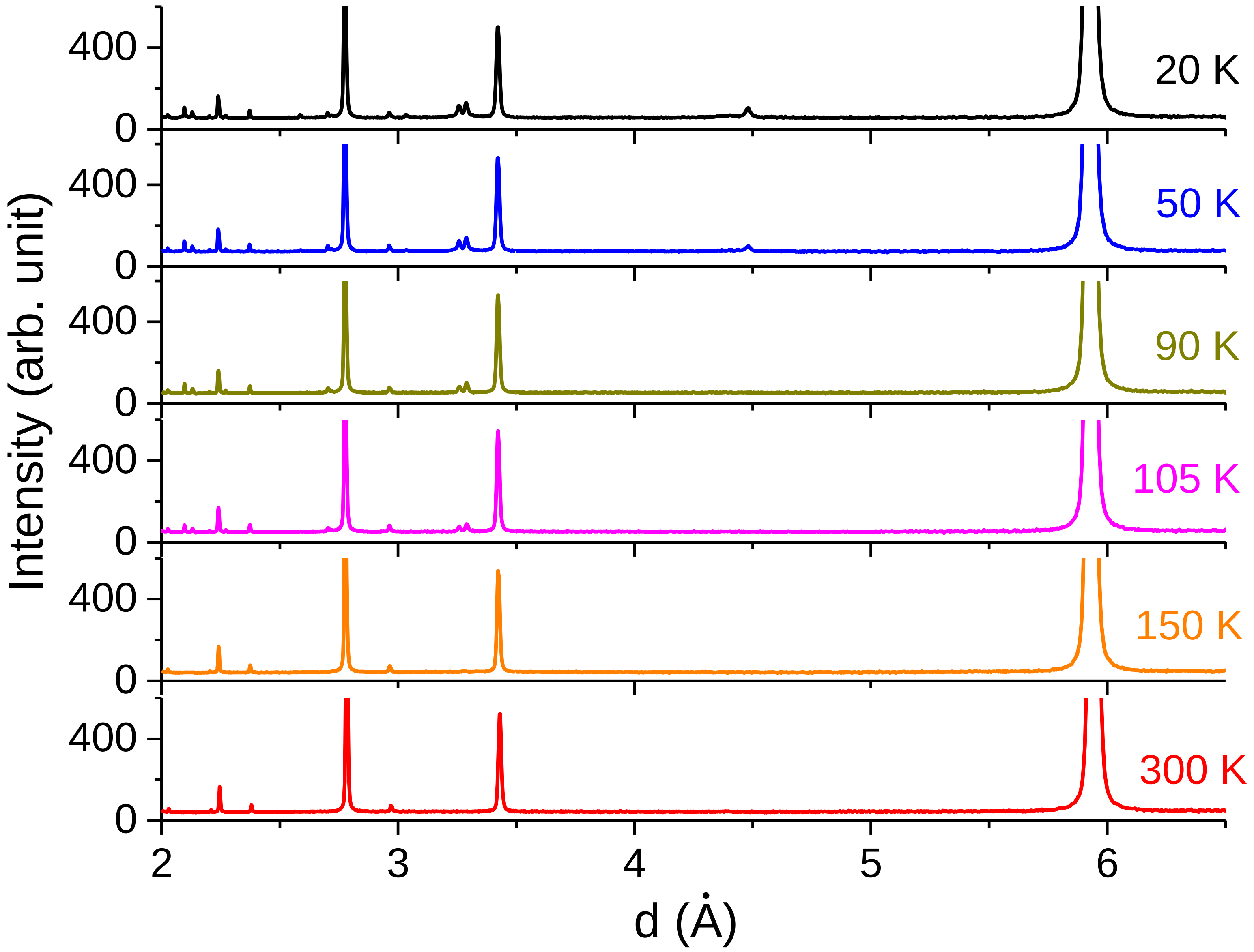

Figure A.23.: $Mn_3Fe_2Si_3$ neutron powder diffraction obtained on POWGEN in the region [2-6]Å at different temperatures for a center wavelength of 2.665 Å.

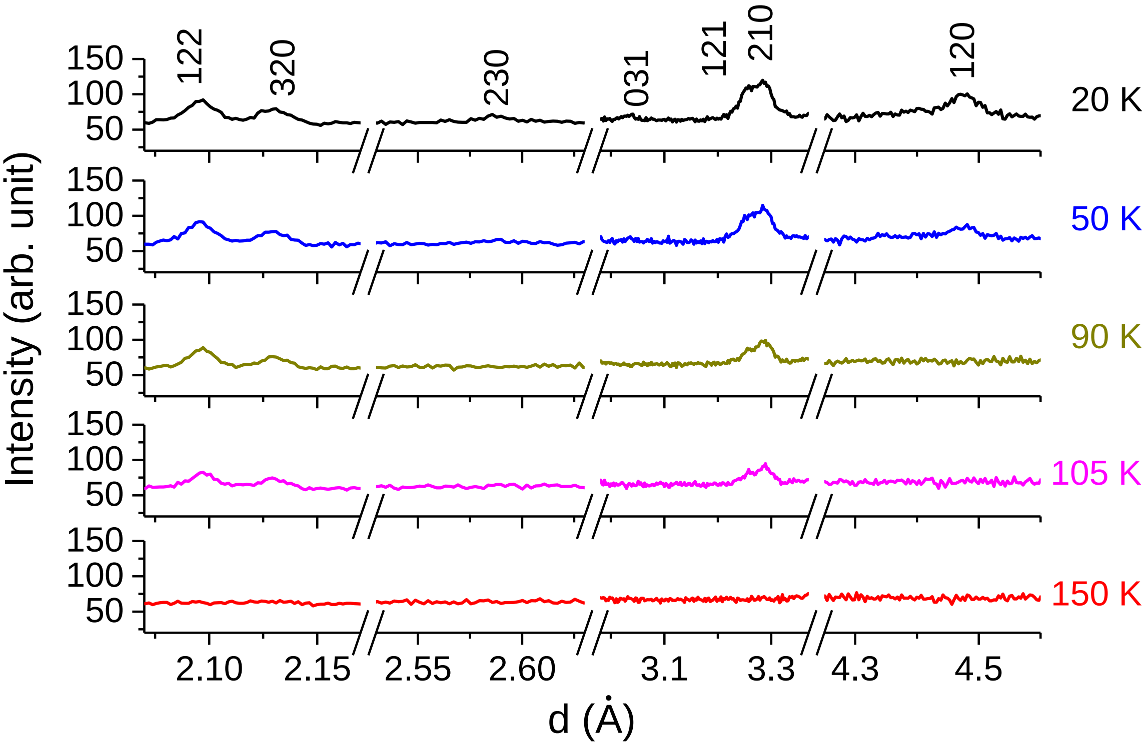

Figure A.24.: $Mn_3Fe_2Si_3$ neutron powder diffraction obtained on POWGEN at different temperatures for a center wavelength of 0.8 Å. The multiple axis breaks present the d(Å) regions with the strongest magnetic Bragg reflections indexed using *Ccmm* space group.

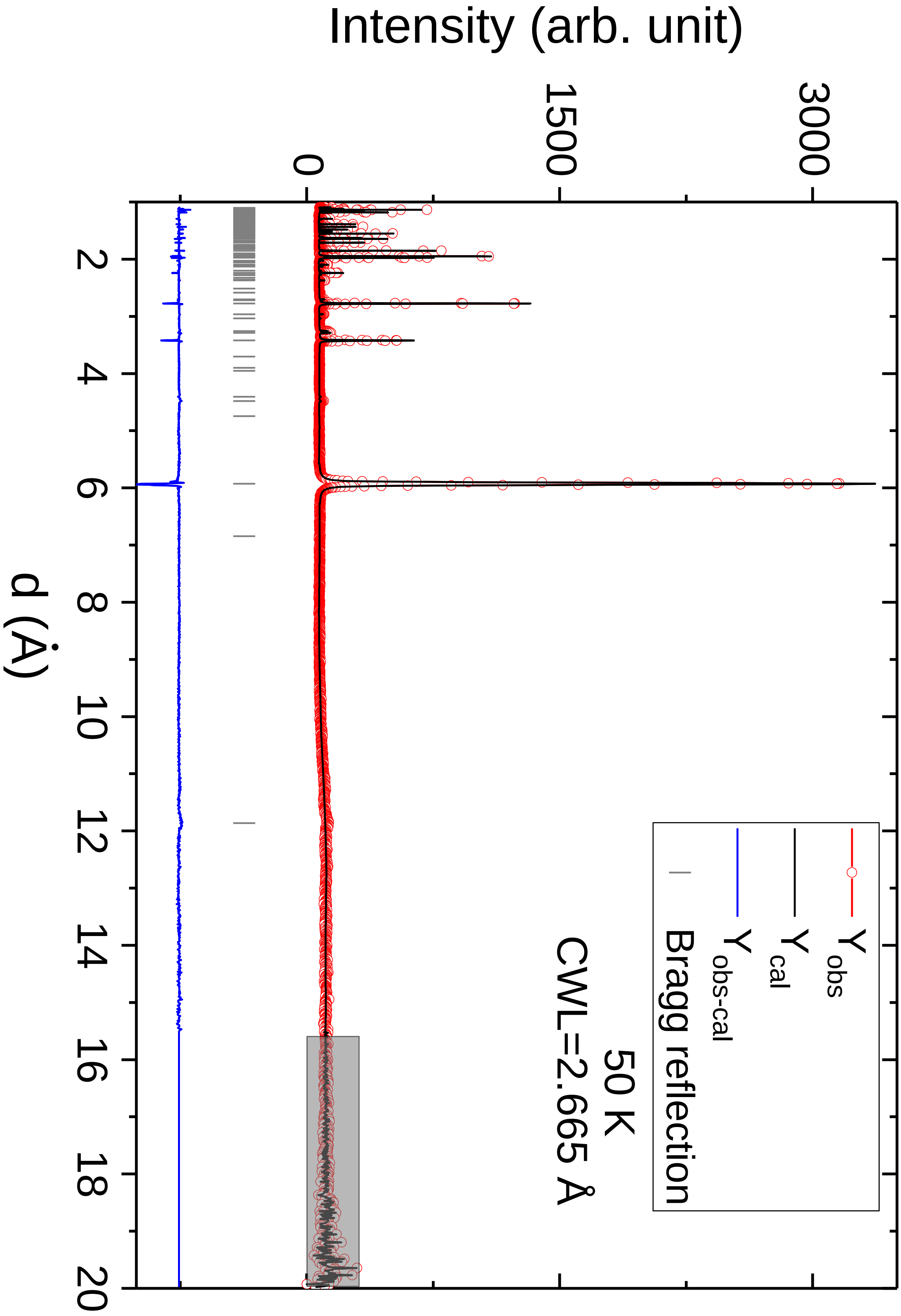

Figure A.25.: $Mn_3Fe_2Si_3$ neutron powder pattern obtained on POWGEN at 50 K for a center wavelength of 2.665 Å. Gray tick marks indicate the positions of nuclear and magnetic reflections.The difference curve is shown below on the same scale.

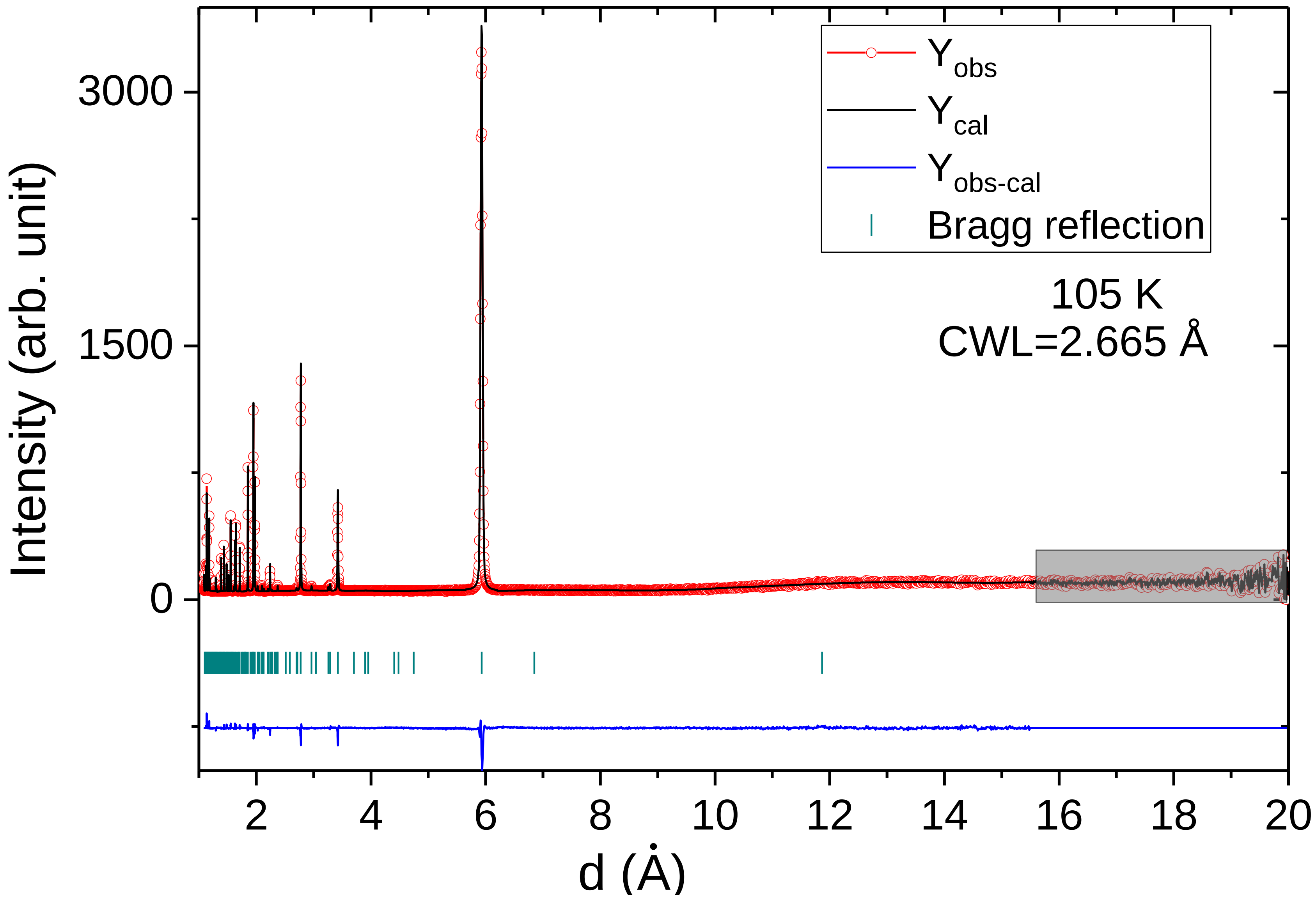

Figure A.26.: $Mn_3Fe_2Si_3$ neutron powder pattern obtained on POWGEN at 105 K for a center wavelength of 2.665 Å. Gray tick marks indicate the positions of nuclear and magnetic reflections.The difference curve is shown below on the same scale.

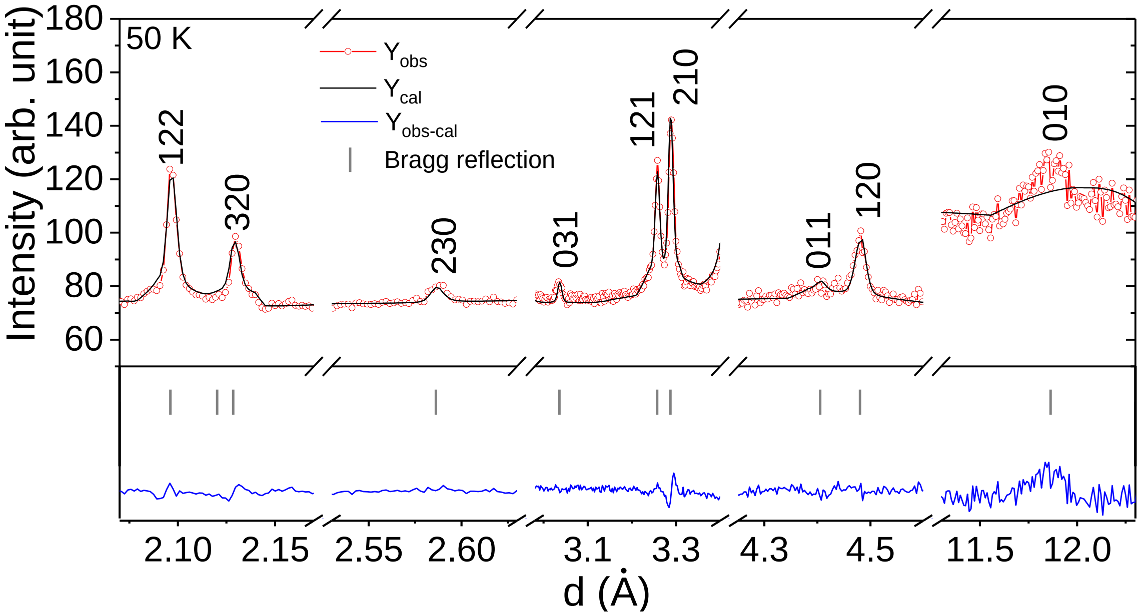

Figure A.27.: $Mn_3Fe_2Si_3$ neutron powder pattern obtained on POWGEN at 50 K for a center wavelength of 2.665 Å. Gray tick marks indicate the positions of the magnetic reflections. The difference curve is shown below on the same scale. The multiple axis breaks present the d(Å) regions with the strongest refined magnetic Bragg reflections indexed using *Ccmm* space group. The magnetic space group model used for the fitting is $P[C]222_1$.

A.3. Tables

[a] determined after the calibration on corundum; [b] provided by beamline scientist; [c] Scan information details for each run are presented in Table 5.4

Input format	$*$.*mccd*
Rotation ∘ / Mirror	90 / Disabled
pixel size (mm)	0.0790
x_0, y_0 [a]	1006, 1020
synchrotron / lambda (Å)[b]	Enabled / 0.4428
Polarisation factor (Plofact)	0.02
monochromator	MIRROR/SYNCROTRON
Detector distance (mm)[a]	80
Scan info [c]	Enabled
Use frames in inverse order	Enabled

Table A.5.: Parameters for the conversion data images collected at the synchrotron P24 beamline (EH2) to *Esperanto* format.

T (K)	a (Å)	c (Å)	V (Å^3)
300	6.85336(11)	4.75556(8)	193.437(5)
250	6.84914(10)	4.75173(7)	193.043(5)
200	6.84389(9)	4.74742(6)	192.573(4)
150	6.83953(10)	4.74247(7)	192.127(5)
125	6.83762(10)	4.74089(6)	191.955(5)
100	6.83591(10)	4.73887(6)	191.777(5)
80	6.83547(13)	4.73789(7)	191.713(6)
60	6.83486(12)	4.73785(7)	191.678(5)
40	6.83426(19)	4.73694(11)	191.607(9)
20	6.8341(2)	4.73711(10)	191.606(9)

Table A.6.: Lattice parameter and unit cell volume of $Mn_3Fe_2Si_3$ from LeBail refinements of X-ray powder diffraction data.

T [K]	No. of meas. refl. (obs/all)	hmin⟶hmax; kmin ⟶kmax; lmin ⟶lmax	Sym. ind. refl (obs/all)	R(int) (obs/all)	R (obs/all)	wR (obs/all)	No. of param.	Culled (man/auto)	No. of Runs
300	8136/11477	-11⟶17 -18⟶ 14 -12 ⟶8	655/787	5.52/5.56	2.45/3.15	2.59/2.74	12	4/0	3
250	8408/11453	-17 ⟶11 -14 ⟶ 18 -12 ⟶8	668/785	5.42/5.46	2.39/2.95	2.68/2.79	12	4/0	3
200	8603/11415	-17 ⟶ 11 -14⟶18 -12 ⟶ 8	679/782	4.35/4.39	2.08/2.63	2.69/2.77	12	3/0	3
150	8601/11399	-17⟶ 11 -12 ⟶14 -8 ⟶12	670/779	4.27/4.31	2.02/2.56	2.25/2.34	12	3/0	3

Table A.7 continued from previous page

T [K]	No. of meas. refl. (obs/all)	hmin⟶hmax; kmin ⟶kmax; lmin ⟶lmax	Sym. ind. refl (obs/all)	R(int) (obs/all)	R (obs/all)	wR (obs/all)	No. of param.	Culled (man/auto)	No. of Runs
125	8610/11410	-17 ⟶ 11 -14⟶18 -12⟶8	665/777	4.22/4.27	2.20/2.67	2.48/2.57	12	4/0	3
100	8565/11357	-17 ⟶ 11 -12⟶14 -8⟶12	662/774	4.01/4.06	2.17/2.80	2.53/2.62	12	2/0	3
80	8527/11378	-17⟶ 11 -12⟶14 -8⟶12	660/774	4.46/4.51	2.40/3.01	2.67/2.76	12	2/0	3
60	8449/11376	-17⟶11 -12⟶14 -8⟶12	654/774	4.40/4.46	2.35/3.01	2.57/2.71	12	2/0	3

Table A.7 continued from previous page

T [K]	No. of meas. refl. (obs/all)	hmin⟶hmax; kmin ⟶kmax; lmin ⟶lmax	Sym. ind. refl (obs/all)	R(int) (obs/all)	R (obs/all)	wR (obs/all)	No. of param.	Culled (man/auto)	No. of Runs
40	3291/4572	-16⟶9 -14⟶18 -12⟶5	619/766	3.69/3.80	2.39/3.42	2.83/3.02	12	1/0	1
20	3220/4563	-9 ⟶ 16 -18⟶14 -12⟶5	617/765	3.48/3.58	2.56/3.52	2.56/2.73	12	3/0	1

Table A.7.: Details of the structure refinements on $Mn_3Fe_2Si_3$ in space group $P63/mcm$ based on x-ray diffraction data.

T(K)	Tmin	Tmax
300	0.059	1
250	0.313	1
200	0.459	1
150	0.423	1
125	0.35	1
100	0.356	1
80	0.487	1
60	0.435	1
40	0.249	1
20	0.314	1

Table A.8.: Empirical absorption correction of $Mn_3Fe_2Si_3$ using spherical harmonics, implemented in SCALE3 ABSPACK scaling algorithm [89].

T (K)	x(Mn2/Fe2)	x(Si)	U_{iso}(Mn1/Fe1)	U_{iso}(Mn2/Fe2)	U_{iso}(Si)
300	0.23281(3)	0.59801(5)	0.00619(3)	0.00788(4)	0.00692(7)
250	0.23271(3)	0.59804(5)	0.00573(3)	0.00718(4)	0.00645(7)
200	0.23258(2)	0.59805(5)	0.00479(2)	0.00594(3)	0.00549(7)
150	0.23249(2)	0.59808(4)	0.00427(2)	0.00517(3)	0.00501(6)
125	0.23248(3)	0.59805(6)	0.00390(2)	0.00467(3)	0.00460(7)
100	0.23249(2)	0.59806(5)	0.00356(2)	0.00420(3)	0.00429(7)
80	0.23246(2)	0.59809(5)	0.00361(20	0.00419(3)	0.00436(7)
60	0.23246(3)	0.59812(5)	0.00359(2)	0.00410(3)	0.00437(7)
40	0.23246(3)	0.59806(7)	0.00379(3)	0.00415(4)	0.00441(9)
20	0.23246(3)	0.59810(7)	0.00409(3)	0.00449(4)	0.00482(9)

Table A.9.: Atomic coordinates, isotropic displacement parameters of $Mn_3Fe_2Si_3$ from the refinements of x-ray single crystal diffraction data in $P6_3/mcm$. Mn1/Fe1 and Si1 occupy WP $6g$ (x 0 1/4) and Fe2 occupies WP $4d$ (2/3 1/3 0).

T [K]	(Mn1/Fe1)			(Mn2/F2)			
	U_{11}	U_{33}	U_{12}	U_{11}	U_{22}	U_{33}	U_{12}
300	0.00655(5)	0.00546(6)	0.00327	0.00798(5)	0.00558(6)	0.00927(6)	0.00279
250	0.00615(4)	0.00491(5	0.00307	0.00743(5	0.00529(5)	0.00811(5)	0.00264
200	0.00524(3)	0.00394(4)	0.00262	0.00631(4)	0.00450(4)	0.00646(4)	0.00262
150	0.00461(3)	0.00353(4)	0.00230	0.00552(4)	0.00402(4)	0.00539(4)	0.00201
125	0.00427(4)	0.00309(5)	0.00213	0.00512(4)	0.00371(5)	0.00464(5)	0.00185
100	0.00396(4)	0.00271(5)	0.00198	0.00467(4)	0.00346(5)	0.00402(4)	0.00173
80	0.00404(4)	0.00267(5),	0.00202	0.00474(4)	0.00365(5)	0.00374(5),	0.00182
60	0.00419(4)	0.00238(5)	0.00209	0.00482(4)	0.00369(5)	0.00338(5)	0.00184
40	0.00452(5)	0.00235(6)	0.00226	0.00498(5)	0.00401(6)	0.00316(5)	0.00200
20	0.00501(5)	0.00226(5)	0.00250	0.00553(5)	0.00452(6)	0.00308(5)	0.00226

Table A.10.: Anisotropic displacement parameters of (Mn1/Fe1) and (Mn2/Fe2) in $Mn_3Fe_2Si_3$ from the refinements of x-ray single crystal diffraction data in $P63/mcm$.

T [K]	(Si)			
	U_{11}	U_{22}	U_{33}	U_{12}
300	0.00630(9)	0.00572(12)	0.00852(12	0.00286
250	0.00594(8)	0.0056(1)	0.0076(1)	0.00284
200	0.00518(7)	0.0048(1)	0.00637(9)	0.00243
150	0.00477(7)	0.00451(9)	0.00557(9)	0.00225
125	0.00450(8)	0.0041(1)	0.00491(9)	0.00209
100	0.00431(8)	0.0040(1)	0.00439(9)	0.00200
80	0.00440(8)	0.0041(1)	0.0043(1)	0.00206
60	0.00464(9)	0.0044(1)	0.0039(1)	0.00220
40	0.0048(1)	0.0043(1)	0.0038(1)	0.00216
20	0.0053(1)	0.0052(1)	0.0037(1)	0.00260

Table A.11.: Anisotropic displacement parameters of (Si) in $Mn_3Fe_2Si_3$ from the refinements of x-ray single crystal diffraction data in $P63/mcm$.

T(K)	M1-M1$^{[i]}$	M1-M2$^{[ii]}$/M2$^{[iii]}$	M2$^{[ii]}$-M2$^{[iii]}$	M2$^{[ii]}$-M2$^{[iv]}$	M2$^{[ii]}$-Si	M2$^{[ii]}$-Si$^{[v]}$	M2$^{[ii]}$-Si$^{[vi]}$	M1-Si$^{[vii]}$
300	2.3778(1)	2.94629(15)	2.86352(17)	2.7636(3)	2.3958(4)	2.5029(4)	2.6454(2)	2.4039(4)
250	2.37585(1)	2.94475(17)	2.86099(16)	2.7608(3)	2.3941(4)	2.5022(5)	2.6435(2)	2.4024(4)
200	2.3737(1)	2.94301(19)	2.85803(15)	2.7571(2)	2.3921(3)	2.5012(4)	2.64157(19)	2.40046(13)
150	2.37125(1)	2.94135(18)	2.85504(15)	2.7541(2)	2.3904(3)	2.5005(4)	2.63926(19)	2.39874(13)
125	2.37045(1)	2.9406(19)	2.85405(15)	2.7531(3)	2.3898(3)	2.4998(4)	2.6385(2)	2.398(13)
100	2.36945(1)	2.93964(17)	2.85312(16)	2.7528(3)	2.3893(3)	2.4989(4)	2.6374(2)	2.3973(13)
80	2.36895(1)	2.93957(17)	2.8525(16)	2.7522(3)	2.3889(4)	2.4993(5)	2.637(2)	2.39713(14)
60	2.36895(1)	2.93931(17)	2.85246(16)	2.7521(3)	2.3885(4)	2.4992(5)	2.6368(2)	2.39702(14)
40	2.36845(1)	2.93902(19)	2.85194(15)	2.7517(3)	2.3886(5)	2.4986(6)	2.6365(2)	2.39663(19)
20	2.36855(1)	2.93895(18)	2.85202(19)	2.7517(4)	2.3883(5)	2.4988(5)	2.6364(2)	2.39669(19)

Table A.12.: Interatomic distances of $Mn_3Fe_2Si_3$ in space group $P6_3/mcm$ obtained from synchrotron X-ray single crystal diffraction at different temperatures (The assignment of the interatomic distances is illustrated in figure 7.2). Symmetry code: $[i]x, y, -z-1/2$, $[ii]-x+1, -y, -z$,$[iii]-y+1, x-y, z$, $[iv]-y+1, x-y, z$, $[v]y+1, -x+y, -z$, $[vi]-x+1, -y, -z$, $[vii]y, -x+y+1, -z$, $[viii]-y, x-y, z$.

T (K)	wR(obs/all)	R(obs/all)
105	3.13/3.14	2.26/2.27
90	3.54/ 3.55	2.51/ 2.52
50	3.76/3.77	2.70/2.71
20	3.48/3.49	2.54/2.55

Table A.13.: R(obs/all) and wR(obs/all) factors for nuclear reflections of $Mn_3Fe_2Si_3$ based on the neutron powder data measured on POWGEN at different temperatures for a center wavelength of 0.8 Å.

R(obs/all)								
T (K)	P[C]cmm	P[C]nam	P[C]nmn	P[C]can	P[C]nan	P[C]cmn	P[C]cam	P[C]nmm
105	13.51/ 30.18	7.41/ 24.87	11.17/ 23.44	13.37/ 29.89	7.39/ 16.35	10.61/ 19.91	10.92/ 27.64	8.82/ 18.32
90	12.61/ 30.90	11.20/ 25.38	12.28/ 24.24	11.52/ 22.74	5.56/ 13.71	9.47/ 16.47	7.87/ 19.23	9.25/ 17.72
50	14.02/ 24.18	9.56/ 18.71	12.91/ 21.91	11.55/ 18.79	6.22/ 11.27	8.47/ 14.62	12.03/ 20.69	10.42/ 15.99
20	15.03/ 22.19	12.45/ 20.46	15.34/ 21.06	13.82/ 20.64	9.64/ 13.51	11.03/ 16.18	13.13/ 20.45	11.72/ 16.84

Table A.14.: R(obs/all) factors for magnetic Bragg reflections of $Mn_3Fe_2Si_3$ based on the neutron powder data measured on POWGEN at different temperatures for a center wavelength of 0.8 Å.

wR(obs/all)								
T (K)	P[C]cmm	P[C]nam	P[C]nmn	P[C]can	P[C]nan	P[C]cmn	P[C]cam	P[C]nmm
105	4.51/ 5.07	3.97/ 4.49	3.75/ 4.23	4.05/ 4.58	4.80/ 5.06	4.11/ 4.38	4.21/ 4.78	3.79/ 4.16
90	4.55/ 5.00	4.47/ 4.84	4.05/ 4.44	4.41/ 4.71	4.74/ 4.94	4.01/ 4.23	4.10/ 4.42	4.49/ 4.74
50	4.33/ 4.61	4.16/ 4.36	4.17/ 4.40	4.42/ 4.61	4.14/ 4.29	4.94/ 5.09	4.74/ 4.93	4.52/ 4.71
20	4.37/ 4.58	4.17/ 4.34	4.34/ 4.49	4.44/ 4.61	4.10/ 4.23	4.14/ 4.26	4.40/ 4.59	4.17/ 4.41

Table A.15.: wR(obs/all) factors for magnetic Bragg reflections of $Mn_3Fe_2Si_3$ based on the neutron powder data measured on POWGEN at different temperatures for a center wavelength of 0.8 Å.

N.I.S.G	$Ama2$							
M.S.G	P[C]c2m	P[C]n2n	P[C]c2_1n	P[C]n2_1m	P[C]c2m	P[C]n2n	P[C]c2_1n	P[C]n2_1m
R(obs/all)	18.77/ 21.10	6.39/ 8.03	31.01/ 37.91	21.89/ 34.46	18.25/ 20.71	8.27/ 9.40	30.79/ 36.69	21.31/ 36.05
wR(obs/all)	20.77/ 20.88	9.04/ 9.18	42.12/ 42.35	22.52/ 24.09	20.14/ 20.25	10.96/ 11.00	38.41/ 38.67	22.32/ 23.23
N.P	6	9	11	8	6	9	11	8
N.I.S.G	$Amm2$							
M.S.G	P[C]2mm		P[C]2an		P[C]2_1am		P[C]2_1mn	
R(obs/all)	24.95/ 28.11		6.02/ 7.99		29.32/ 38.13		24.55/ 42.30	
wR(obs/all)	24.60/ 24.70		6.51/ 6.59		24.67/ 25.37		17.56/ 19.75	
N.P	6		10		8		10	
N.I.S.G	$Cmc2$							
M.S.G	P[C]cm2_1		P[C]na2_1		P[C]nm2_1		P[C]ca2_1	
R(obs/all)	20.31/26.16		13.71/15.96		26.04/40.36		23.08/32.57	
wR(obs/all)	20.46/20.88		13.87/13.98		24.61/26.81		24.20/24.85	
N.P	8		9		8		9	
N.I.S.G	$C222_1$							
M.S.G	P[C]222_1		P[C]$2_12_12_1$		P[C]22_12_1		P[C]2_122_1	
R(obs/all)	2.64/4.59		21.48/31.12		23.73/25.77		21.68/29.76	
wR(obs/all)	2.76/3.03		20.68/21.65		23.18/23.20		15.33/16.20	
N.P	7		10		9		8	
N.I.S.G	$C2/c$							
M.S.G	P[C]-1		P[C]-1		P[C]-1		P[C]-1	
R(obs/all)	48.14/50.77		45.62/49.52		13.67/17.11		12.62/15.72	
wR(obs/all)	57.91/57.96		54.11/54.18		13.97/14.15		12.60/ 12.75	
N.P	16		16		16		16	
N.I.S.G	$C2/m$							
M.S.G	P[C]2/m		P[C]2_1/a		P[C]2/a		P[C]2_1/m	
R(obs/all)	20.72/35.52		21.47/29.51		13.45/18.10		26.69/33.01	
wR(obs/all)	18.83/20.14		23.76/24.41		14.53/14.86		17.77/18.09	
N.P	7		10		8		9	
N.I.S.G	$C2_1/m$							
M.S.G	P[C]2_1/m		P[C]2_1/n		P[C]2_1/n		P[C]2_1/m	
R(obs/all)	18.62/25.38		7.71/12.68		21.03/24.82		66.81/65.19	
wR(obs/all)	19.15/19.73		6.69/7.09		22.73/23.24		59.15/59.12	
N.P	7		10		10		7	

Table A.16.: R(obs/all) and wR(obs/all) factors for magnetic Bragg reflections of $Mn_3Fe_2Si_3$ based on the neutron powder data measured on POWGEN at different 20 K for a center wavelength of 2.665 Å. **N.I.S.G**: non-isomorphic subgroups of *Ccmm*, **M.S.G**: magnetic space group derived from N.I.S.G, **N.P**: number of paremeters.

<table>
<tr><td>N.I.S.G</td><td colspan="8">$Ama2$</td></tr>
<tr><td>M.S.G</td><td>P[C]c2m</td><td>P[C]n2n</td><td>P[C]c2$_1$n</td><td>P[C]n2$_1$m</td><td>P[C]c2m</td><td>P[C]n2n</td><td>P[C]c2$_1$n</td><td>P[C]n2$_1$m</td></tr>
<tr><td>R(obs/all)</td><td>29.92/ 31.94</td><td>10.80/ 17.66</td><td>30.56/ 32.61</td><td>24.06/ 39.07</td><td>27.18/ 29.45</td><td>11.84/ 13.48</td><td>28.10/ 33.05</td><td>24.17/ 39.11</td></tr>
<tr><td>wR(obs/all)</td><td>27.85/ 27.91</td><td>11.12/ 11.45</td><td>29.95/ 30.06</td><td>24.08/ 25.74</td><td>26.54/ 26.61</td><td>10.45/ 10.51</td><td>28.00/ 28.39</td><td>24.15/ 25.81</td></tr>
<tr><td>N.P</td><td>6</td><td>9</td><td>11</td><td>8</td><td>6</td><td>9</td><td>11</td><td>8</td></tr>
<tr><td>N.I.S.G</td><td colspan="8">$Amm2$</td></tr>
<tr><td>M.S.G</td><td colspan="2">P[C]2mm</td><td colspan="2">P[C]2an</td><td colspan="2">P[C]2$_1$am</td><td colspan="2">P[C]2$_1$mn</td></tr>
<tr><td>R(obs/all)</td><td colspan="2">35.32/38.75</td><td colspan="2">66.66/67.37</td><td colspan="2">20.97/32.60</td><td colspan="2">26.76/43.21</td></tr>
<tr><td>wR(obs/all)</td><td colspan="2">32.11/32.20</td><td colspan="2">49.14/49.61</td><td colspan="2">20.67/21.79</td><td colspan="2">22.64/24.35</td></tr>
<tr><td>N.P</td><td colspan="2">6</td><td colspan="2">10</td><td colspan="2">8</td><td colspan="2">10</td></tr>
<tr><td>N.I.S.G</td><td colspan="8">$Cmc2$</td></tr>
<tr><td>M.S.G</td><td colspan="2">P[C]cm2$_1$</td><td colspan="2">P[C]na2$_1$</td><td colspan="2">P[C]nm2$_1$</td><td colspan="2">P[C]ca2$_1$</td></tr>
<tr><td>R(obs/all)</td><td colspan="2">28.96/37.65</td><td colspan="2">7.27/13.37</td><td colspan="2">29.51/51.42</td><td colspan="2">32.02/36.60</td></tr>
<tr><td>wR(obs/all)</td><td colspan="2">26.98/27.48</td><td colspan="2">6.29/7.13</td><td colspan="2">23.76/25.75</td><td colspan="2">29.75/29.87</td></tr>
<tr><td>N.P</td><td colspan="2">8</td><td colspan="2">9</td><td colspan="2">8</td><td colspan="2">9</td></tr>
<tr><td>N.I.S.G</td><td colspan="8">$C222_1$</td></tr>
<tr><td>M.S.G</td><td colspan="2">P[C]222$_1$</td><td colspan="2">P[C]2$_1$2$_1$2$_1$</td><td colspan="2">P[C]22$_1$2$_1$</td><td colspan="2">P[C]2$_1$22$_1$</td></tr>
<tr><td>R(obs/all)</td><td colspan="2">4.34/5.79</td><td colspan="2">21.22/34.68</td><td colspan="2">33.62/36.40</td><td colspan="2">21.56/32.33</td></tr>
<tr><td>wR(obs/all)</td><td colspan="2">5.84/5.94</td><td colspan="2">19.32/21.20</td><td colspan="2">34.58/34.63</td><td colspan="2">21.07/22.24</td></tr>
<tr><td>N.P</td><td colspan="2">7</td><td colspan="2">10</td><td colspan="2">9</td><td colspan="2">8</td></tr>
<tr><td>N.I.S.G</td><td colspan="8">$C2/c$</td></tr>
<tr><td>M.S.G</td><td colspan="2">P[C]-1</td><td colspan="2">P[C]-1</td><td colspan="2">P[C]-1</td><td colspan="2">P[C]-1</td></tr>
<tr><td>R(obs/all)</td><td colspan="2">29.52/46.38</td><td colspan="2">32.70/50.14</td><td colspan="2">14.47/19.73</td><td colspan="2">13.58/18.84</td></tr>
<tr><td>wR(obs/all)</td><td colspan="2">27.86/28.84</td><td colspan="2">30.99/31.88</td><td colspan="2">15.44/15.58</td><td colspan="2">11.96/12.15</td></tr>
<tr><td>N.P</td><td colspan="2">16</td><td colspan="2">16</td><td colspan="2">16</td><td colspan="2">16</td></tr>
<tr><td>N.I.S.G</td><td colspan="8">$C2/m$</td></tr>
<tr><td>M.S.G</td><td colspan="2">P[C]2/m</td><td colspan="2">P[C]2$_1$/a</td><td colspan="2">P[C]2/a</td><td colspan="2">P[C]2$_1$/m</td></tr>
<tr><td>R(obs/all)</td><td colspan="2">29.83/48.27</td><td colspan="2">22.67/34.01</td><td colspan="2">12.59/17.33</td><td colspan="2">23.72/39.47</td></tr>
<tr><td>wR(obs/all)</td><td colspan="2">23.83/25.12</td><td colspan="2">22.81/23.76</td><td colspan="2">12.29/12.41</td><td colspan="2">18.38/19.83</td></tr>
<tr><td>N.P</td><td colspan="2">7</td><td colspan="2">10</td><td colspan="2">8</td><td colspan="2">9</td></tr>
<tr><td>N.I.S.G</td><td colspan="8">$C2_1/m$</td></tr>
<tr><td>M.S.G</td><td colspan="2">P[C]2$_1$/m</td><td colspan="2">P[C]2$_1$/n</td><td colspan="2">P[C]2$_1$/n</td><td colspan="2">P[C]2$_1$/m</td></tr>
<tr><td>R(obs/all)</td><td colspan="2">25.81/34.13</td><td colspan="2">10.00/15.02</td><td colspan="2">23.21/33.23</td><td colspan="2">26.53/30.08</td></tr>
<tr><td>wR(obs/all)</td><td colspan="2">24.17/24.87</td><td colspan="2">10.88/11.04</td><td colspan="2">23.58/24.33</td><td colspan="2">21.48/21.63</td></tr>
<tr><td>N.P</td><td colspan="2">7</td><td colspan="2">10</td><td colspan="2">10</td><td colspan="2">7</td></tr>
</table>

Table A.17.: R(obs/all) and wR(obs/all) factors for magnetic Bragg reflections of $Mn_3Fe_2Si_3$ based on the neutron powder data measured on POWGEN at different 50 K for a center wavelength of 2.665 Å. **N.I.S.G**: non-isomorphic subgroups of *Ccmm*, **M.S.G**: magnetic space group derived from N.I.S.G, **N.P**: number of paremeters.

List of Figures

List of Tables

Eidesstattliche Erklärung

Declaration of Authorship

I, *Mohammed Ait haddouch*

declare that this thesis and the work presented in it are my own and has been generated by me as the result of my own original research.

Hiermit erkläre ich an Eides statt / I do solemnly swear that:

1. This work was done wholly or mainly while in candidature for the doctoral degree at this faculty and university;

2. Where any part of this thesis has previously been submitted for a degree or any other qualification at this university or any other institution, this has been clearly stated;

3. Where I have consulted the published work of others or myself, this is always clearly attributed;

4. Where I have quoted from the work of others or myself, the source is always given. This thesis is entirely my own work, with the exception of such quotations;

5. I have acknowledged all major sources of assistance;

6. Where the thesis is based on work done by myself jointly with others, I have made clear exactly what was done by others and what I have contributed myself;

7. None of this work has been published before submission.

29.11.2021